UNIVERSITÀ DEGLI STUDI DI MILANO
FACOLTÀ DI SCIENZE MATEMATICHE, FISICHE E NATURALI
DOTTORATO DI RICERCA IN
FISICA, ASTROFISICA E FISICA APPLICATA

STUDY OF DTL STABILIZATION WITH POST COUPLERS FOR THE SPES DRIVER LINAC

Settore Scientifico disciplinare FIS/04

Coordinatore: Prof. Marco Bersanelli
Tutore: Prof. Angela Bracco

Tesi di Dottorato di:
Francesco Grespan
Ciclo XXII

Anno Accademico 2008-2009

To Agnese.

Table of Contents

Introduction

Particle accelerators are powerful instruments for physics investigation. They allow researching unknown matter components, as new nuclei or new fundamental particle, or reproducing in a laboratory the very early instants of the universe. On the other hand, accelerators are used for cancer therapy and for radio-pharmaceutical production. Furthermore accelerators allow generating intense photon and neutron beams for a large number of applications (electronics, spectroscopy, material science).

Main parameters for accelerator characterization are final energy and beam intensity. Over last years, together with construction and start-up of the high energy collider LHC for elementary particle study, demand and supply of more intense beams has increased, for experiments on synthesis of exotic nuclei, for study of new radioactive waste disposal systems and for medical applications. Construction of high intensity beam accelerator entails to get through a large number of scientific and technological challenges, related to the transport of high power beams, to the beam loss control and finally to the accelerator structure activation. In a word, what must be guaranteed is the stability of the accelerator.

The concept of stability in accelerator physics includes a vast number of topics and one of the most important is the *stabilization of the accelerating field*. Stabilizing the accelerating field means reducing the field sensitivity to geometric factors of perturbation, in order to keep the field within the limits which guarantee a good beam quality. Perturbation factors can have different origins, from the mechanical machining to the heating during high power operation, but they always cause a geometric error which affects the nominal field configuration. Furthermore, a larger L/λ ratio (structure length over wave length) accentuates the effect of geometrical errors on the accelerating field.

In *drift tube linear accelerators* the accelerating field stabilization is obtained by equipping the cavity with special devices called *post couplers*, which consist of resonant bars installed in the horizontal cavity plane. The study of this stabilization device is the core of my thesis.

This thesis work arose from the research and development program related to the proposal of a normal conducting linac as a driver accelerator for the SPES RIB facility at LNL. Based on some parameter similarities of the two projects, the collaboration between SPES and Linac4 project on the design and construction of drift tube linacs (DTL) gave to me the opportunity to deepen the knowledge on this accelerating structure by using DTL prototypes already present at CERN.

Main objectives of my thesis are:

- to analyze 2D and 3D simulations of DTL cavity, in order to deepen the understanding of the post coupler working principle;
- to develop the equivalent circuit for DTL cavity, describing the complete cavity topology, including stems and post couplers;
- to define a procedure for optimum post coupler length calculation, based on the equivalent circuit analysis;
- to validate equivalent circuit and tuning procedure with measurements.

In Chapter 1 the physics scenario concerning the SPES project is presented, together with the facility layout. The proposed driver linac, consisting in the RFQ and the DTL, is then introduced.

Chapter 2 is an introduction to the Linac4 project, presented in the frame of the CERN new injectors. The DTL of Linac4, more involved in this work, is presented in detail.

Chapter 3 consists of a brief overview of the concept of Alvarez Drift Tube Linac, Resonant Coupling and Post Coupler Stabilization in a DTL.

The core of the research work starts at Chapter 4, where 2D and 3D simulations performed on post couplers are shown, together with a geometrical estimation of equivalent circuit parameters in the quasi-static approximation.

In Chapter 5 the equivalent circuit development is presented.

Chapter 6 illustrates the tuning procedure defined on the equivalent circuit assumptions and measurements undertaken to validate it.

Chapter 7 summarizes the conclusions of this work.

In three Appendices we present arguments of interest or related to the thesis body. Appendix A is an introduction to the figures of merit of a resonant cavity. Appendix B describes the high power test of the DTL prototype. Appendix C presents the equivalent circuit for the Stems.

Chapter 1. The SPES Project

SPES (Selective Production of Exotic Species) is the project for the construction of a facility for radioactive ion beams (RIBs) at INFN-LNL. It will be an ISOL-type facility, based on a 40 MeV proton driver and on a multi-slice direct target. The facility will provide neutron-rich RIBs with energies up to 10 MeV/u and with masses in the range 80-160 u.

In this chapter we introduce the physics scenario where the SPES project will be located, we present the general layout of the facility and finally we focus on the driver accelerator, describing the proposal of the linac.

1.1 Physics with Radioactive Ion Beams (RIBs)

The nuclear physics can be divided in two main parts:

- the study of nuclear structure, which includes all theories concerning shape, cohesion and static properties of the nucleus, like mass, energy levels, spin status;
- the study of nuclear reactions, which includes radioactive decays and all processes where two or more nuclei collide to produce different nuclei, such as fragmentation, fusion and nucleon transfers.

These two branches are strictly connected, in the sense that all information on nuclear structure comes from studies of nuclear reactions and, on the other hand, nuclear reactions themselves can be interpreted from an understanding of nuclear structure.

Since the discovery of the nucleus, in 1912, knowledge of nuclear physics has been gained by studying nuclei near the valley of beta stability in the chart of nuclides (Figure 1.1), from observing natural decays of unstable elements, nuclear reactions in the stars and reactions induced in accelerator beam facilities. Unlike the atomic model, there is not a unique theory describing all nuclear properties, but there are different models, complementary to each other, such as the liquid drop model, the shell model and the mean field models. In order to generalize nuclear models towards a unique nuclear description and to understand the element production in the Universe, larger regions of the chart of nuclides need to be explored: the regions of exotic nuclei.

Unstable and rare, the exotic nuclei do not live long enough to make a target, therefore, to study reactions involving them at first seems impossible. The revolution came from the possibility of producing beams of exotic nuclei. Instead of sending the probe to the nucleus to be studied, it is sufficient to send the nucleus to the probe.

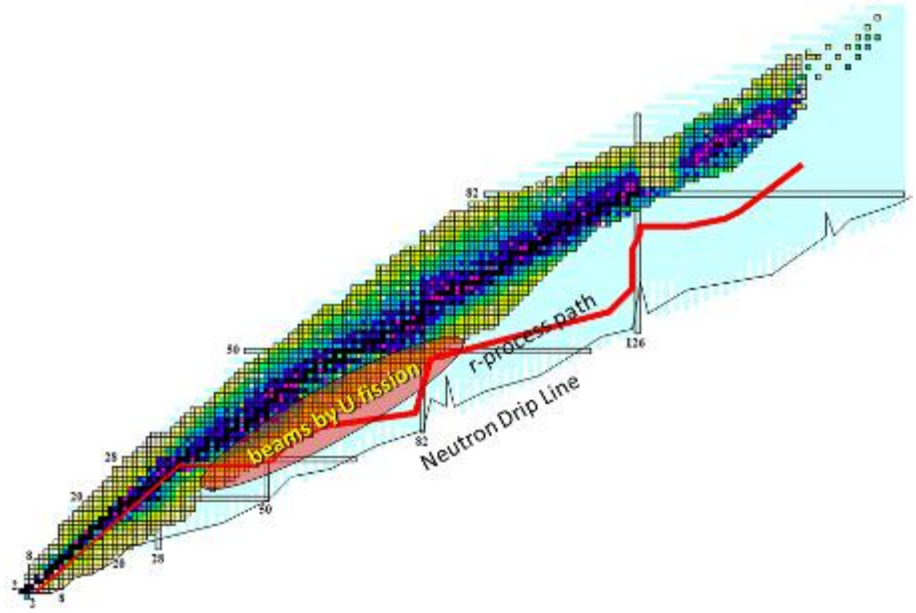

Figure 1.1: chart of nuclides.

The history of RIB facilities started more than 50 years ago in order to satisfy the need to study of nuclei far from the stability valley. Otto Kofoed-Hansen and Karl Ove Nielsen at the Niels Bohr Institute in Copenhagen were the first to perform such an experiment in 1951 [1]. They were investigating beta-decay and neutrino emission from neutron-rich krypton isotopes, produced in uranium fission. They used deuterons from their cyclotron on an internal target to produce neutrons. These then impinged upon a uranium oxide target (mixed with baking powder) from which gas flowed. The gas was then ionized, extracted from a high-voltage platform and passed through a mass separator, which selected the krypton ions of interest.

Today a large number of facilities for RIB are operating around the world: ISOLDE at CERN, SPIRAL in Ganil, EXCYT in Catania in Europe, and HRIBF at ORNL, NSCL at Michigan State University, ISAC at TRIUMF in North America. Furthermore a number of projects are proposed or already under realization, as SPES at LNL, SPIRAL2 in Ganil, the upgrade of REX-ISOLDE at CERN and FAIR at GSI [2].

The SPES project is concentrating on the production of neutron rich radioactive beams from uranium fission with mass in the range 80-160 u (Figure 1.1) [3]. The number of possible experiments with such beams is incredibly large, but we would like to highlight two fields of interest to be explored with exotic beams of this mass region: the study of the shell structure for nuclei of intermediate mass and the r-process in astrophysics.

The shell model of nuclear structure is based on a picture where nucleons experience a mean field generated by all the others, and they are arranged in shells, each one able to contain up to a certain number of nucleons determined by quantum numbers. If a shell is fully occupied, a sizeable energy gap appears between the last occupied shell and the first unoccupied shell, providing an extra stability of the nucleus. Shell completions defines magic numbers for protons and neutrons: 2, 8, 20, 28, 50, 82, 126. Nuclei which have both neutron number N and proton number Z equal to one of the magic numbers are called double magic. Magic numbers are well established for nuclei along the stability line.

However, for neutron-rich nuclei far from stability the vanishing of the classical shell gaps and the presence of new magic numbers might occur. In fact, magic numbers are generated by the spin-orbit interaction, which pushes up the energy gap if the relative orientation of the intrinsic spin is anti-parallel to the orbital angular momentum, or push it down if parallel. A large excess of neutrons with respect to protons ($N>>Z$) could affect the shell structure because of a reduction of the spin-orbit interaction due to the neutron spatial distribution, which forms a skin on the outside of the nucleus (Figure 1.2). New magic numbers could be similar to those produced by a harmonic oscillator when switching off the spin-orbit coupling (Figure 1.3). These predictions can be tested by measuring binding energies of single particle states in neutron rich nuclei with N=40, 50, 70, which are in the range of masses foreseen for SPES [4].

Exotic nuclei produced by the SPES facility are in the ideal range of masses to investigate a nucleo-synthesis process called r-process. This process involves n-capture $n + (Z, N) \rightarrow (Z, N+1) + \gamma$, the photodisintegration $\gamma + (Z, N+1) \rightarrow (Z, N) + n$ and the beta decay $(Z, N) \rightarrow (Z+1, N-1) + e^- + \nu$. In core-collapse supernovae, where neutron flux and temperature are extremely high, a rapid succession of neutron captures (r-process) occurs. Neutron captures are much faster than beta-minus decays, meaning that the r-process "runs up" the N axis in the chart of nuclides. After an element has captured enough neutrons to close a neutron shell, there is an equilibrium between n-captures and γ-decays and a slower beta decay occurs, taking the r-process path closer to the stability valley (vertical parts of the r-process path in Figure 1.1). SPES could allow experiments to follow the r-process path up to N=82 by producing exotic species with mass range $A \approx 80\text{-}130$ [6].

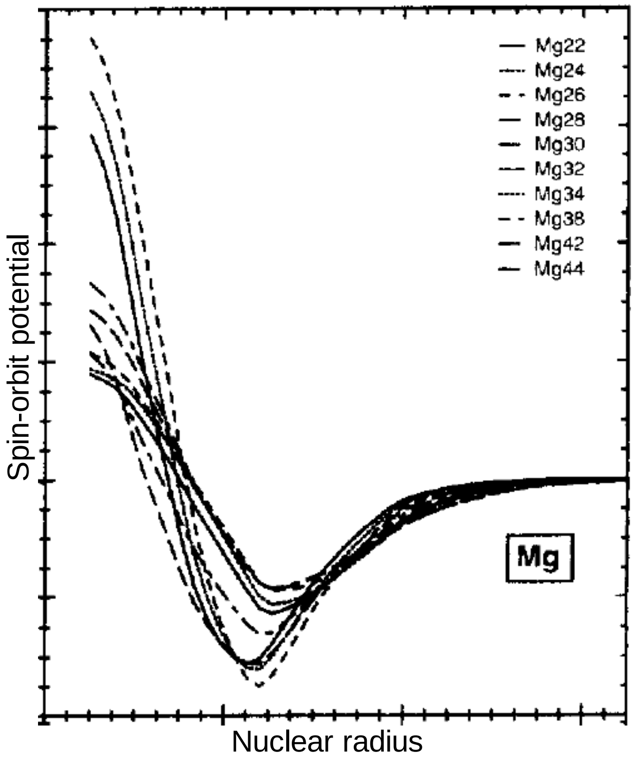

Figure 1.2: radial dependence of the spin-orbit potential for different Mg isotopes. Neutron rich isotopes experience a lower spin-orbit potential [5].

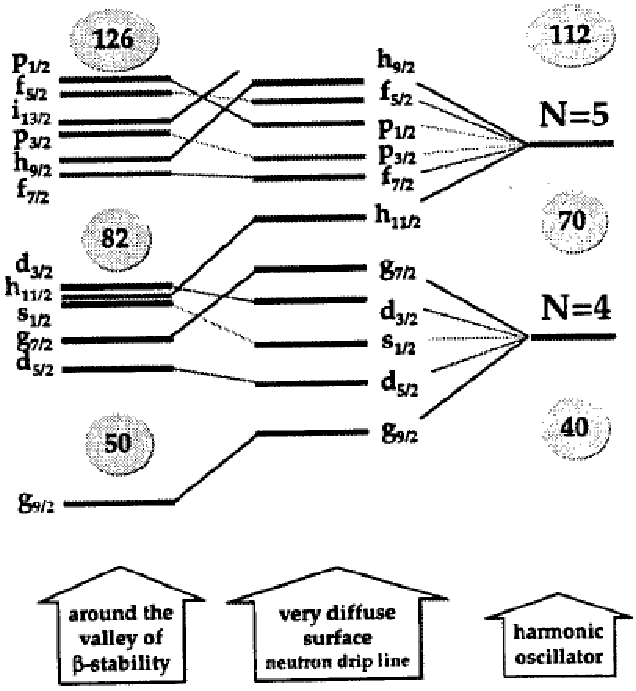

Figure 1.3: shell structures for nuclei close to the stability valley (left), for nuclei in the drip line (middle) and for harmonic oscillator (right), which reproduces nuclear potential in absence of spin-orbit coupling.

For many experiments related to the SPES project γ-ray detection will be crucial. Most parts of present γ-detectors consist of large volume germanium crystals surrounded by shields for Compton-ray suppression, which limit the detection efficiency and resolution power. SPES will be the platform to test a new generation of detectors based on electrical segmented Ge crystals. As shown in Figure 1.4, the γ-rays interact with different segments of the Ge array. Segment signals are then processed in order to identify all interaction points, "track" the path of a given γ-ray and finally obtain the full initial γ-ray energy by only summing tracked interactions. This process guarantees high energy resolution, efficiency and sensitivity. In particular for SPES a portion of the future AGATA detector, covering a solid angle of 1 π will be used [6, 7] (Figure 1.5).

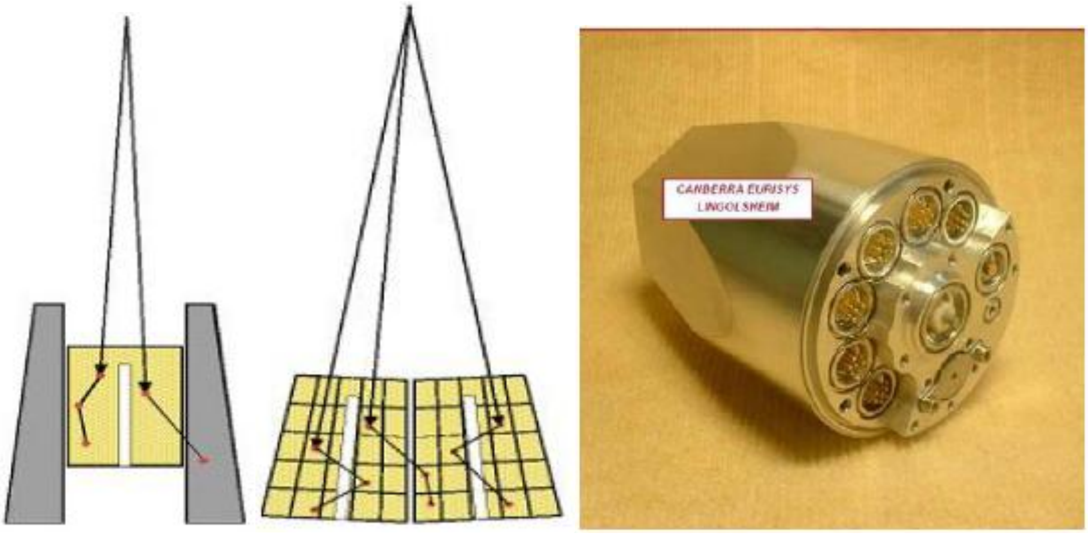

Figure 1.4: a scheme of a Ge crystal with shield for Compton-ray suppression (left) compared with a segmented Ge crystal (center). In the right picture of a segmented Ge array electrical connectors to single segments are shown.

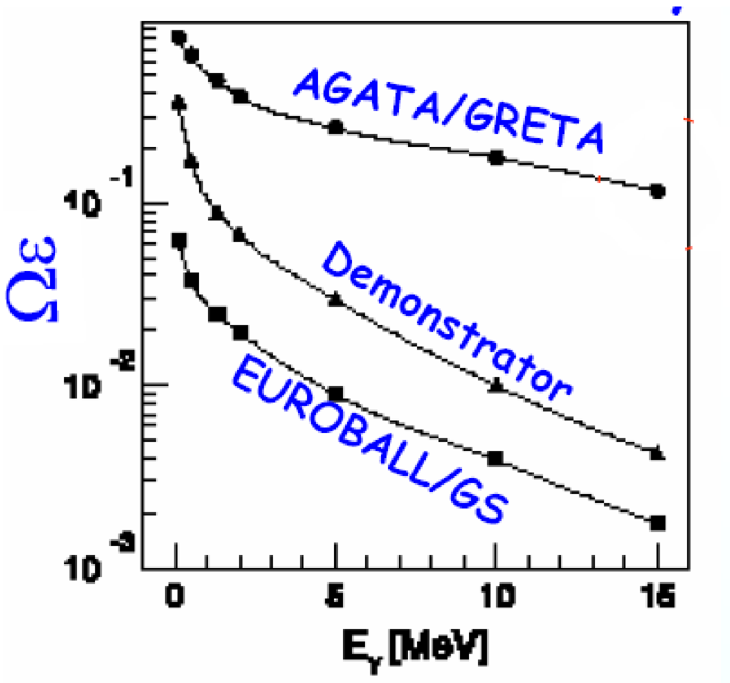

Figure 1.5: detection efficiency of present detectors like Euroball, compared with the AGATA demonstrator and with the complete AGATA array.

1.2 SPES project layout

A schematic layout of the SPES facility at LNL is shown in Figure 1.6 [1].

SPES is an ISOL facility, where an intense proton beam (primary beam) collides on a Uranium target for the production of exotic species, which are then ionized and re-accelerated in a post-accelerator. The construction of this facility at LNL is based on the availability of the super-conducting accelerator ALPI as the post-accelerator.

Main steps of the facility are:

- the TRIPS source, a high intensity microwave discharge ion source, built at INFN-LNS and now installed at LNL. TRIPS injects in the following RFQ 35 mA of protons with a rms emittance lower than 0.2π mm-mrad at an operating voltage of 80 kV.
- the RFQ, developed in the framework of the TRASCO project. The total, 7.13 m, length of the RFQ is segmented into 3 parts, which are resonantly coupled to each other, in order to improve the field stability. The final energy of the proton beam is 5 MeV with 4% of beam loss. The construction of the TRASCO RFQ is now complete (2009), and the first high power test is planned at the beginning of 2010.

- the Drift Tube Linac (DTL), which accelerates the 30 mA beam from 5 MeV to 43 MeV. For such an energy the DTL will be 15.2 m long, divided in 2 tanks, but the possibility of upgrading it up to 95 MeV has been considered.
- the multi-slice direct target, where 30 mA of protons at 43 MeV are directed for production of exotic species. The target consists of 7 disks of Uranium Carbide (UC_x). The impact of the proton beam on the UCx disks induces the production of fission fragments. Because of the high temperature of the target ($T > 2000°$ C), fragments diffuse to the surface and can be directed to the ion source, where they are ionized at +1 charge state.
- the high resolution spectrometer, able to distinguish nuclear species with a mass resolution of 1/20000. This spectrometer selects the element candidate for the radioactive ion beam. To optimize the reacceleration, a Charge Breeder will be developed to increase the charge state to +N, because for efficient acceleration in the ALPI linac a charge over mass of 1/10 is required.
- the post-accelerator, consisting of the bunching RFQ, the PIAVE Superconducting RFQ and the superconducting linac, ALPI. The selected RIB is accelerated up to 10 MeV/u with an overall transmission of 70% and finally sent to the experimental areas.

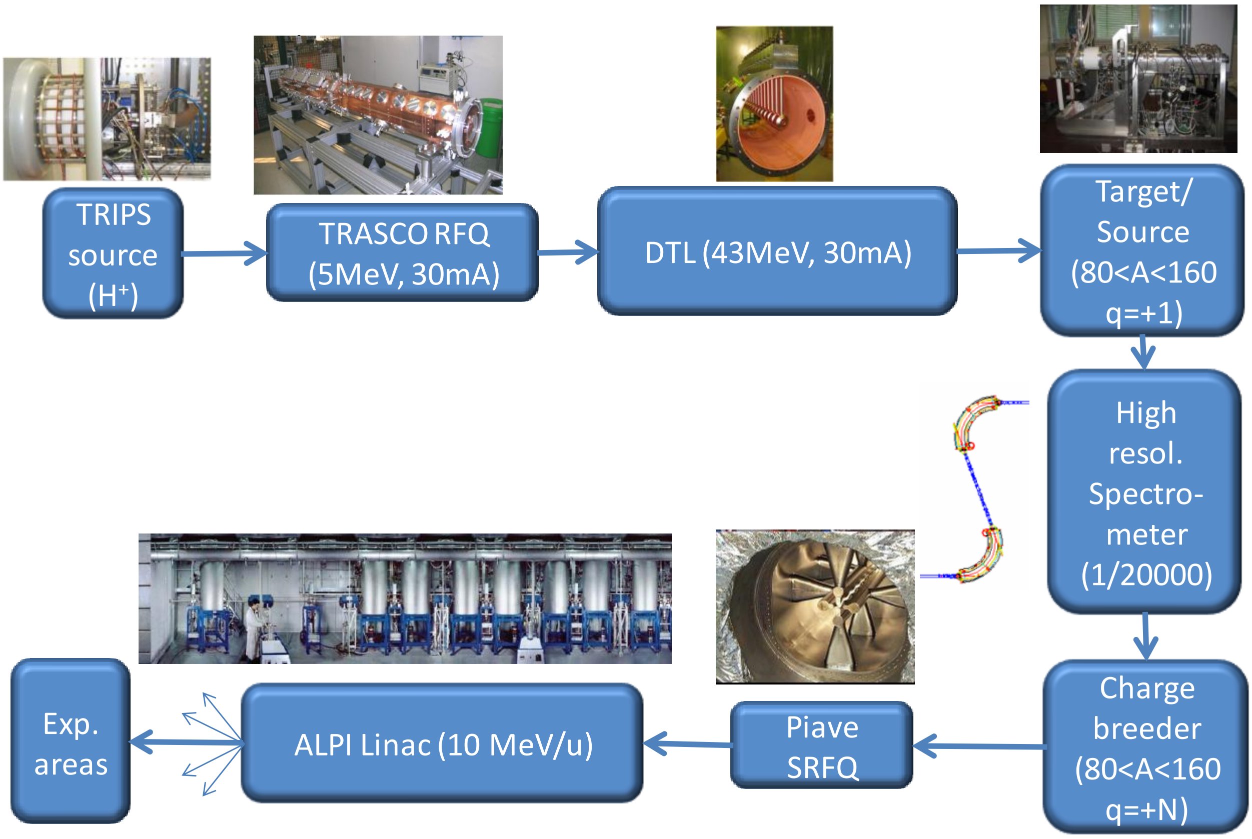

Figure 1.6: schematic layout of the SPES facility at LNL.

The repetition rate of the driver linac (RFQ and DTL) has been chosen in order to satisfy a specific requirement related to the thermal behavior of the production target. The target is heated up to 2200° C to enhance the release of fission products and it can withstand a average beam power deposition of about 10 kW. The linac beam power is indeed pulsed. The pulsing adds a time dependent transient to the target temperature distribution and to the stress distribution in the target disks. With a linac repetition rate >10 Hz this effect is completely negligible, as shown in Figure 1.7. At the nominal rep. rate of 50 Hz the transient temperature ripple is 100 times lower than the maximum temperature non-homogeneity in the target and would not influence the target performances and lifetime [8].

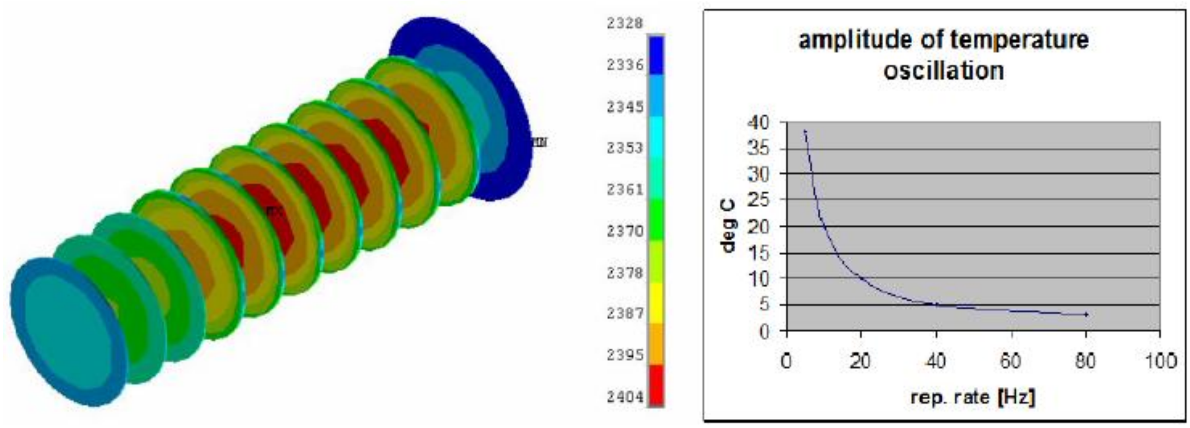

Figure 1.7: 3D simulation of the temperature distribution on the SPES production target, and temperature ripple amplitude as a function of the repetition rate frequency.

Figure1.8 shows the intensity available in the experimental target for different SPES exotic beams. It is determined by the relation

$$I = I_p \cdot \Delta x \cdot \sigma \cdot E_r \cdot E_i \cdot E_s \cdot E_t \cdot E_p$$

where σ is the cross section of the production reaction, I_p the primary beam intensity, Δx the thickness of the production target, E_r the efficiency of release of the target and transfer, E_i the efficiency of ion source, E_s the efficiency of the separator, E_t the delay transfer efficiency due to radioactive decay losses and finally E_p the efficiency of the post-accelerator [1].

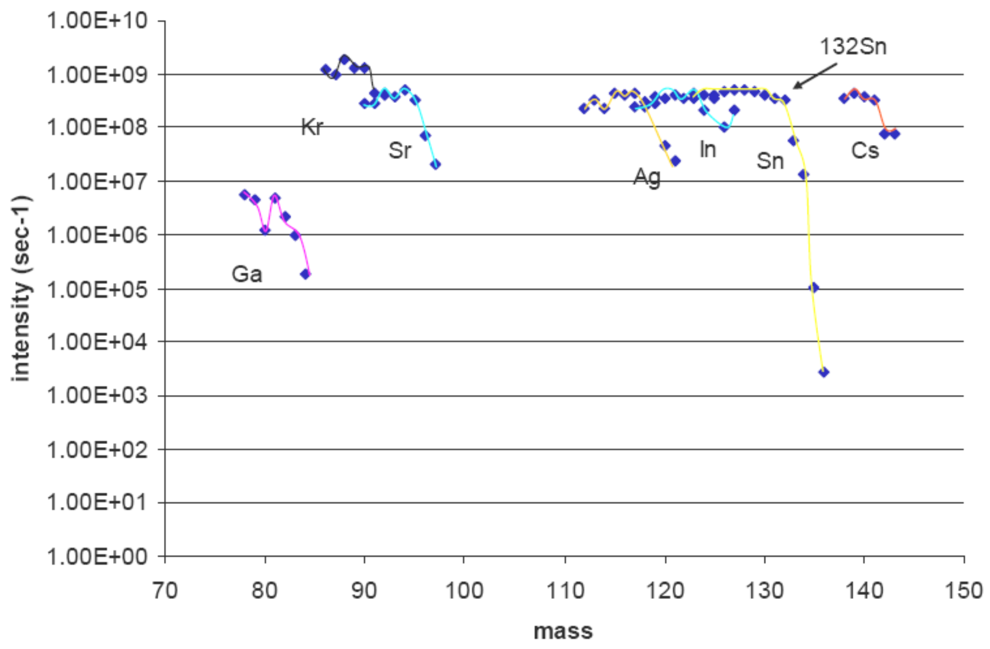

Figure 1.8: SPES RIB intensities on experimental targets, calculated by considering the primary beam intensity, the production target release and the acceleration efficiencies.

1.3 SPES driver linac RF structures

The layout of the LINAC is presented in Figure 1.9; the main elements are the off resonance ECR source (TRIPS), the Low Energy Beam Transport (LEBT), the radio frequency quadrupole (RFQ), the Medium Energy Beam Transport (MEBT) and the Drift Tube Linac (DTL). The main beam parameters of the linac are listed in Table 1.1 [1, 8].

The RFQ, initially designed for the TRASCO project, is able to accelerate the beam from 80 keV up to 5 MeV with a current of 30 mA, with 100% duty cycle. The CW operation option is foreseen in order to satisfy requirements of the Boron Neutron Capture Therapy application, which requires a powerful proton beam (150 kW) delivered to a beryllium target for the production of neutrons for an innovative cancer therapy study. The maximum duty cycle for SPES operation is 3%, the operating frequency is 352 MHz with the design choice of the use of a single 1.3 MW klystron already used at LEP. The RF power will be fed by means of eight high power loops. In order to keep beam losses below 4%, the longitudinal field stabilization for the operating mode will be achieved with two coupling cells, which reduce the effect of perturbing quadrupole modes, and with 24 dipole stabilizing rods in order to reduce the effect of perturbing dipole modes. Indeed, 104 slug tuners will keep the quadrupole mode longitudinal ripple below 1% of the nominal value ($\Delta V_q/V_q \leq 0.01$), as well as the residual dipole component below 2% of the longitudinal field uniformity of quadrupole mode (±1%).

Parameter	
Ion species	H+
Source output energy	80 keV
Linac output energy	43 MeV
Bunch frequency	352.2 MHz
Max.rep. rate	50 Hz
Max beam pulse length	600 μs
Max. beam duty cycle	3%
Max source current	60 mA
Linac pulse current	50 mA
Average current	1.5 mA
Max Beam power	64.5 kW
Linac output transverse emittance	0.22 π mm mrad

Table 1.1: SPES driver linac beam parameters

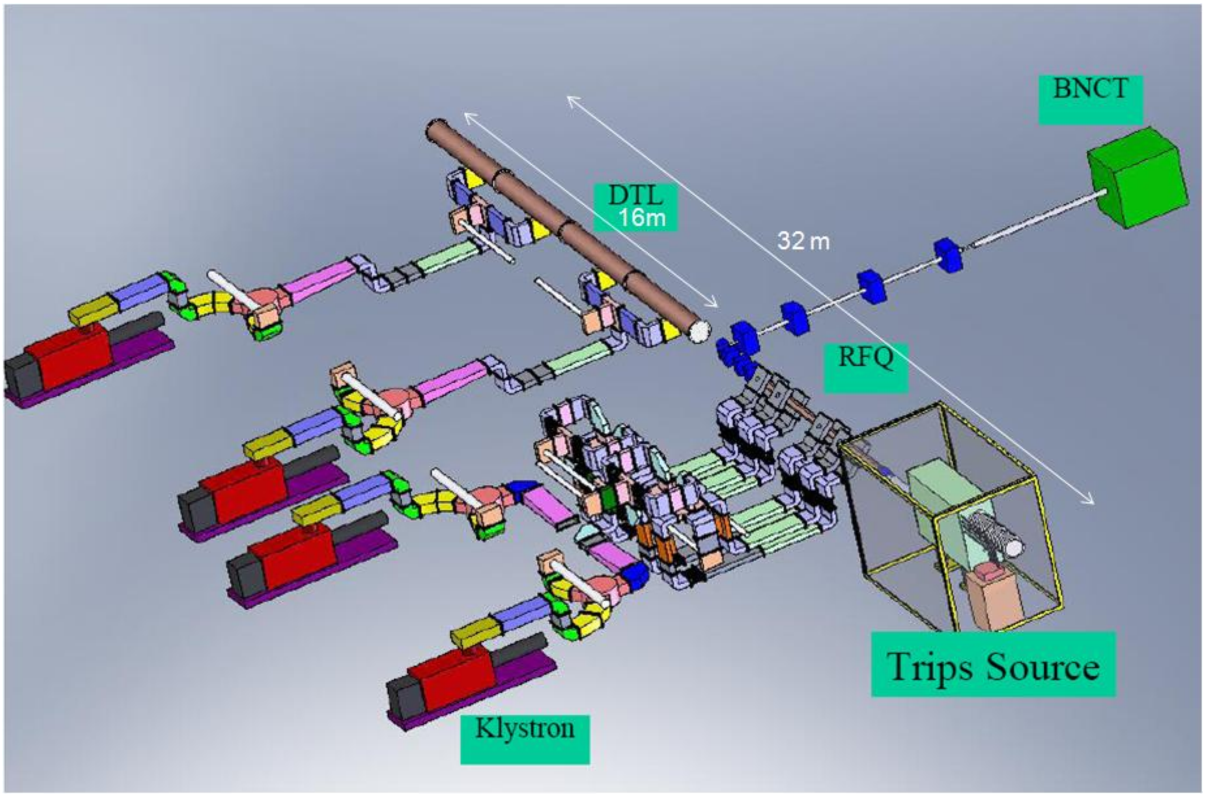

Figure 1.9: SPES driver linac layout.

The parameters of the SPES DTL are listed in Table 1.2.

Parameter	Tank 1	Tank 2
Frequency [MHz]	352.2	352.2
Average pulse current [mA]	50	50
Design RF duty cycle	10%	10%
Tank inner diameter [mm]	520	520
Drift tube diameter [mm]	90	90
Aperture radius [mm]	10	10
Length [m]	7.53	7.68
PMQ length [mm]	45	45
Focusing scheme	FFDD	FFDD
Max. surface field [kilp]	1.6	1.23
Synchronous phase [deg]	-35/-20	-20
Gradient E_0 [MV/m]	3.1	3.1
Final Energy [MeV]	23.82	43
RF peak power (incl. beam)[MW]	2.0	2.0
N. of klystrons	1 (2.5 MW)	1 (2.5 MW)
N. of gaps	55	35
N. of Post Couplers	27	17
Stem diameter [mm]	29	29
Post coupler diameter [mm]	20	20
Number of Tuners	10	10
Tuner diameter [mm]	90	90

Table 1.2: SPES DTL parameters.

The DTL is designed to provide an high quality proton beam to the production target of the SPES project. The structure, composed by 2 tanks of 7.53 m and 7.68 m for a total length of 15.2 m, accelerates proton pulses of 50 mA from 5 MeV to 43 MeV. The input energy of 5 MeV, higher with respect to other similar cases (Linac4: 3MeV, SNS: 2.5 MeV), allows avoiding troublesome constraints on focusing strength and peak electric field due to short length of gaps at low energy.

The average electric field is constant at 3.1 MV/m for the whole structure, while the synchronous phase is ramped from -35° up to -20° in the first tank to accommodate the input beam. The maximum surface electric field is kept below 1.6 kilpatrick to avoid RF breakdown risks.

The beam focusing is provided by permanent quadrupole magnets installed inside drift tubes with the constant focusing scheme FFDD. The use of permanent magnets, beside reducing the number of power supplies and the complexity of the control of the machine, allows the use of smaller drift tubes and the achievement of a higher shunt impedance. The shunt impedance curve shown in Figure 1.10 is determined by drift tube design choices. Geometrical parameters and dimensions of a drift tube linac half cell are shown in Figure 1.11. In our case, only face angle varies along the structure in order to keep each cell tuned at the operating frequency of 352.2 MHz. A larger face angle value allow to keep the accelerating gap length relatively small with respect to the cell length, and a small accelerating gap increases the shunt impedance. For short drift tubes face angle is limited by permanent magnet space.

The beam dynamics design was aimed at keeping the transverse and longitudinal phase advances continuous. Figure 1.12 shows the nominal simulation case performed with TraceWin for the output beam. Figure 1.13 shows beam envelopes along the DTL. Computations foresee no losses and no emittance growth.

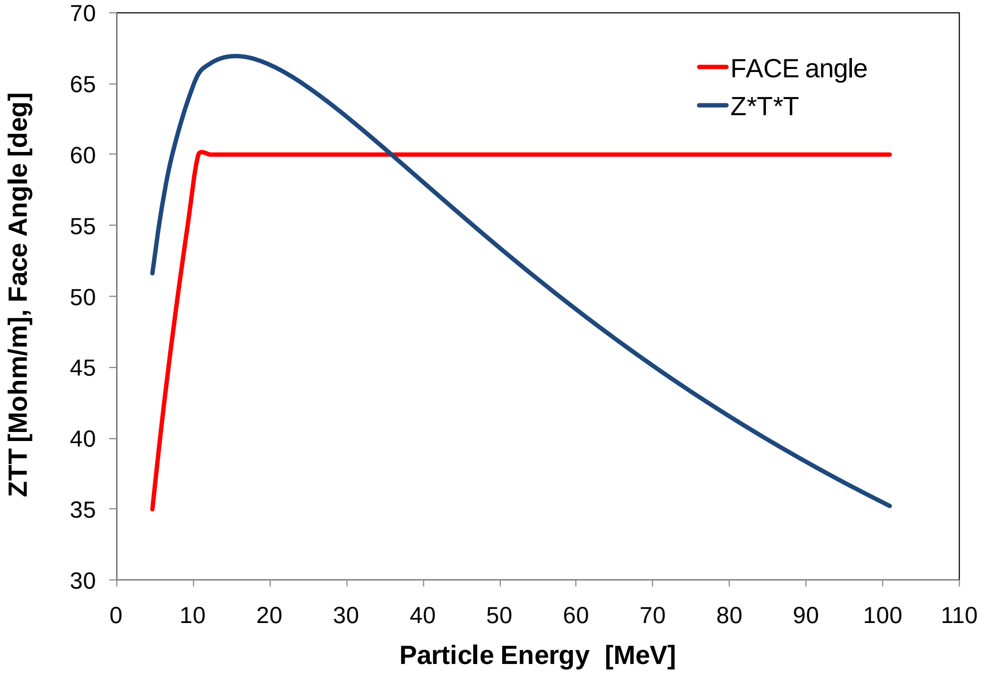

Figure 1.10: face angle and shunt impedance ZT^2 (Superfish value) as functions of particle energy for SPES DTL design up to 100 MeV.

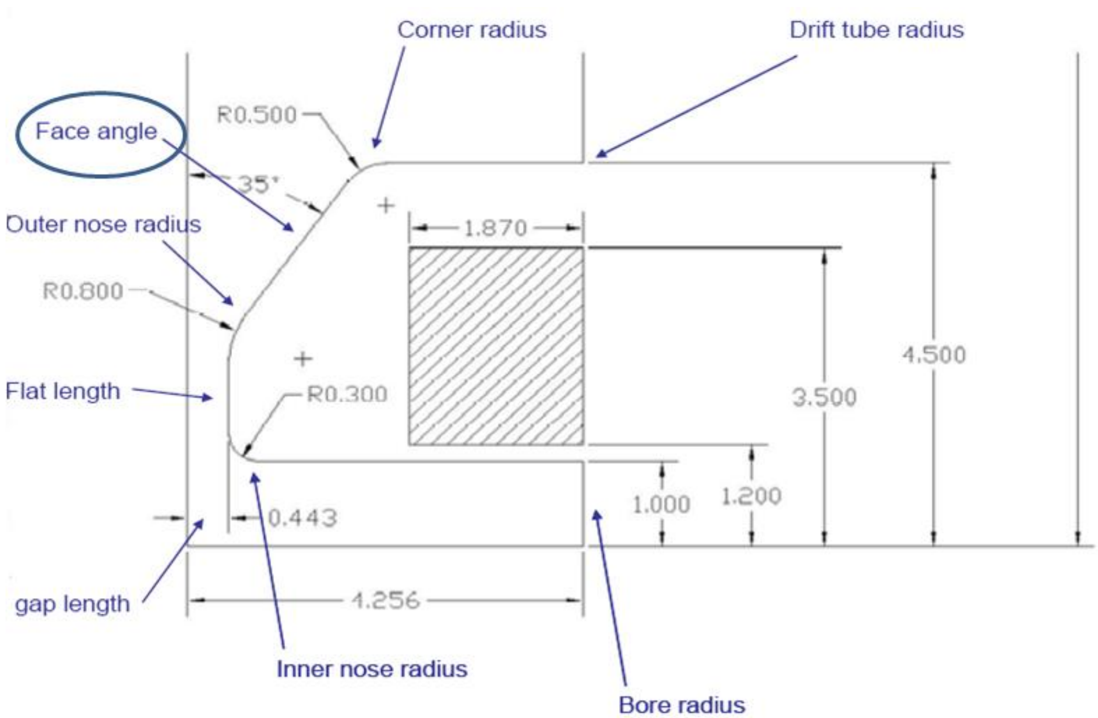

Figure 1.11: geometrical parameters and dimensions of a drift tube linac half cell. Shaded area marks the magnet position and dimension.

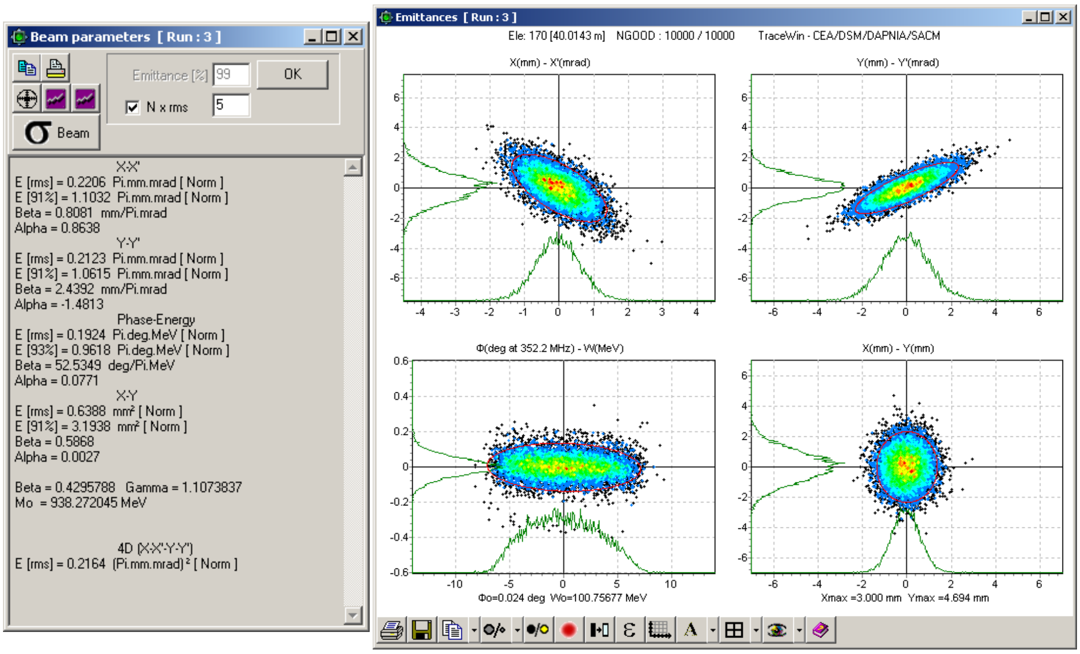

Figure 1.12:Output beam from the DTL.

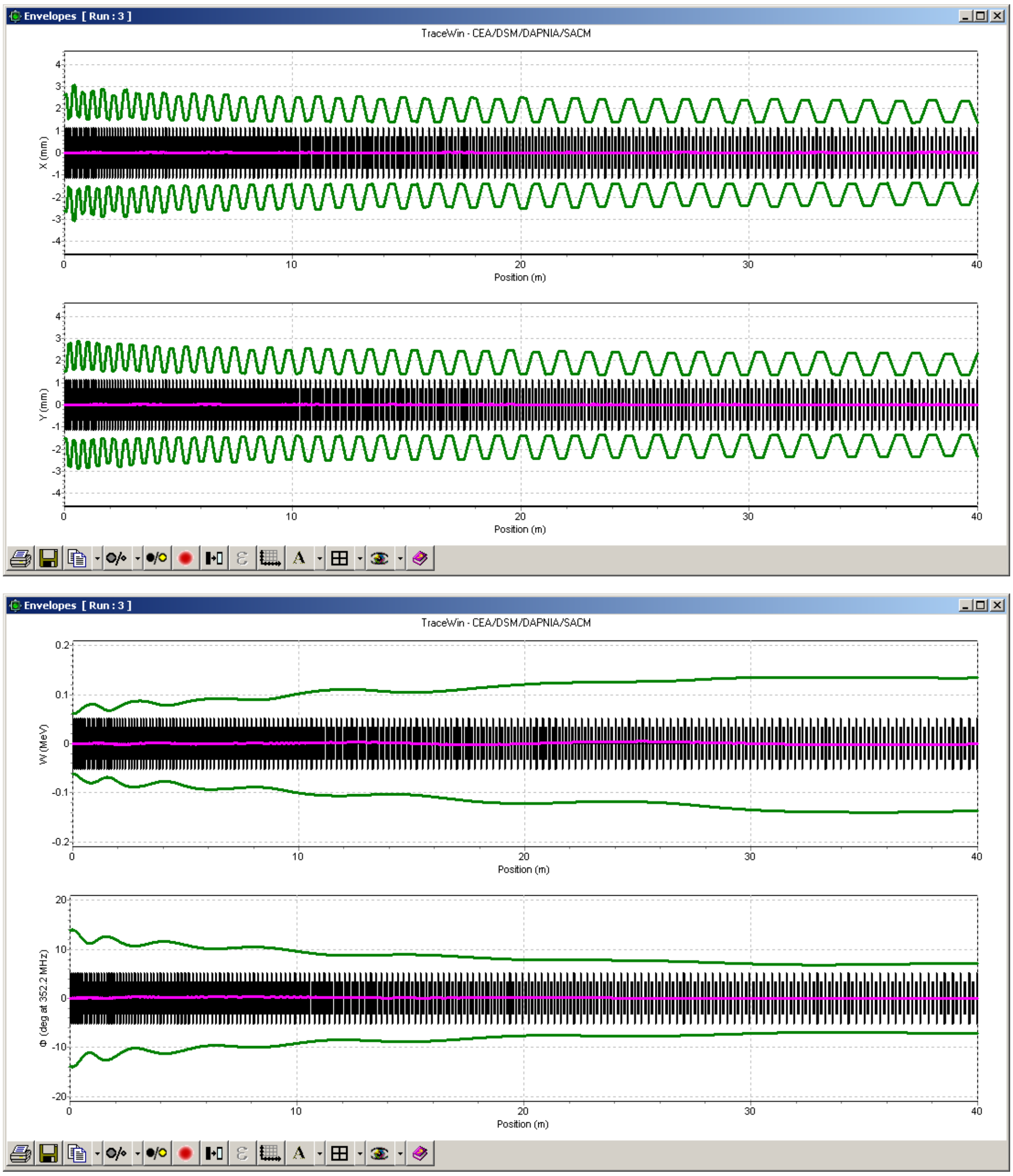

Figure 1.13: transversal and longitudinal beam envelopes along the SPES DTL.

The cooling system of the resonator is dimensioned for a duty cycle of 10%, so to leave open the development toward a higher power linac. The cooling water temperature is used for the tuning of the resonant frequency.

Mechanical design choices profit from experience at SNS and have been developed in collaboration with the Linac4 group an CERN. Indeed some important requirements of this linac (like the operating frequency and the duty cycle) are in common with LINAC4. Therefore, except for the details in the dimensions and position of the drift tube, the cavity can be the same for the CERN and LNL designs. In particular, the power couplers developed for CERN, based on slot coupling and planar RF window, are adopted.

The result of this collaboration is a mechanical design with simplified assembling and lower cost, materialized in the construction of a DTL prototype for high power tests, delivered at CERN in 2008, available for both projects.

In Figure 1.14 an inside view of the DTL prototype is shown. The drift tubes are in bulk copper, with e-beam welded water channels to allow full power RF tests. The rigidity of the system is guaranteed by the thick iron tube (copper plated) of the tank structure. The precision of the alignment of the drift tubes (about 0.1 mm) is reached with the machining of the aluminum drift tube girder on the top. Concerning the permanent magnet installation in the drift tubes, the magnet is in air and the drift tube is closed using laser welding. This approach minimizes the possibility of trapped volumes in vacuum. As an alternative a simpler construction will be developed, leaving the permanent magnets in vacuum, as is successfully in operation in the SNS Linac.

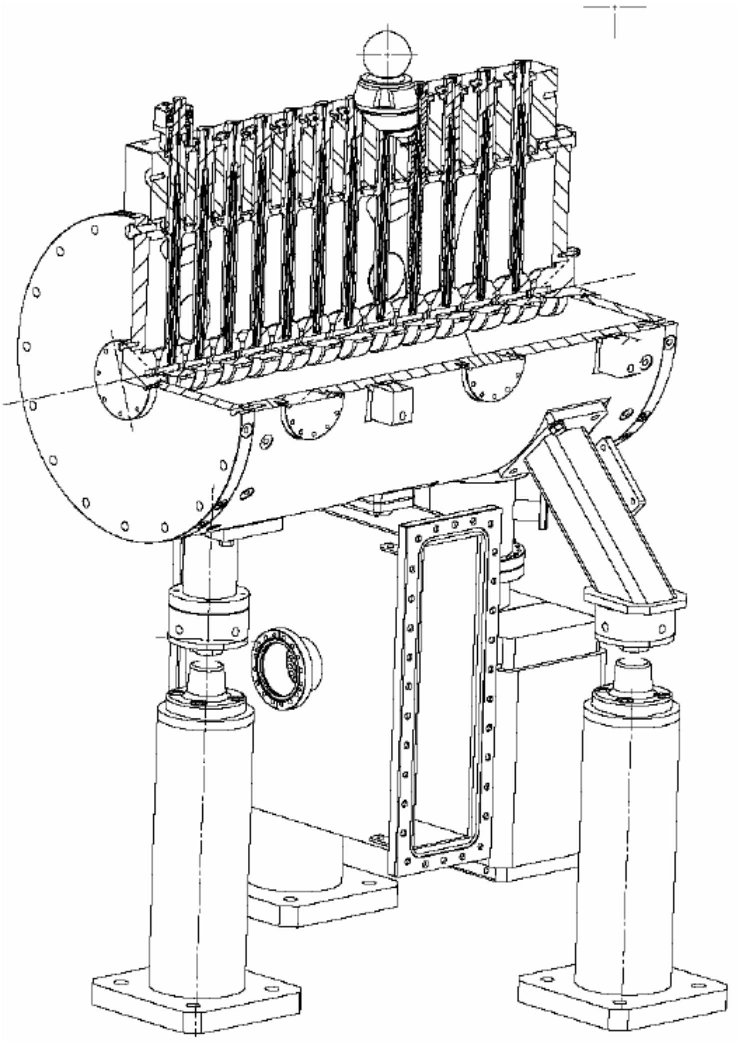

Figure 1.14: a drawing of the DTL prototype for high power tests built in collaboration between CERN and LNL.

References

[1] J. C. Cornell, "Radioactive ion beam facilities in Europe: current status and future developments", Proc. EPAC04.

[2] Y. Blumenfeld, "Radioactive ion beam facilities in Europe", NIM B, 2008, Vol. 266, 4074.

[3] G. Prete, A. Pisent (ed.), "SPES technical design report", INFN-LNL 220, 2007.

[4] A. Bracco, A. Pisent (ed.), "SPES technical design report", INFN-LNL 181/02, 2007.

[5] G. A. Lalazissis et al., "Reduction of the spin-orbit potential in light drip-line nuclei", Phys. Lett. B, 1998, Vol. 418, 7.

[6] A. Bracco, Lectures at Varenna, 2006.

[7] S. Leoni, "Lectures on Detectors for Nuclear Physics", 2007.

[8] A. Pisent et al., "Design of the high current linac of SPES project", Proc. EPAC08.

Chapter 2. The Linac4 Project

The normal conducting accelerator Linac4 is the first step of the CERN accelerator complex upgrade. The construction of Linac4 was approved in 2007 as a high priority project and will replace the existing Linac2.

In this chapter the motivations and related solutions for new accelerators at CERN are introduced and the Linac4 main parameters and accelerating structures are described. Finally we focus on the DTL structure, which will be the focus of this thesis.

2.1 New injectors at CERN

There are two main reasons leading to the upgrade of the proton injector complex at CERN: the reliability of the present injector chain and the LHC performance limitations [1,2].

The present injector chain of LHC is comprised of 4 accelerators (Figure. 2.1):

- *Linac2*, commissioned in 1978 and upgraded in 1993, with the replacement of the Cockroft-Walton with the present RFQ as pre-injector for the DTL. It accelerates protons up to 50 MeV at an operating frequency of 202 MHz.
- *Proton Synchrotron Booster* (PSB), the first circular accelerator of the complex, commissioned in 1972. It is a four ring synchrotron, accelerating protons from 50 MeV to 1.4 GeV.
- *Proton Synchrotron* (PS), switched on in 1959. It leads the proton beam up to 26 GeV energy.
- *Super Proton Synchrotron* (SPS), in operation since 1976. It can accelerate particles up to 450 GeV, the injection energy in LHC.

The original design parameters of these accelerators have been amply exceeded during the years of operation, in order to satisfy continuous new requirements of CERN users. The number of experiments using beams from these accelerators requires a very large machine time availability (e.g. Linac2 annual operation time is about 6000 hours!). Age, performance stretch and using time have gradually caused recurrent hardware problems during recent years (radiation damages in PS magnets, water leaks in SPS magnets, vacuum leaks in Linac2, etc.), which compromise the LHC operation reliability [2].

The present Proton Accelerator Complex can limit the future performances of LHC in term of luminosity for the experiments.

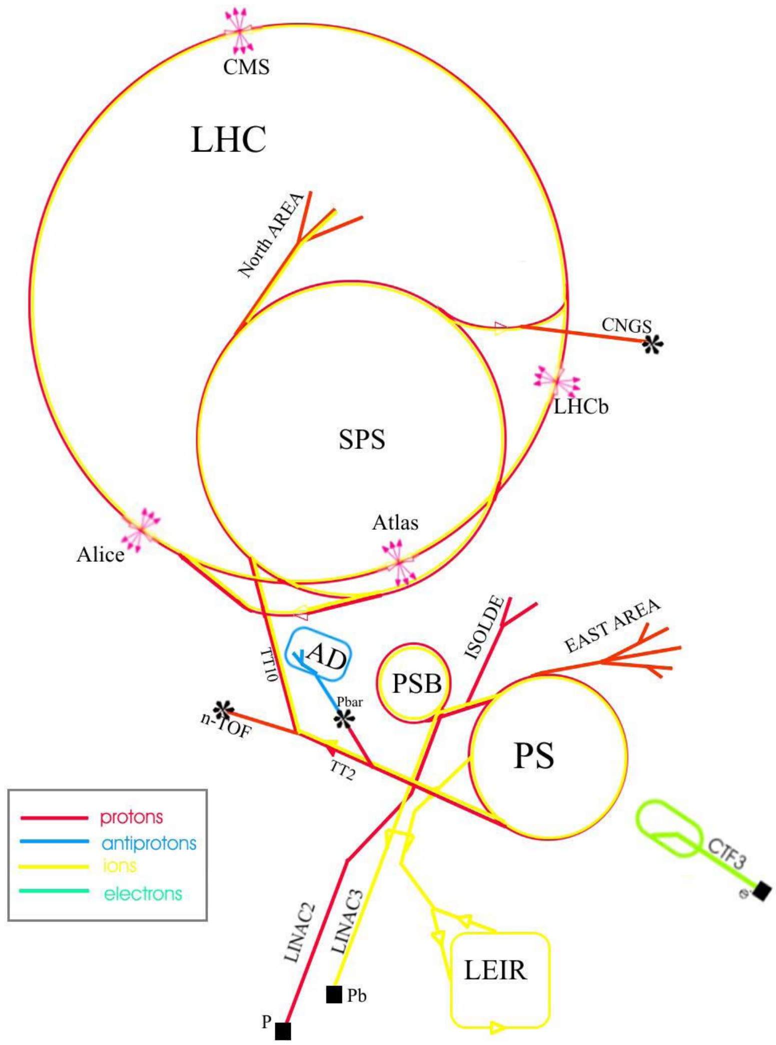

Figure 2.1: the present CERN accelerator complex.

Two levels of performance have been defined for the LHC, which correspond to two different sets of beam characteristics called "nominal" and "ultimate" (Table 2.1) [2]. The nominal LHC luminosity of 10^{34} $cm^{-2}s^{-1}$, sufficient for the initial phase of LHC operation, can be reached with the present injectors, but the ultimate luminosity of 2.3 x 10^{34} $cm^{-2}s^{-1}$ can be obtained only with an upgrade of the Proton Accelerator Complex [3].

An elementary definition of Luminosity can be

$$L \propto \frac{n_b \cdot f_{rev} \cdot N_b^2}{A(\varepsilon_x^*, \varepsilon_y^*)},$$

where n_b is the number of bunches, f_{rev} the frequency revolution, N_b is the number of particles per bunches (ppb) and A the beam cross section, expressed as a function of the transverse normalized emittances $\varepsilon^*_{x,y}$. Since all the other parameters are fixed, the ultimate luminosity value can be obtained only by increasing N_b at LHC collisions to 1.7×10^{11} ppb. This requires a higher beam brightness ($N_b/ \varepsilon^*_{x,y}$) in each accelerator of the injector chain.

			Injection	Collision
Energy		[GeV]	450	7000
Luminosity	Nominal Ultimate	[$cm^{-2}s^{-1}$]	-	10^{34} 2.3×10^{34}
Number of bunches (nb)			2808	
Bunch spacing		[ns]	24.95	
Particle per bunch (Nb)	Nominal Ultimate	[ppb]	1.15×10^{11} 1.70×10^{11}	
Circulating beam current	Nominal Ultimate	[A]	0.58 0.86	
Normalized transv. emittance ($\varepsilon^*_{x,y}$)		[µm rad]	3.5	3.75

Table 2.1: nominal and ultimate LHC beam parameters.

The bottle-neck for the generation of higher brightness beams has been identified with the incoherent space charge tune spread value at injection to the PSB [1,2]. The incoherent space charge tune spread is defined as

$$\Delta Q_{SC} \propto \frac{N_b}{\varepsilon^*_{x,y}} \cdot \frac{R}{\beta\gamma^2}$$

where R is the mean radius of the accelerator and β and γ are the classical relativistic parameters. As for the ultimate required brightness $N_b/ \varepsilon^*_{x,y}$, the value of ΔQ_{SC} becomes excessive at the injection energy of 50 MeV. In order to satisfy the ultimate performances and upgrade of the LHC, the brightness will be doubled by doubling the relativistic factor $\beta\gamma^2$, whilst maintaining the present ΔQ_{SC} value. This corresponds to a PSB injection energy of 160 MeV, provided by the new normal conducting proton linac, Linac4 [1,2,3].

Similar analysis of LHC performances, together with the necessity of reliable operation, are the basis of the gradual replacement proposed for the present injector complex, as sketched in Figure 2.2 and Figure 2.3 [1,2]. The only accelerator which will not be replaced is SPS. The first accelerator to be built is Linac4 (2008 start - 2013 commissioning).

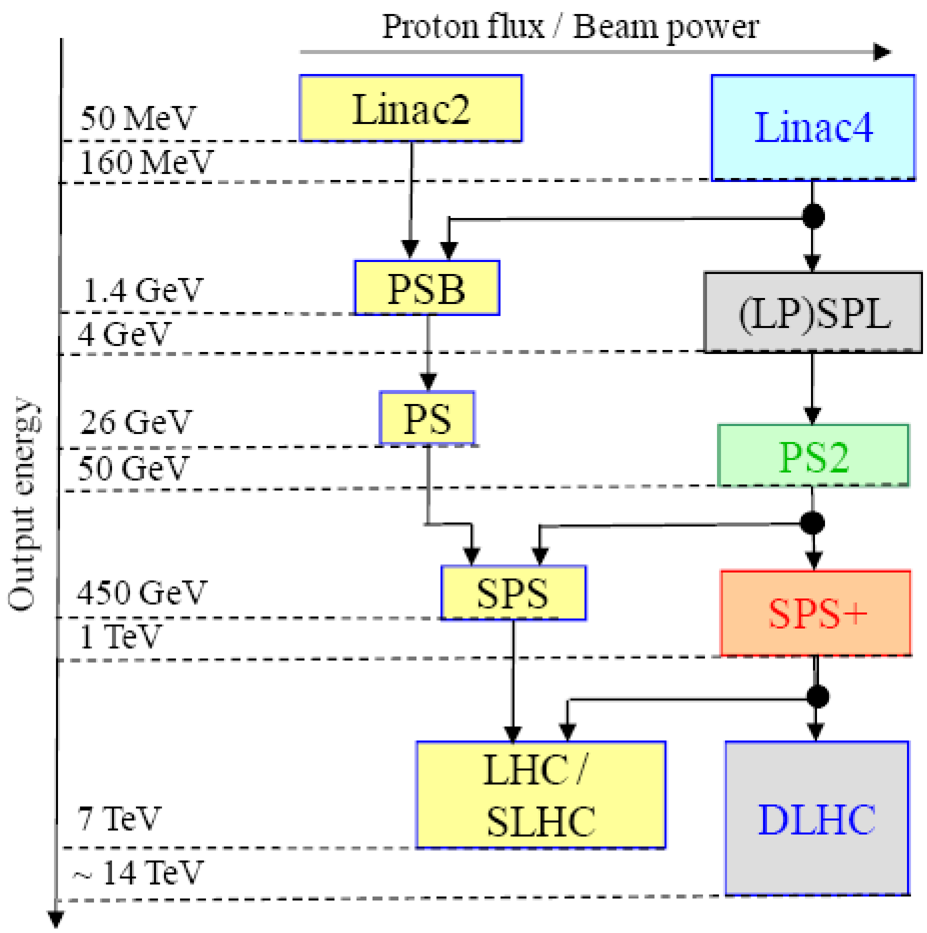

Figure 2.2: a scheme of present and future accelerators of the CERN complex. At the moment the only new accelerator approved and in construction is Linac4.

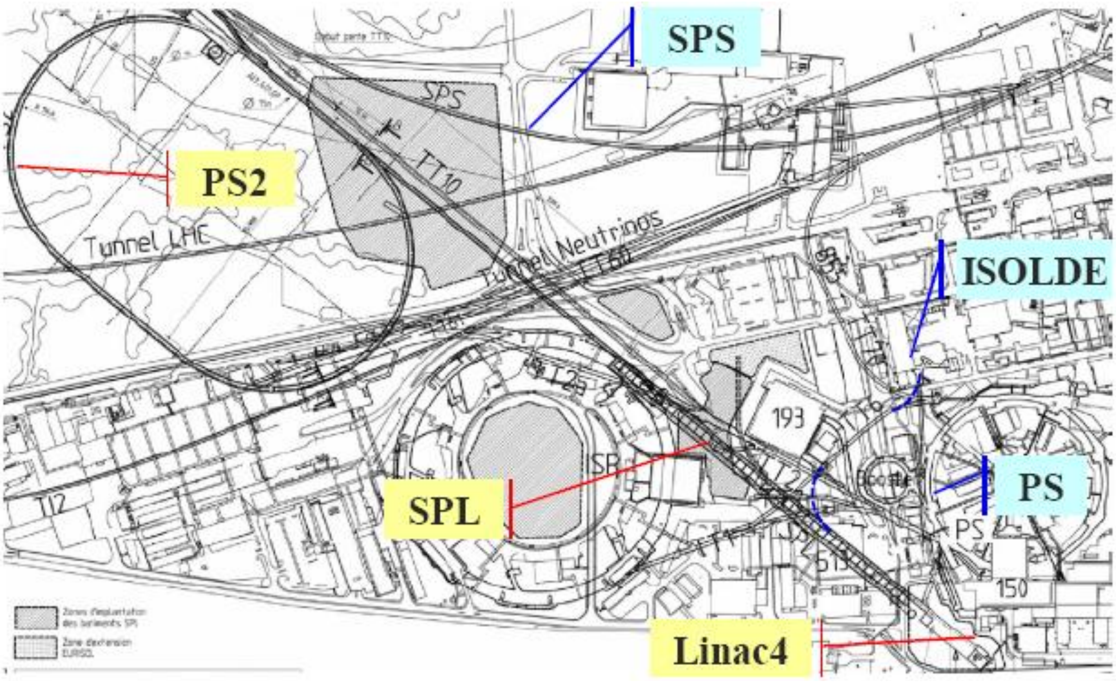

Figure 2.3: layout of the new complex.

The last remark is on the choice to build the new linacs (Linac4 and SPL) as H^- machines. The notable advance during the last 20 years of the technology of H^- sources and linear accelerators has allowed the upgrade to take advantage of the charge-exchange injection of H^- into the synchrotrons (PSB or PS2) using a stripping foil [3].

2.2 Linac4 RF structures

Linac4 parameters are listed in Table 2.2. They are mainly based on the PSB injection characteristics [3,4].

Parameter	
Ion species	H-
Source output energy	45 keV
Linac output energy	160 MeV
Bunch frequency	352.2 MHz
Max.rep. rate	2 Hz
Beam pulse length	400 μs
Max. beam duty cycle	0.08%
Chopper beam-off factor	37.5%
Source current	80 mA
RFQ output current	70 mA
Linac pulse current	40 mA
Average current	0.032 mA
Beam power	5.1 kW
Particles per pulse	1.00×10^{14}
Particle per bunch	1.14×10^{9}
Linac transverse emittance	0.4 π mm mrad

Table 2.2: Linac4 beam parameters.

The final energy is fixed in order to double the intensity in PSB, the 2 Hz repetition rate is given by the PSB frequency and the emittances are defined by the LHC needs. The maximum number of protons (in fact H^-) per pulse (10^{14} protons per pulse) is defined by the high intensity experiments served by this machine (e.g. ISOLDE). The average beam current is 2×10^{14} protons per second (2 Hz x 10^{14} protons per pulse), which corresponds to 32 μA. The average current during pulse is 40 mA and the pulse length is 0.4 ms. The beam duty cycle is 0.08% and considering an RF pulse of 0.5 ms, the RF duty cycle is 0.1%.

Nevertheless this machine is going to be the front end of the H^- SPL, which will provide a 4 GeV beam at repetition rate of 5 Hz (5% duty cycle). In order to keep a margin for future operations, all Linac4 accelerating structures are designed for a maximum duty cycle of 10%.

The RF frequency is determined by the availability of RF equipment at 352 MHz (klystrons, wave-guides, circulators) from the decommissioning of the LEP RF system. The operating frequency is the same for all the structures.

The chopping system located after the RFQ is devoted to stop a selected sequence of beam bunches, in order to avoid beam losses at high energy during longitudinal capture into the PSB buckets. Since the fraction of beam removed by the chopper is 37.5%, the pulse current before chopping has to be 64 mA. Including margins for beam losses in the transfer line, in the RFQ and in the chopper line, the RFQ output current is set at 70 mA and the source current at 80 mA.

The Linac4 scheme is shown in Figure 2.4 [4]. The total length of Linac4 is 80 m.

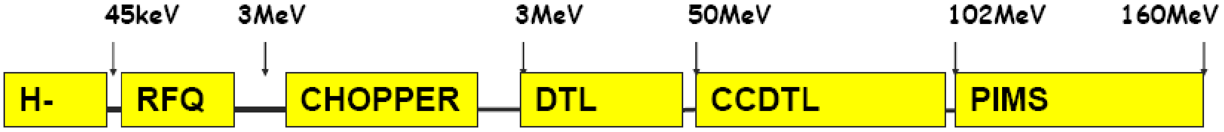

Figure 2.4: basic Linac4 architecture.

The H^- ion source delivers an 80 mA beam at 45 keV to the RFQ.

The RFQ is a 3 meter long structure, with a constant vane voltage of 81 kV and a maximum surface electric field of 35 MV/m, corresponding to 1.9 Kilpatrick. The transmission factor is 95% and the output energy is 3MeV, a compromise between the necessity of chopping at low energy for irradiation concerns and the requirement of starting the DTL at higher energy for mechanical constraints in the construction of the first drift tubes. The RFQ total peak power dissipation is 541 kW including beam [5].

After the chopper line, 3 different accelerating structures accelerate the beam up to 160 MeV: a Drift Tube Linac (DTL) up to 50 MeV, a Cell-Coupled DTL (CCDTL) up to 102 MeV and a π-mode structure (PIMS) up to the final energy of 160 MeV.

The DTL consists of 3 tanks with a very high shunt impedance (Figure 2.5), because the use of Permanent Magnet Quadrupoles (PMQs), for beam focusing allows the reduction of the drift tube diameter. Nevertheless, since PMQs do not offer any flexibility of adjusting the transverse focusing for different beam currents, the switch to the CCDTL is chosen at 50 MeV, where DTL would be still convenient according to the shunt impedance value [4]. The CCDTL is constituted by 7 modules, each consisting of 3 coupled DTL–type cavities and with 3 accelerating gaps. The 21 Electro-Magnetic Quadrupoles (EMQs) are located outside the tanks, at the coupling cavity position. Around 100 MeV the shunt impedance of structures with βλ period (0-mode structure), such as DTL and CCDTL, rapidly decreases because of the increasing drift tube length, and it is convenient to use structures with period βλ/2 (π-mode structure). The PIMS used by Linac4 is constituted by 12 modules of 7 cells, coupled to each other by two coupling slot. Beam focusing is provided by 12 EMQs located between tanks. The choice of the PIMS rather than the original Side Coupled Linac (SCL) reduces the number of cells from 468 to 74 and simplifies the tuning procedure [4].

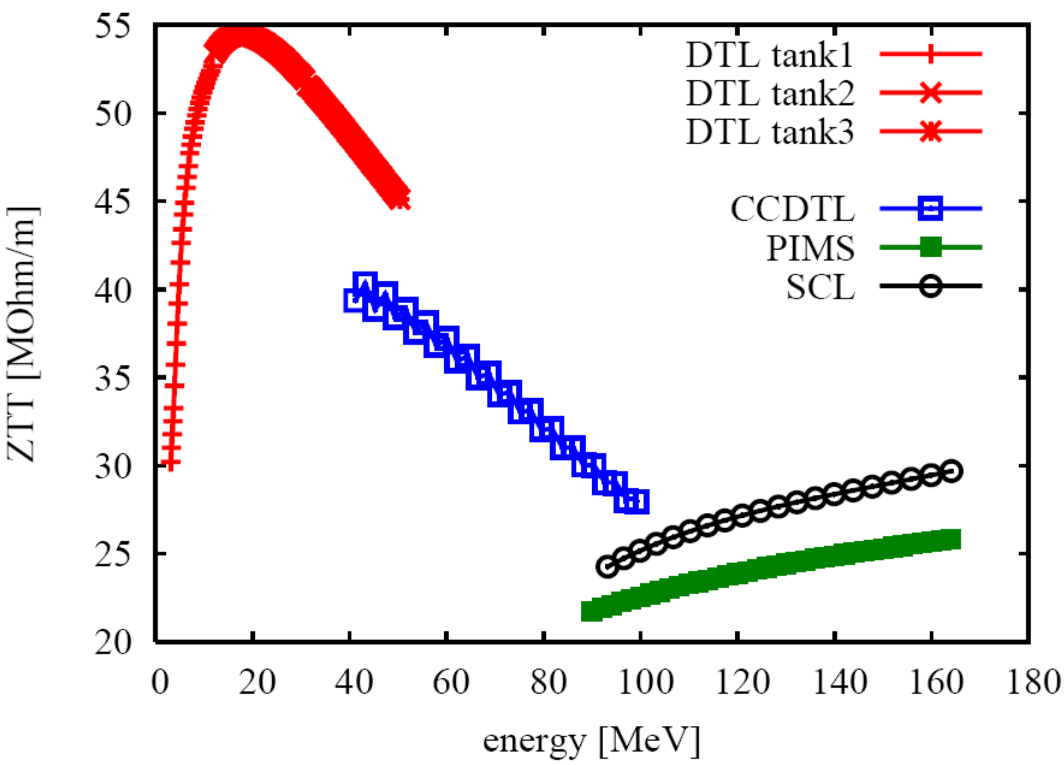

Figure 2.5: effective shunt impedance for Linac4 accelerating structures.

The RF system uses both 1.3 MW LEP klystrons and 2.5 MW new klystrons, designed for pulsed operation, as in the scheme in Figure 2.6. All accelerating structures use iris-coupling from a tangential wave guide to deliver RF power to the cavities [4].

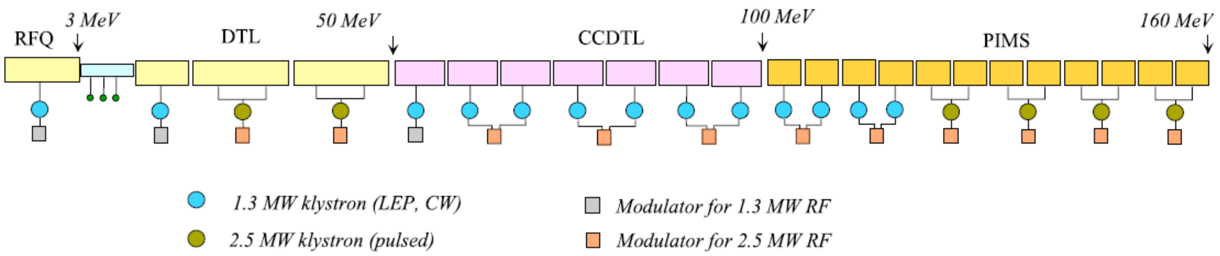

Figure 2.6: Linac4 RF system configuration.

2.3 The Linac4 Drift Tube Linac (DTL)

The DTL cavity parameters are summarized in Table 2.3 [3,4,6].

Parameter	Tank 1	Tank 2	Tank 3
Frequency [MHz]	352.2	352.2	352.2
Average pulse current [mA]	40	40	40
Design RF duty cycle	10%	10%	10%
Tank inner diameter [mm]	520	520	520
Drift tube diameter [mm]	90	90	90
Aperture radius [mm]	10	10	10
Length [m]	3.63	7.38	7.25
PMQ length [mm]	45	80	80
Focusing scheme	FFDD	FD	FD
Max. surface field [kilp]	1.6	1.4	1.3
Synchronous phase [deg]	-30/-20	-20	-20
Gradient E_0 [MV/m]	3.2	3.2	3.2
Final Energy [MeV]	12.18	31.80	50.00
RF peak power (incl. beam)[MW]	0.95	1.92	1.85
N. of klystrons	1 (1.3 MW)	1 (2.5 MW)	1 (2.5 MW)
N. of gaps	36	42	30
N. of Post Couplers	11	20	29
Stem diameter [mm]	29	29	29
Post coupler diameter [mm]	20	20	20

Table 2.3: Linac4 DTL parameters.

The Linac4 DTL is designed to accelerate pulses of 40 mA of H- ions from 3 MeV to 50 MeV. The structure is composed by 3 tanks with a total length of 18.7 m. The tank diameter is 520 mm and the drift tube diameter is 90 mm, with a beam aperture of 20 mm.

The beam focusing is provided by PMQs installed inside the drift tubes. The choice to use PMQs keeps the drift tube size small and avoids current wires and additional power supplies. Increased flexibility of the focusing system is obtained by placing electromagnetic quadrupoles in each of the intertank spaces.

The average electric field E_0 is constant at 3.2 MV/m over all gaps, which simplifies the tuning procedure and results in a more compact design, because of the relatively high field value. The choice of a constant average field E_0 is different with respect to other similar facilities (Linac2, SNS, J-Parc), where the field is ramped in the first cells in order to keep a lower peak field and reduce RF breakdown risks. In the Linac4 DTL the peak field in the first cells has been reduced by 30% by increasing the gap length, but without affecting the desired constant E_0 value. The Kilpatrick limit at 352.2 MHz is 18.4 MV/m and the bravery factor for DTL is 1.7, reduced to 1.2 in the initial cells [6] (Figure 2.7) .

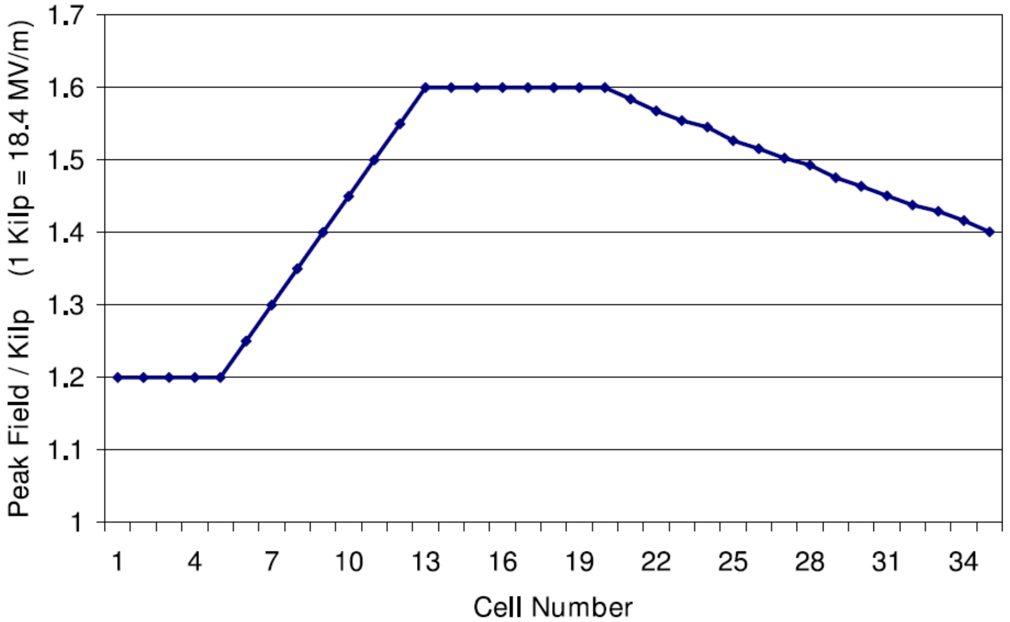

Figure 2.7: peak electric field in the first cells of tank 1.

Together with the high accelerating gradient E_0, a more aggressive law for the synchronous phase has been chosen to reduce the structure length. The synchronous phase is ramped from -30° to -20° in the first 20 cells and then kept constant -20° to the end, values that have to be compared with typical values of -45° and -25°.

The RF power for tank 1 is provided by one 1.3 MW LEP klystron via a coupling iris, accurately matched to the cavity by the adjustable short-circuit which terminates the waveguide at λ/4 from the iris hole center. Tank 2 and tank 3 need one 2.5 MW klystron each, with 2 coupling irises per tank [4]. Each coupling iris transmits about 1MW to the cavity and has been simulated using 3D electromagnetic codes, in order to compute dimensions and surface power densities (Figure 2.8).

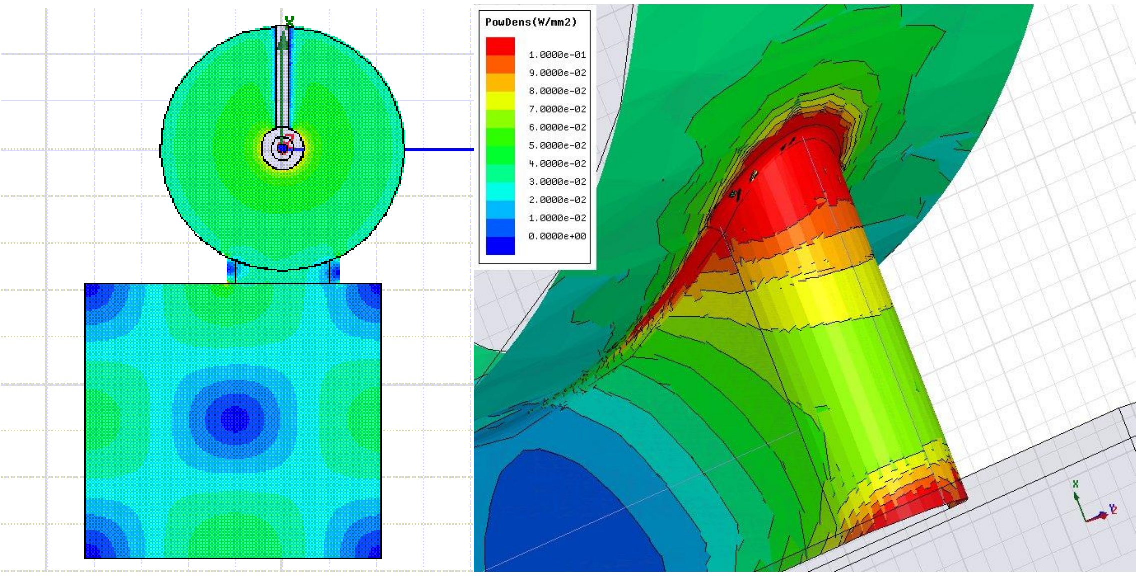

Figure 2.8: 3D simulation results of the DTL prototype coupling iris, with a zoom on the maximum power density area.

Mechanically, the DTL is assembled starting from up to 2 m long steel cylinders. Each cylinder has a rectangular slit on the top with holes for each drift tube in order to slot the aluminum girder which support drift tubes. Vertical and horizontal references for drift tube positioning are defined by 2 steel positioning rings inserted into the girder. After tank and girder are assembled together, drift tubes are mounted into the girder, without the possibility of further alignment. If a major alignment fault is detected, it can be only corrected by re-machining one of the positioning rings [4,6].

A full-scale prototype [6] of the first section of tank 1 has been built in order to test mechanical choices, manufacturing and assembly procedure, vacuum sealing and to fix concerns related to high RF power operation (coupling iris, cooling system, heating spot, RF breakdown).

The tuning of the Linac4 DTL can be divided in 3 main points:

- field flatness, obtained by the precise drift tube alignment in the assembly phase and slightly adjusted using slug tuners;
- frequency tuning, obtained by setting fixed slug tuners and moving adjustable tuners during operation;

- field stabilization, provided by post couplers.

Slug tuners are placed at 45° with respect to stem position. The present configuration foresees about 3 tuners per meter. Post coupler distribution foresees one post coupler every 3 drift tubes in tank 1, one post coupler every 2 drift tubes in tank 2 and one post coupler every drift tube in tank 3. These configurations correspond respectively to 3.3, 2.8 and 4.1 post couplers per meter. The small drift tube diameter, allowed by the small PMQ size, has the advantage of increasing the shunt impedance, but at the same time the distance between drift tube and tank is larger than $\lambda/4$ (1.01 $\lambda/4$), considered to be critical for achieving field stabilization. The stabilization effectiveness of this post coupler configuration has been verified in detail with 3D simulations and with a dedicated aluminum scaled prototype, showing that stabilization can be achieved [6,7].

References

[1] R. Garoby, "Upgrade issues for the CERN accelerator complex", Proc. EPAC08.

[2] Interdepartmental working group on "Proton Accelerators for the Future" (PAF), http://paf.web.cern.ch/paf/.

[3] F. Gerigk, M. Vretenar (ed.), "Linac4 Technical Design Report", CERN-AB-2006-084 ABP/RF.

[4] F. Gerigk et al., "RF structures for Linac4", Proc. PAC07.

[5] A. M. Lombardi, C. Rossi, M. Vretenar, "Design of an RFQ Accelerator optimised for Linac4 and SPL", CERN-AB-Note-2007-027.

[6] S. Ramberger et al., "Drift Tube Linac Design and Prototyping for the CERN Linac4", Proc. LINAC08.

[7] N. Alharbi, F. Gerigk and M. Vretenar, "Field Stabilization with Post Couplers for DTL Tank1 of Linac4", Tech. Rep. CARE-Note-2006-012-HIPPI, CARE, 2006.

Chapter 3. Drift Tube Linac and Resonant Coupling

In this chapter we briefly introduce some concepts about resonant cavities and linear accelerator structures

The Drift Tube Linac (DTL) cavity is a common accelerating structure at ion facilities since the end of World War II. DTLs are efficient at providing the second acceleration step for ions, in the velocity region of $0.1 < \beta < 0.5$, corresponding to proton kinetic energy W of 3 MeV < W < 150 MeV. For reasons of RF power saving it is convenient to build a long DTL tank, but this choice involves risks of accelerating field instability. This problem has been fixed by using the resonant coupling stabilization method and equipping DTL cavities with enigmatic coupled resonators, called post couplers.

3.1 Alvarez Drift Tube Linac (DTL)

The Drift Tube Linac (DTL) is an accelerating structure proposed by L. Alvarez in 1946 [1], consisting of an array of drift tubes on the beam axis, suspended from the cavity tank by supporting stems (Figure 3.1).

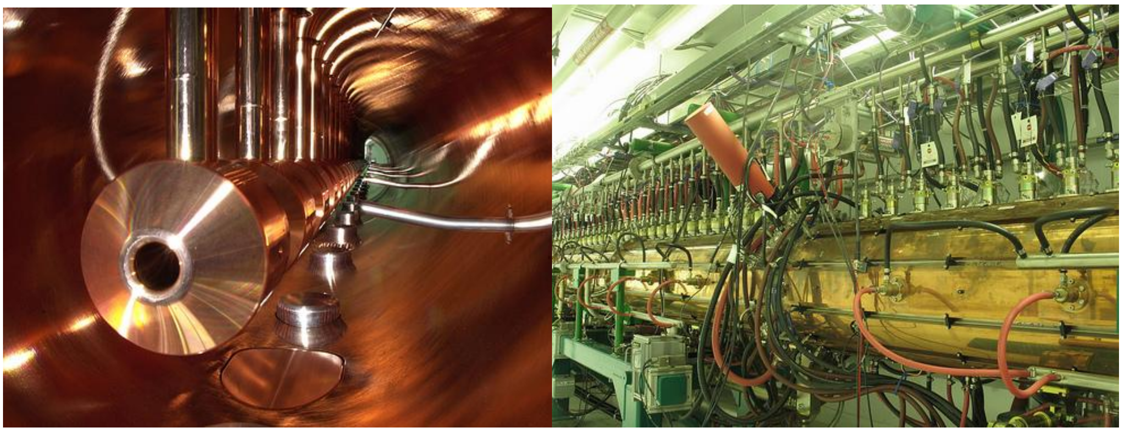

Figure 3.1: internal and external view of the SNS DTL.

Starting from a pillbox cavity [2,3] operating at the TM_{010} resonant mode, where the electric field is uniform along the beam axis z of the cavity, a reentrant gap is introduced to concentrate the electric field in the beam axis region and therefore to increase the accelerating efficiency of the structure. Now a set of identical single-cell cavities are concatenated to form a multigap accelerator (Figure 3.2). If the RF fields in all the cavities are phased to be identical in time and the cavities are dimensioned such that the space between gaps is $\beta\lambda$, by the time the ion transits from one gap to the next the field has progressed by one wave and the ion experiences an accelerating field in each gap. Since the cavities are all in synchronism, the velocity at each point is fixed: the Alvarez structure is inherently a fixed-velocity structure.

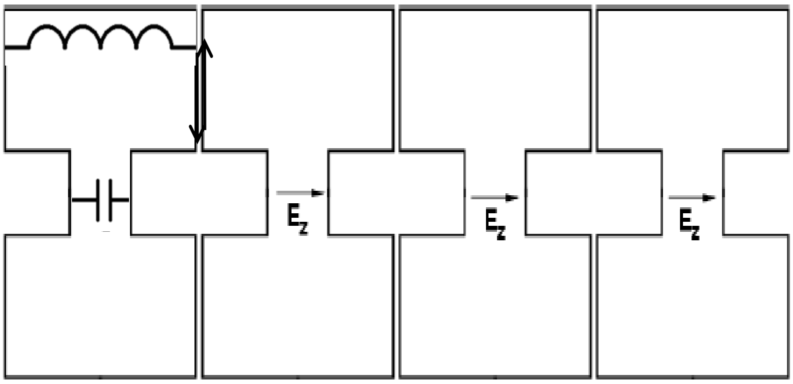

Figure 3.2: a single cell cavity array. Wall currents and lumped circuit elements are shown.

The accelerator is now an array of single cavities all in phase, but this configuration can be improved. In the TM_{010} mode currents flow along the walls, heating them and requiring RF power. The fields on each side of the walls separating each cell are identical in amplitude and direction, so the walls separating the cells can be removed and the drift tubes suspended on stems (Figure 3.3).

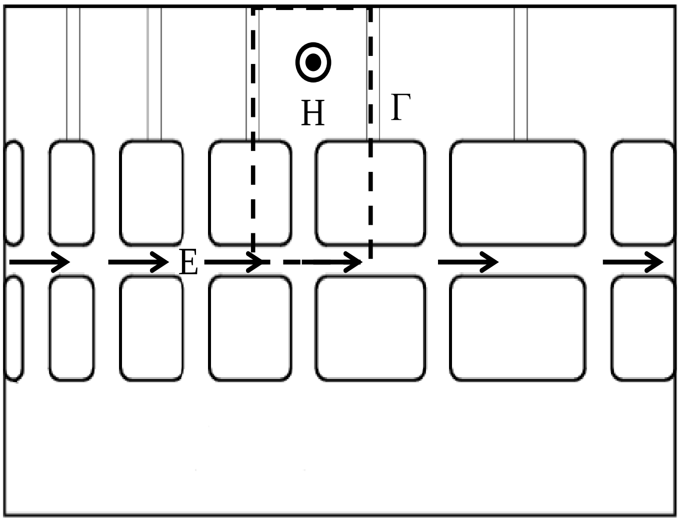

Figure 3.3: in a DTL cavity separating walls are removed, and drift tube are supported by stems.

This is one way to look the DTL: a series of single-cell cavities all in phase, where the separating walls are removed without altering the field configuration.

We can also consider the DTL as a long pillbox cavity with the electric field along the axis. If the cavity is made longer than the distance a particle travels in half an RF period (βλ/2), the particle is both accelerated and decelerated as well. If hollow drift tubes are installed along the axis the particle will be inside a Faraday Cage that shields the particles when the polarity of the axial field is opposite to the beam direction. The drift tubes divide the cavity into cells of length βλ. As the particles gain energy at each gap, the cell lengths increase with β. Because the fields in all the cells are in phase, the Alvarez DTL structures operates in a 0 mode, where zero refers to the cell-to-cell field phase difference at a fixed time.

An interesting quantity for accelerator design is the average axial field E_0 for a single accelerating cell defined as

$$E_0 = \frac{V_0}{L_{cell}} = \frac{\int_{Lcell} \overline{E}(0,z)d\overline{z}}{L_{cell}}.$$

If we apply the Faraday's law to the rectangular path Γ in Figure 3.3, we have

$$\int_{\Gamma} \overline{E} \cdot d\overline{l} = -\frac{\partial}{\partial t} \int \overline{B} \cdot d\overline{A}.$$

Since the line integral of the electric field is nonzero only on the beam axis path, the left side of the equation is

$$\int_{\Gamma} \overline{E} \cdot d\overline{l} \equiv \int_{\beta\lambda} \overline{E}(0,z)d\overline{z} = V_0 = E_0 \beta\lambda .$$

The integral on the right side is $-\frac{\partial}{\partial t} \int \overline{B} \cdot d\overline{A} = -j\omega\Phi$ where Φ is the magnetic flux.

Therefore the magnitudes of the left and the right sides are related by $E_0\beta\lambda = \omega\Phi$. E_0 is proportional to the magnetic flux per unit length of the cell. Frequently DTLs are designed in order to have constant E_0 for all the cells and, in a structure with constant tank diameter and constant drift tube diameter, this can be obtained with the same radial distribution of B along the cavity. Generally, DTLs with constant E_0 have different peak electric field in the gaps and different peak surface electric field, depending on the cell length and geometry.

Coming back to the cavity cell description in Figure 3.2, each cavity can be seen as a lumped circuit whit a capacitance on the drift tube gap, and an inductance associated to the current loop from one drift tube to the outer walls and back to the other drift tube, becoming displacement current in the gap. An approximate value of the capacitance can be calculated with the parallel plate formula $C_0 = \varepsilon_0 \pi d^2 / 4g$ and the inductance with the coaxial inductance formula $L_0 = \mu_0 \beta\lambda \ln\left(D/d\right)/2\pi$ where βλ is the cell length, d is the drift tube diameter, D is the tank diameter and g is the gap. The cell resonant frequency is $\omega_0 = 1/\sqrt{C_0 L_0}$.

As the cell length increases with β along the structure, the lumped circuit inductance L_0 increases as well. In order to keep the resonant frequency constant, the capacitance must decrease with increasing the gap size. The lumped circuit formulas are not accurate enough for a quantitative dimensioning of DTL cells, which can be designed using 2D or 3D simulation codes for RF design (Figure 3.4).

The drift tubes are supported to the outer tank by stems. There is no net current on the stems, but the time varying magnetic field causes eddy currents and consequently an additional power dissipation. Stems are not necessary for the electromagnetic design of a DTL, but they are mechanically essential for drift tube support, alignment and cooling. Focusing quadrupole magnets are located inside the drift tubes and their dimension gives an inferior limit for drift tube length and diameter (Figure 3.5). The gap-to-gap cell spacing is βλ, and a typical geometry is gap = ¼ βλ, drift-tube = ¾ βλ and quadrupole magnet = ½ βλ.

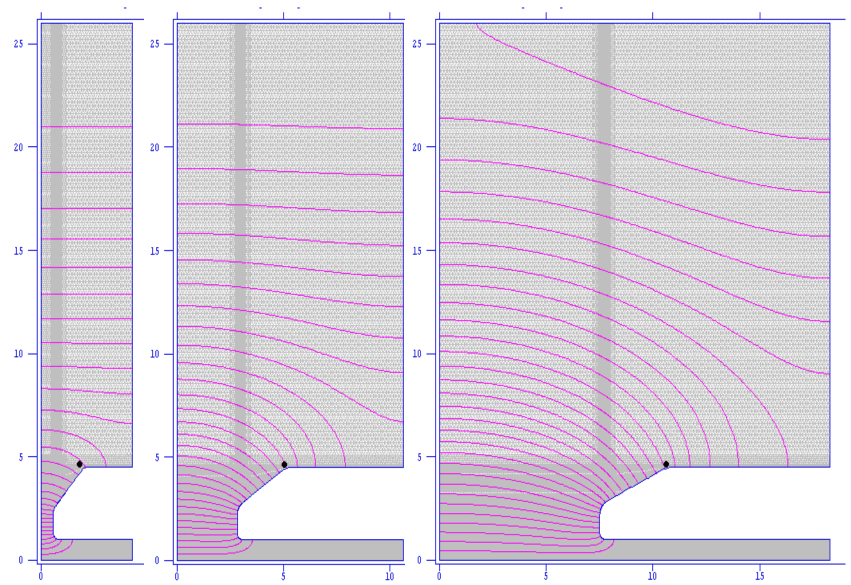

β=0.1 β=0.25 β=0.43

Figure 3.4: DTL cells at different β values designed with SUPERFISH 2D code.

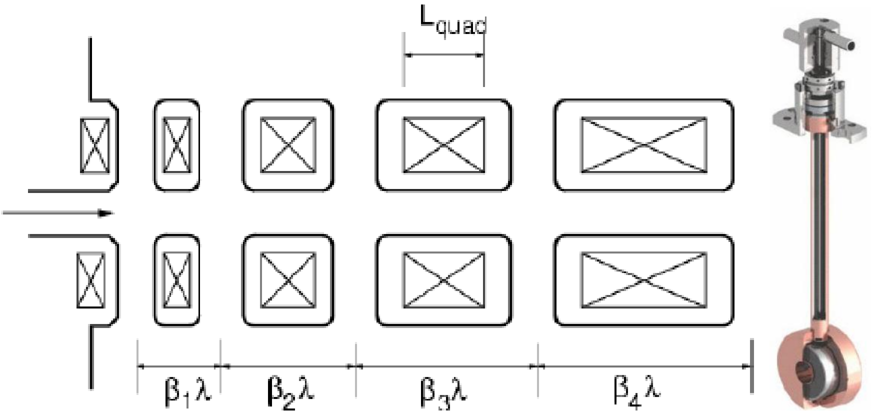

Figure 3.5: focusing quadrupole magnets are located inside the drift tubes.

3.2 Resonant Coupling

In a periodic accelerating structure composed of identical cells (as a DTL) the resonant modes can be classified depending on the field phase shift θ per period. For example, in the DTL working mode θ = 0, but it is also possible to excite modes where θ = π/2 or θ = π (Figure 3.6). In a biperiodic structure, where there are 2 kinds of alternating cells, we can distinguish the phase shift θ between identical cells and the phase shift ϕ between different cells, which satisfy the relation θ = 2ϕ (Figure 3.7). There is no agreement about the mode nomenclature in literature. For example, some authors would consider the case in Figure 3.8 a π/2 mode by analogy with the single periodic structure, we prefer to consider it a π mode, referring to the full period of the structure [4].

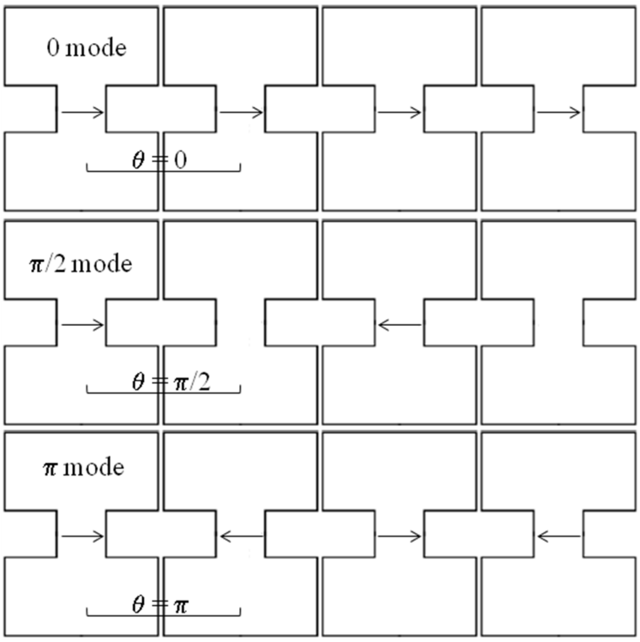

Figure 3.6: 0, π/2 and π mode in an array of identical cells.

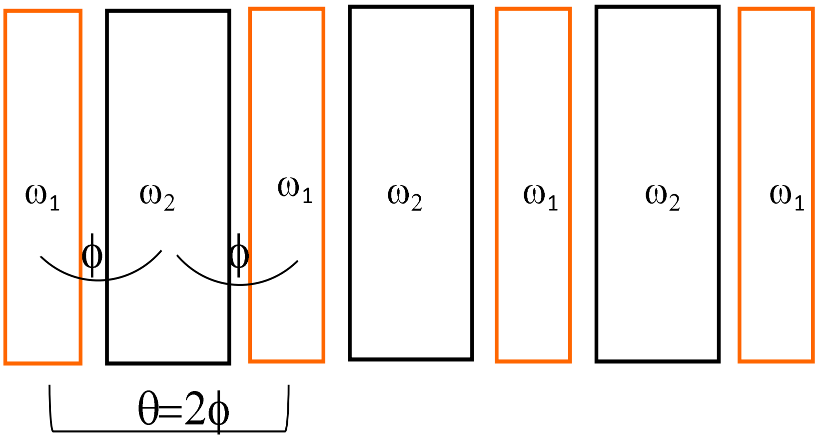

Figure 3.7: mode phase shift in a biperiodic structure.

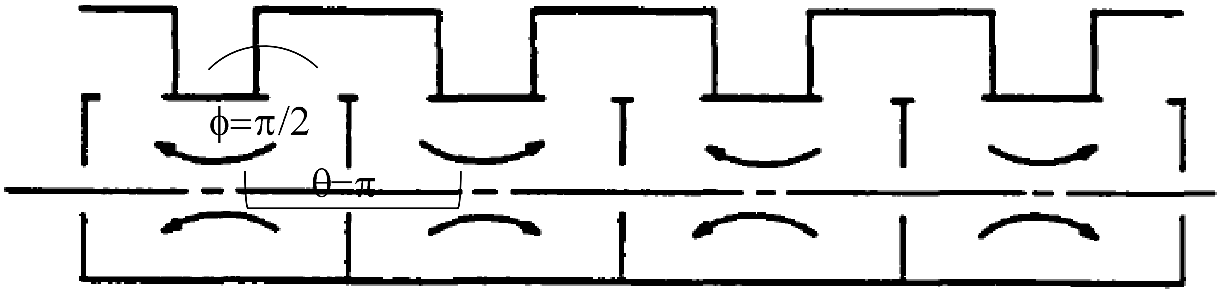

Figure 3.8: a π mode in a biperiodic structure.

The nominal field distribution in a real accelerating cavity is perturbed by inevitable wall losses, manufacturing error and beam loading. It is easy to show [5], using a coupled resonant circuit model, that in a chain of identical coupled cavities the $\pi/2$ mode field has low sensitivity to frequency errors (manufacturing), power losses (walls) and transient conditions (beam loading). These unique properties are related to the central location of the $\pi/2$ mode in the mode dispersion curve, because at this point the mode spacing and the dispersion curve slope are maximum, which reduces the close mode perturbation and increases the power flow along the structure.

These interesting properties of the $\pi/2$ mode can be introduced in structures working in 0 mode or π mode by providing the structure with a second chain of resonators used as unexcited coupling elements between accelerating cavities (Figure 3.9). The general approach of using resonant oscillators as coupling elements to stabilize the field distribution of a multicell standing-wave cavity is called resonant coupling [5, 6].

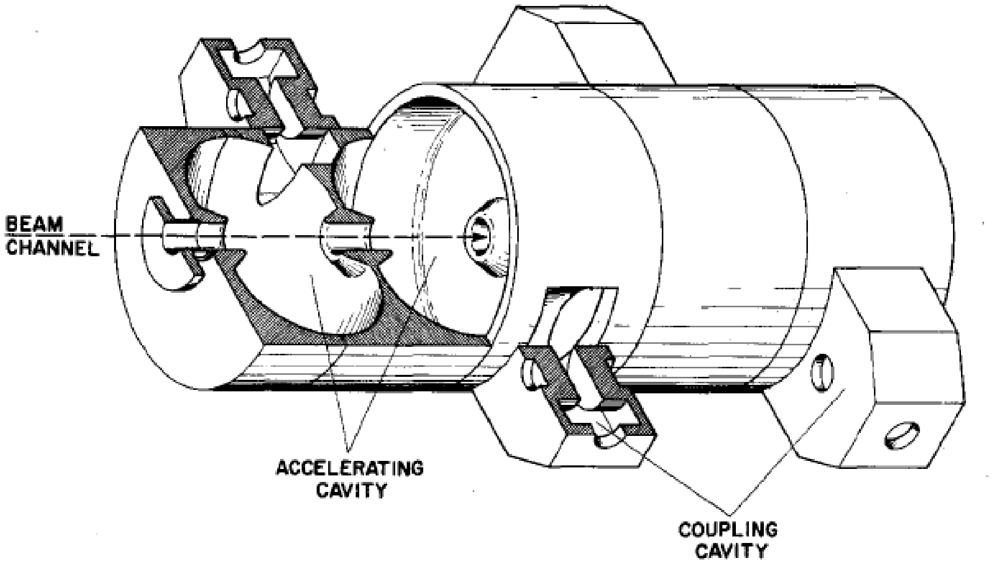

Figure 3.9: in a side coupled linac accelerating cavities are coupled by external coupling cavities.

Because of the existence of a second resonator chain, the dispersion curve has now 2 passbands, separated by a stopband. If the cavities are tuned in order to remove the stopband, the structure gets the desired $\pi/2$ mode properties. Such a joining up of two passbands is called confluence point. A structure where the operating point (0 or π mode) is the confluence point is called a compensated or stabilized structure. The stopband can be completely eliminated only in an infinite structure. In terminated structures only the accelerating cavity mode can be excited at the confluence point, the coupling cavity mode being forbidden because of boundary conditions [4] (Figure 3.10).

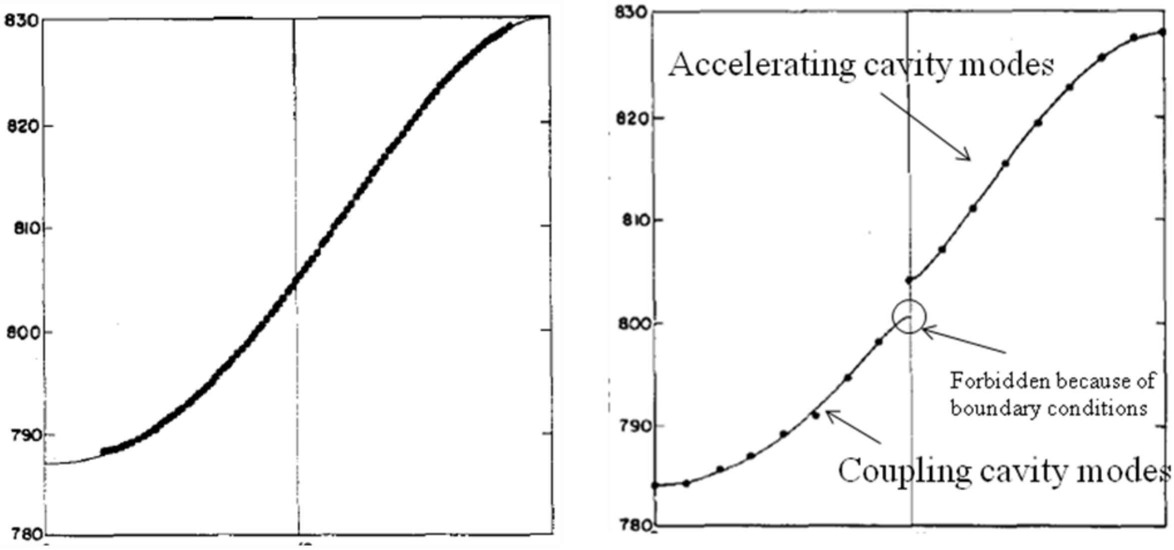

Figure 3.10: dispersion curve of an infinitely long coupled structure (left) and for a terminated coupled structure.

The resonant coupling principle, originally developed for the Side Coupled Linac (Figure 3.9), has been applied to other accelerating structures. The most common resonantly coupled structures are listed in Table 3.1.

Structure	Coupling element	Mode at confluence
Side Coupled Linac	Side cavity	π
Multistem DTL	Stems	0
Post Coupled DTL	Post couplers	0
Segmented RFQ	Coupling cell	0

Table 3.1: some resonantly coupled structures.

3.3 Post Coupled DTL

DTL cavities operate in the TM_{010} mode. The fields in all the cells have the same phase, so that the overall cell array operates in a 0 mode. The group velocity of a resonating mode is proportional to the slope of the dispersion curve at that point, being $v_g = \partial\omega / \partial k_z$. Since the group velocity of the TM_{010} mode is zero, there is no power flowing along the structure and the field distribution is very sensitive to frequency perturbations of the cells, power losses and beam loading. This problem is particularly serious for long DTLs, where the frequency separation between modes is lower.

A solution has been proposed in 1960's at Los Alamos [7], applying the resonant coupling method. In this case the resonant coupling elements are simple internal metallic bars, which extend from the outer cylinder towards the drift tube, without touching the latter (Figure 3.11). These bars are called Post Couplers (PCs).

The post couplers are located at the points on the outer wall of the cavity that are aligned with the centers of the drift tubes, and oriented at 90° with respect to the stems, in order to minimize the coupling between posts and stems. Furthermore, the nature of the coupling between adjacent PCs is such that they must be placed on opposite sides of the cavity (Figure 3.11).

The system, composed of two chains of coupled resonators, has two bands of frequencies: the TM band and the PC band (Figure 3.12).

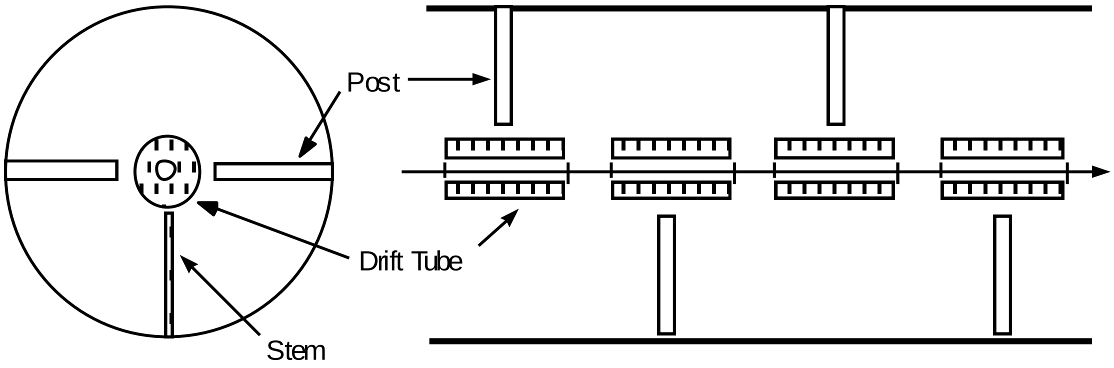

Figure 3.11: post couplers inside a DTL cavity.

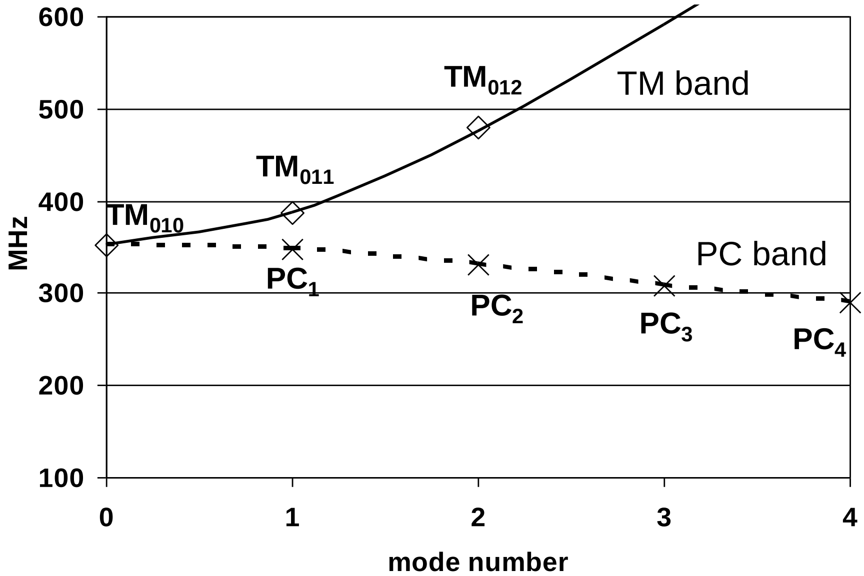

Figure 3.12: TM band associated to the accelerating cells and PC band associated to post coupler resonators.

The confluence mode of the TM passband and the PC passband is the 0 mode. However, since the PC mode field distribution correspond to a capacitively loaded TE mode, the PC 0 mode cannot be excited in a real tank with conducting end walls, but it is allowed only in an infinite structure (Figure 3.13). The PC 0 mode has the electric field from post couplers to drift tubes all with same direction and magnitude as it can be simulated using perfect magnetic end walls. In case of metallic walls the electric field magnitude is not the same for each post coupler, therefore this is not a “pure” 0 mode.

Figure 3.14 shows simulated TM and PC bands of structures in Figure 3.13. The plot distinguishes between modes allowed with perfect magnetic boundary conditions and modes allowed with perfect electric boundary conditions. It is interesting to notice that the three PC modes simulated with perfect electric boundary conditions have the same frequencies as the three central modes of the PC band simulated with perfect magnetic boundary conditions.

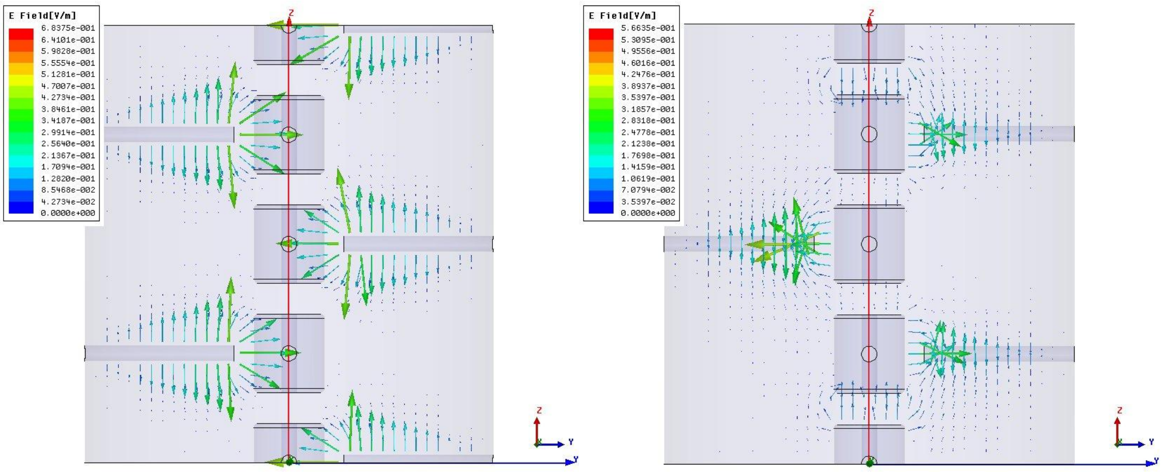

Figure 3.13: the PC 0 mode can be simulated only with perfect magnetic end walls (left). With metallic end walls (right) it is not possible to excite a “pure” PC 0 mode.

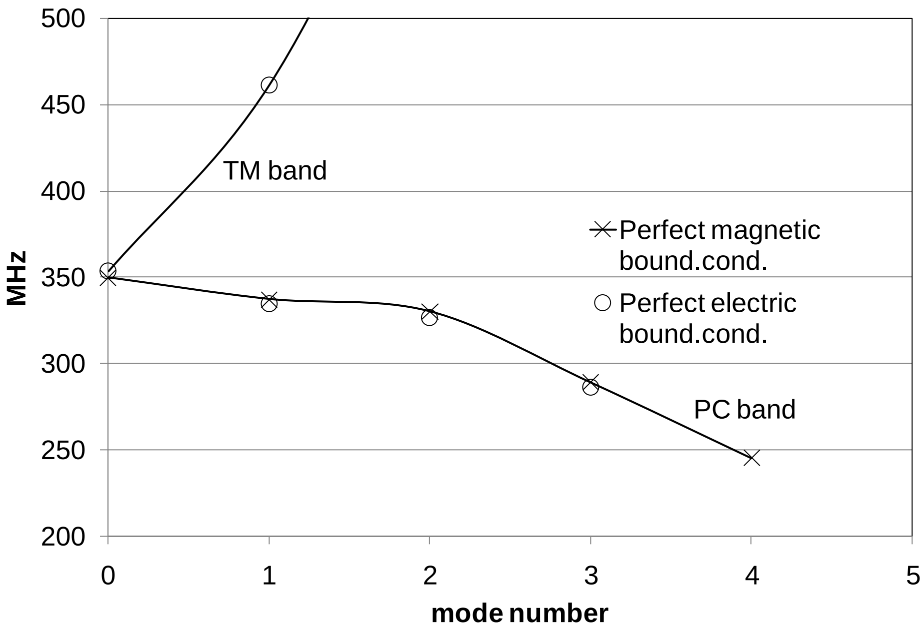

Figure 3.14: dispersion curves simulated with perfect electric boundary conditions and with perfect magnetic boundary conditions in a DTL with post couplers (Figure 3.13).

The coupling between post couplers and DTL accelerating cells is provided by the capacitance from the end of PCs to the drift tube walls. The coupling is stronger if the gap between PCs and drift tubes is small. The tuning of the coupling element resonance to get the confluence point can be done by adjusting the distance between post couplers, for example, changing the number of post couplers per drift tube. Once this parameter is determined, it is still possible to tune the post couplers frequency by changing the gap size between post couplers and drift tubes. It is clear that a variation of the gap changes the capacitive coupling strength as well.

There is a complication for the DTL post coupled structure with respect, for example, to the side coupled structure: the tuning of the coupling strength between elements and the resonance frequency tuning are dependent on each the other.

References

[1] L. W. Alvarez, “The Design of a Proton Linear Accelerator”, Phys. Rev., 1946, Vol. 70, 799.

[2] J. Staples, Lectures at USPAS, June 2007.

[3] T. Wangler, “RF Linear Accelerators”, John Wiley & Sons, Inc. 1998, par.4.4.

[4] G. Dôme, “Review and survey of accelerating structures”, in “Linear Accelerators” (ed. by P. Lapostolle and A Septier) North-Holland Publ.Co., 1969.

[5] D. E. Nagle, E. A. Knapp, B. C. Knapp, “ Coupled Resonator Model for Standing Wave Accelerator Tanks”, Rev. Sci. Instrum., 1967, Vol. 38, Number 11.

[6] E. A. Knapp, B. C. Knapp, J. M. Potter, “Standing Wave High Energy Linear Accelerator Structures”, Rev. Sci. Instrum., 1968, Vol. 39, Number 7.

[7] D. A. Swenson, E. A. Knapp, J. M. Potter, E. J. Schneider, “Stabilization of the Drift Tube Linac by Operation in the $\pi/2$ Cavity Mode”, Proc. 6th International Conference on High Energy Accelerators, 1967.

Chapter 4. Post couplers: simulation results

A 1034 mm long DTL prototype (Figure 4.1) [1] for high power tests has been built by CINEL for Linac4 project in collaboration with INFN, Legnaro. The operating frequency is 352.2 MHz and the average field is 3.3 MV/m. It consists of 13 cells with a tank diameter of 520 mm and a drift tube (DT) diameter of 90 mm. The cell length increases along the prototype corresponding to beam energy going from 3 MeV to 5.4 MeV. One post coupler (PC) every three DTs is placed at the longitudinal position of the 2nd, 5th, 8th and 11th DT for field stabilization. The PC diameter is 20 mm [2].

In this chapter we present 2D and 3D simulations and low-power RF measurements performed on this DTL "hot" prototype. The study of PC influence on this structure has the objective of better understanding the PC stabilization mechanism and defining a PC tuning strategy for tank stabilization.

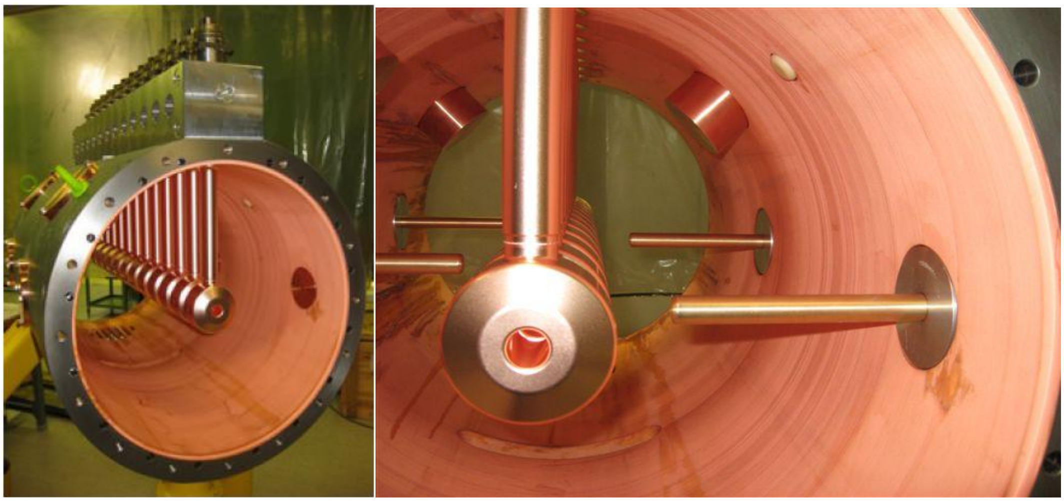

Figure 4.1: Linac4 DTL prototype for high power tests, built in collaboration with INFN-LNL. In the right side he four Post Couplers are shown.

4.1 Slater perturbation theorem calculation versus measurements

Since PCs should have a negligible effect on the nominal accelerating field, the effect in frequency shift and power dissipation on the operating TM_{010} mode due to PC insertion can be estimated using the field distribution computed by Superfish together with the Slater perturbation theorem [3]. Post coupler positions and dimensions are specified in the Superfish input file for DTL multicell design.

Formulas used for frequency and power calculation are [4]:

$$df = \frac{\int_{\Delta V} \mu H^2 - \varepsilon E^2 \ dV}{4U} = \pi R^2 \cdot dr \cdot f \cdot \sum \frac{k_{cyl}\mu H^2 - k_{cyl}\varepsilon E^2}{4U}$$

$$P = \frac{R_s}{2}\int_S H^2 dS = \frac{1}{2}\sqrt{\frac{\mu\omega\rho}{2}}\left[2\pi R \cdot dr \cdot k_{cyl}\left[\sum H^2(z_{PC}, r)\right] + \pi R^2 H^2(z_{PC}, h)\right]$$

where R is the object radius, dr the radial step between 2 SuperFish data, f the cavity frequency, $k_{cyl} = 2$ is the shape factor due to the field distortion close to the PC surface, μ and ε are the material permeability and permittivity, H and E the unperturbed magnetic and electric fields, U the cavity stored energy, R_s the RF surface resistance, ρ the electrical resistivity, h the post coupler length.

The frequency shift calculated as function of PC length for DTL prototype is shown in Figure 4.2, together with measurements on the DTL hot prototype equipped with 4 PCs. The strong variations in frequency shift measured at certain PC lengths [5] have been investigated with more accurate measurements (Figure 4.3), indicating that the crossing and local coupling of the 3 highest modes of the PC band with the TM_{010}. The Slater perturbation theorem describes the TM_{010} frequency shift due to the PC insertion, but cannot give information on the coupling between the TM_{01} band and the PC band and consequently on the optimum length of the PCs for the tank stabilization.

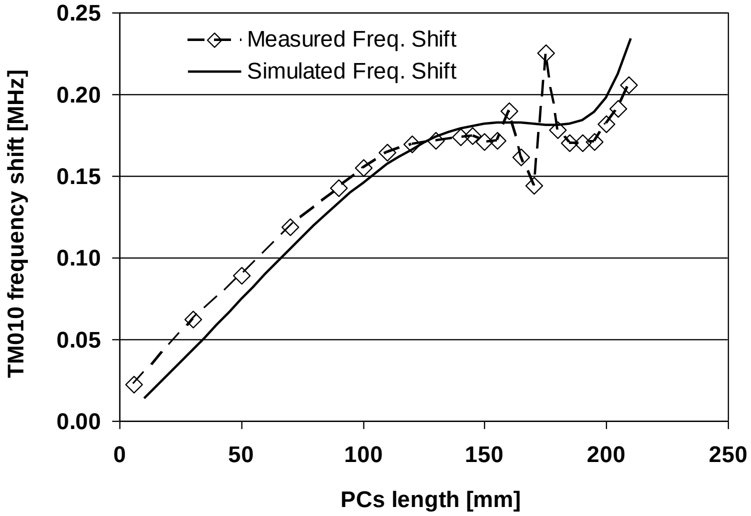

Figure 4.2: Simulated (Superfish) and measured TM_{010} detuning as a function of PC length.

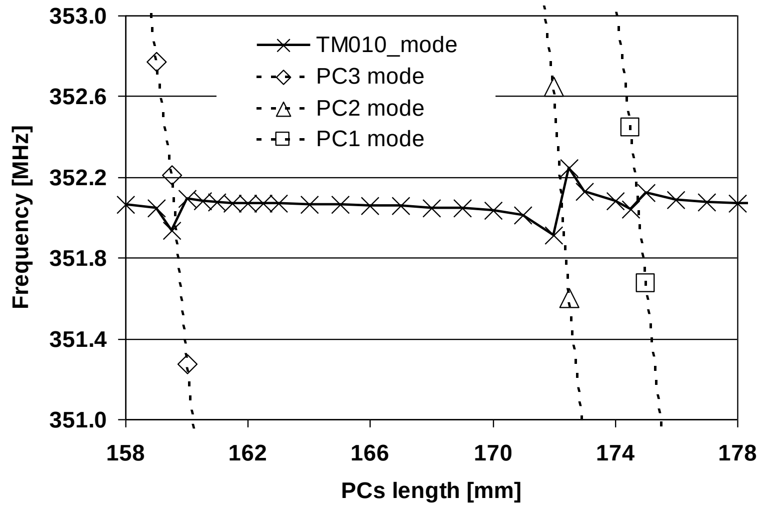

Figure 4.3: Measurements showing PC modes crossing TM_{010} mode.

4.2 3D simulations and bead-pull measurements on post coupler modes

3D HFSS [6] simulations and bead-pull measurements have been undertaken on the four PC modes of the DTL hot prototype. PC modes can be recognized in simulations due to a characteristic field pattern with electric field between PCs and drift tubes and magnetic field around PCs (Figure 4.4). The simulated axial field corresponds well with the bead-pull measurements performed on the PC modes close to confluence. Figure 4.5 shows the highest PC mode (PC_1 mode), which presents the same axial field pattern as the TM_{011} mode shown in Figure 4.6.

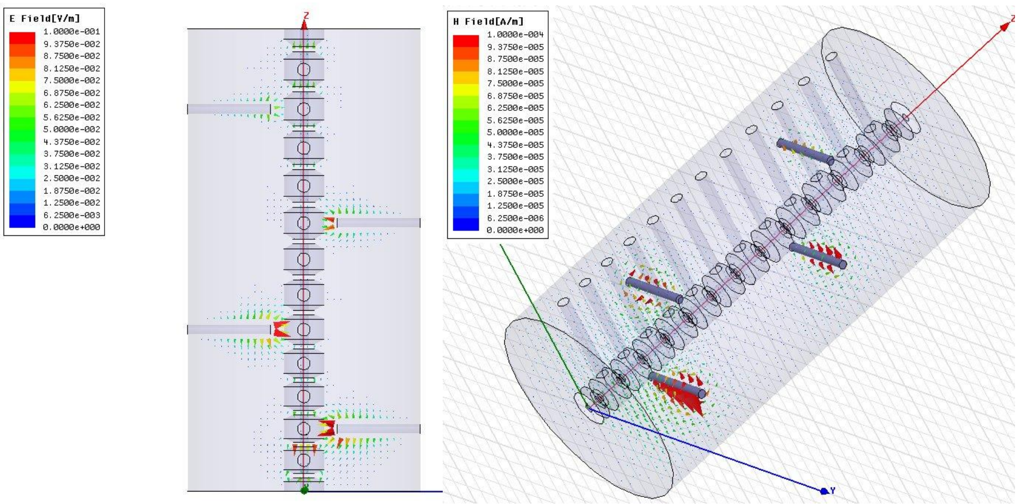

Figure 4.4: Electric and Magnetic Field of the higher PC mode (PC_1 mode) in the DTL hot prototype.

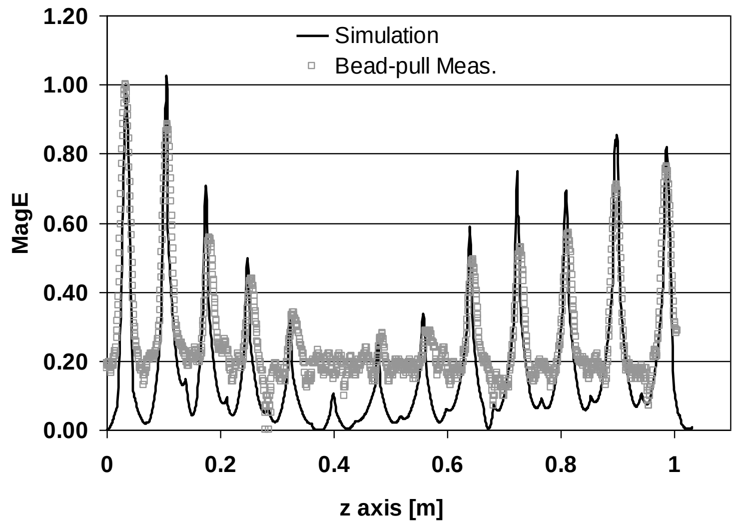

Figure 4.5: Simulated and measured field on axis for the highest PC mode (PC_1 mode) in the DTL hot prototype.

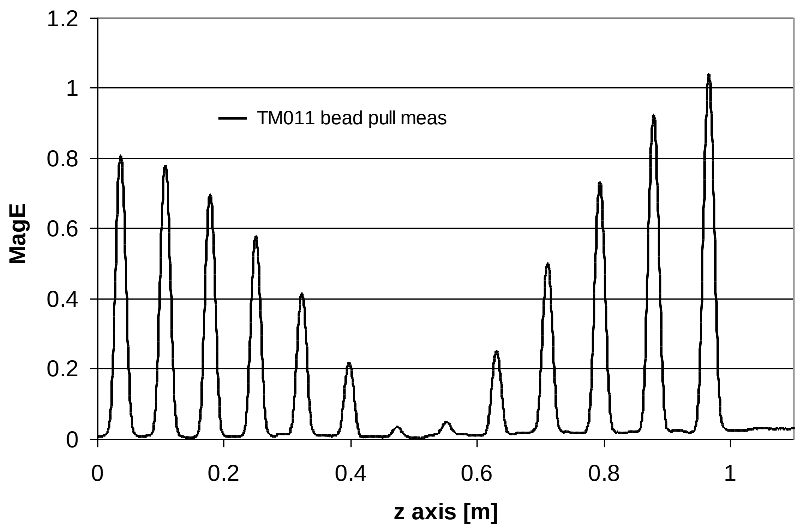

Figure 4.6: Field measurement for TM_{011} mode in the DTL hot prototype.

This suggests an interpretation of the stabilizing effect of the PC_1 mode with respect to perturbations induced by the TM_{011} mode on the accelerating field.

Using the Perturbation Theory formalism limited to PC_1 and TM_{011} modes, the electric field in a generic point (x,y,z) inside the cavity is given by

$$\overline{E}^{pert}(x,y,z) = \overline{E}^{0}(x,y,z) + \Delta\overline{E}^{0}(x,y,z) = \overline{E}^{0}(x,y,z) + \alpha_{PC1}\overline{E}^{PC1}(x,y,z) + \alpha_{TM011}\overline{E}^{TM011}(x,y,z)$$

The quantity measured with the bead-pull technique is the electric field magnitude on the beam axis:

$$\left|\overline{E}\right|^{pert}(0,0,z)=\left|\overline{E}\right|^{0}(0,0,z)+\left|\Delta\overline{E}\right|^{0}(0,0,z)=\left|\overline{E}\right|^{0}(0,0,z)+\alpha_{PC1}\left|\overline{E}\right|^{PC1}(0,0,z)+\alpha_{TM011}\left|\overline{E}\right|^{TM011}(0,0,z)$$

with $\alpha_{mode} \equiv \dfrac{\left\langle \overline{E}^{mode}\left|\overline{\overline{P}}\right|\overline{E}_0\right\rangle}{\omega_o^2-\omega_{mode}^2} = \dfrac{\iiint_{cavity}\left[\sum_i E_i^{mode}(x,y,z)\sum_j P_{i,j}(x,y,z)E_j^0(x,y,z)\right]dxdydz}{\omega_o^2-\omega_{mode}^2}$.

The perturbation coefficients α_{PC1} and α_{TM011} depend on the local geometry perturbation described by the matrix $\overline{\overline{P}}=\overline{\overline{P}}(x,y,z)$ and on the field pattern of modes. If mode resonant frequencies ω_{PC1} and ω_{TM011} are tuned in such a way that coefficients α_{PC1} and α_{TM011} are equal and opposite, the accelerating field perturbation can be canceled.

4.3 3D simulation study of post coupler geometrical parameters

3D HFSS simulations have been used in order to obtain values of the PC_1 mode frequency as function of the number of PC per unit length of the tank (Figure 4.7). Taking a very small gap between PC and DT (gap PC-DT << λ/4) the PC mode electric field is concentrated in the gap area, so it is possible to apply the quasi-static approximation [7] in order to calculate values of the capacitance C_p associated to the gap PC-DT using the formula $C_p=\dfrac{2U}{V^2}$, where U and V are calculated from the simulation. For a gap PC-DT = 3 mm, the results show a value of C_p distributed with respect to an average value of $\overline{C_p}=(2.8\pm0.2)pF$, while the frequency increase with the number of PCs per unit length (Figure 4.8).

From this we can conclude that, for small variations of the distance between PC and DT, the inductance L_p associated to the PC is a function of the distance between PCs. Figure 4.9 shows the values calculated from simulations as $L_p=\dfrac{1}{(2\pi f_p)^2\overline{C_p}}$ compared with the curve obtained by the formula $L_p=2\cdot10^{-7}\ln\left(\dfrac{D_{eq}}{d_{PC}}\right)\cdot l_{PC}$ of a coaxial inductor where the PC is the inner conductor and the outer conductor has an equivalent diameter of

$D_{eq} = D_{tank}\sqrt{\frac{L_{tank}}{2 \cdot N^{o}_{PCs} \cdot l_{PC}}}$ where L_{tank} and D_{tank} are the tank length and diameter, l_{pc} is the PC length and $N°_{PCs}$ is the number of PCs inside the tank.

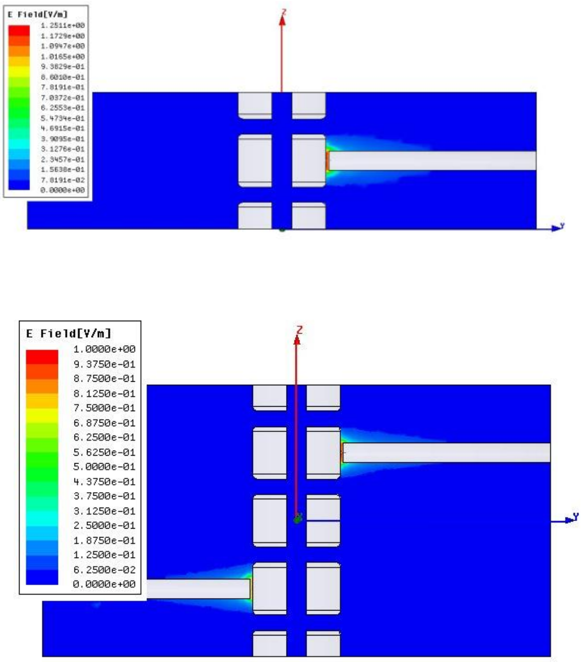

Figure 4.7: two cavity configurations equivalent on number of PCs per unit length.

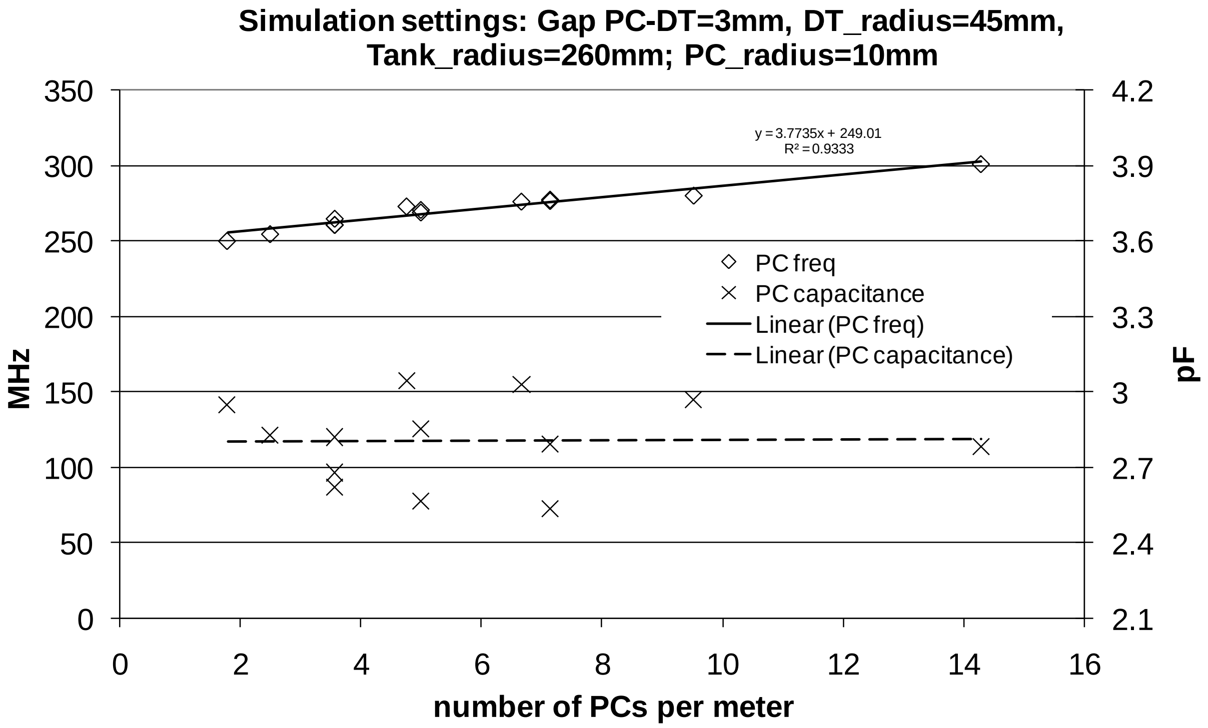

Figure 4.8: PC mode frequency and Cp capacitance from 3D simulations of different distributions of PCs inside the tank.

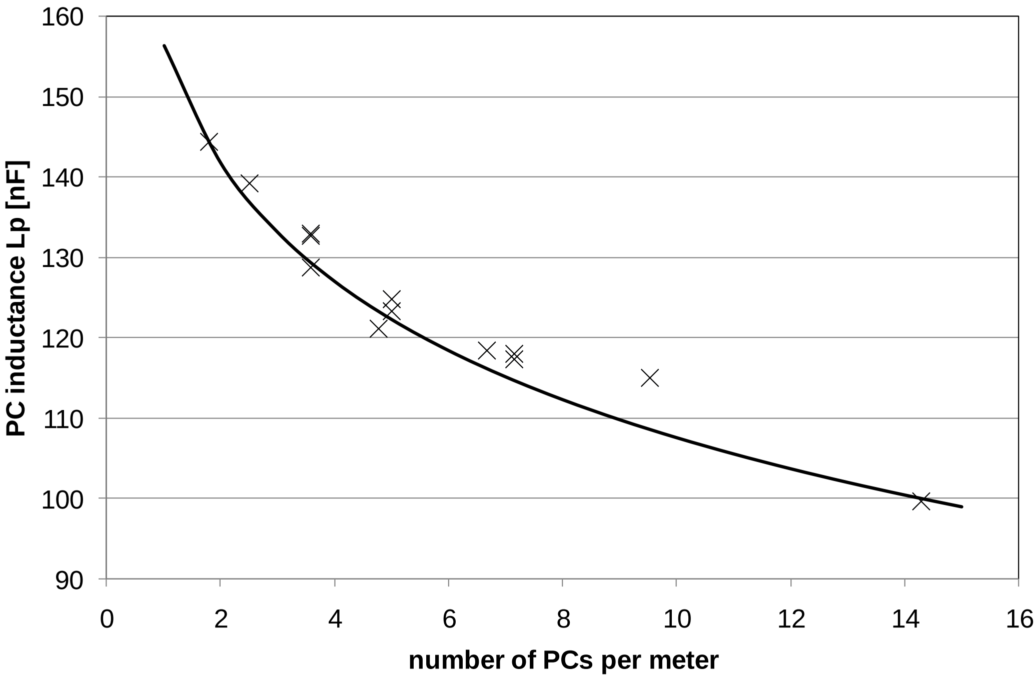

Figure 4.9: PC inductance L_p as function of the number of PCs per meter. The solid line is given by the L_p formula, crosses are obtained from 3D simulations in quasi-static approximation.

In quasi-static conditions it is possible to estimate the C_p value starting form electrostatic considerations. The electrostatic definition for the capacitance is $C = \frac{Q}{V} = \frac{\varepsilon_0 \oint_A \sigma \cdot dA}{\int_d \bar{E} \cdot d\bar{s}} = \frac{\varepsilon_0 \oint_A \bar{E} \cdot d\bar{A}}{\int_d \bar{E} \cdot d\bar{s}}$. We want to get a simple empirical formula $C_p = \frac{\varepsilon_0 A_Q}{g_{av}}$,

where A_Q is the area where the surface charge density σ induced by the electric field is distributed, and g_{av} is the average integral path of the electric field. Figure 4.10 shows in detail the electric field distribution between PC and DT in a PC mode. The surface charge on the DT is distributed over an ellipsis of area $A_Q = (\pi \cdot x_{tg} \cdot s_{tg})$ and the average distance from the PC is $g_{av} = ½ (d_{DT} + 2g - y_{tg})$, where $P_{tg} = (x_{tg}, y_{tg})$ is the tangent point to the drift tube cylinder of a line starting from the border tip point of the PC, s_{tg} is the arc length from P_{tg} to the top of the drift tube, d_{DT} is the DT diameter and g is the gap PC-DT. The capacitance is independent from the length of the DT and the formula is:

$$C_p = \varepsilon_0 \frac{A_Q}{g_{av}} = \varepsilon_0 \frac{\pi \cdot x_{tg} \cdot d_{DT} \arccos(2y_{tg} / d_{DT})}{\frac{d_{DT}}{2} + 2g - y_{tg}}$$

Figure 4.11 shows the curve given by the formula with the values calculated from simulations as $C_p = \frac{2U}{V^2}$. The equation overestimates the capacitance by about 10% with respect to the simulation results.

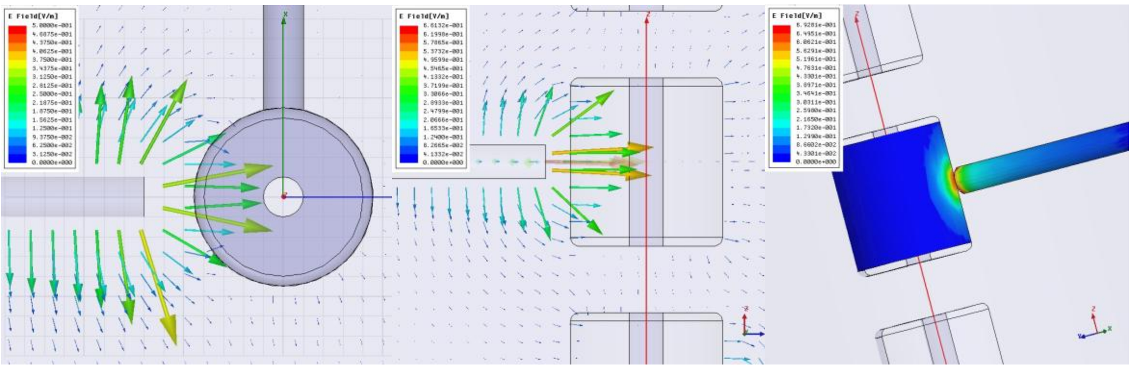

Figure 4.10: electric field pattern between PC and DT in a PC mode.

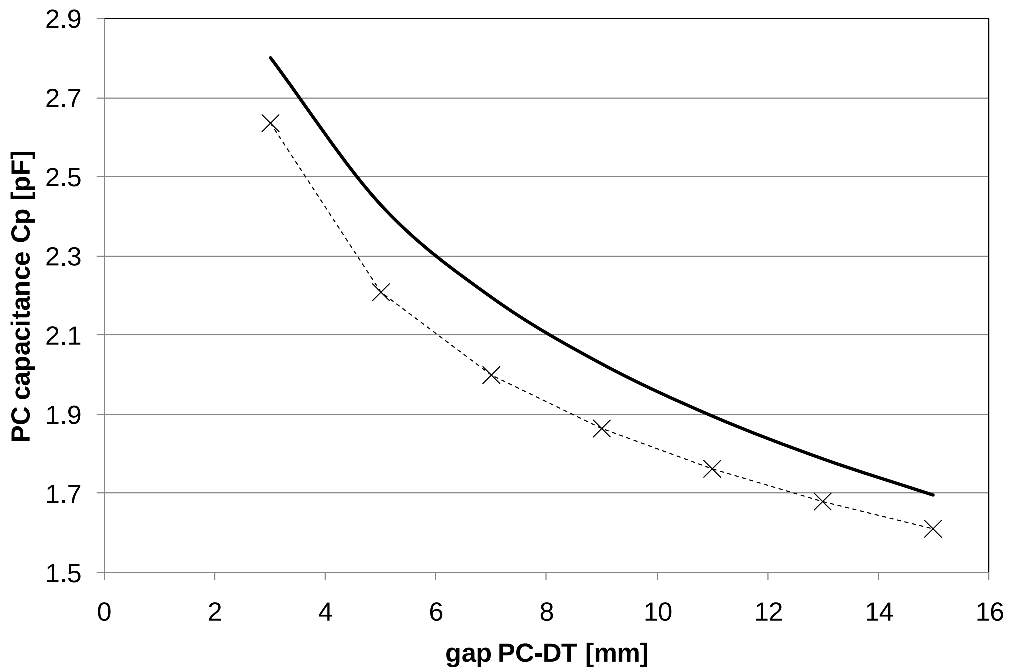

Figure 4.11: PC capacitance C_p as function of the gap PC-DT. The solid line is given by the C_p formula, crosses are obtained from 3D simulations in quasi-static approximation.

The interaction of PCs and stems has also been studied with 3D simulations, in order to properly insert stems in the DTL equivalent circuit.

Stem modes can be distinguished in RF measurements because of the much lower frequencies with respect to the operating mode and because of the low sensitivity to gap displacements. 3D simulations show that the presence of DT stems weakly affects the field pattern of the PC modes (Figure 4.12): the electromagnetic energy is concentrated around the PCs, with a slight deviation of the H field around the stems, and the change in mode frequency can be estimated using the Slater perturbation theorem. The same behavior can be noticed for the stem modes in relation to the presence of PCs (Figure 4.13).

From this we conclude that DT stems and PCs can be considered separately in the equivalent circuit.

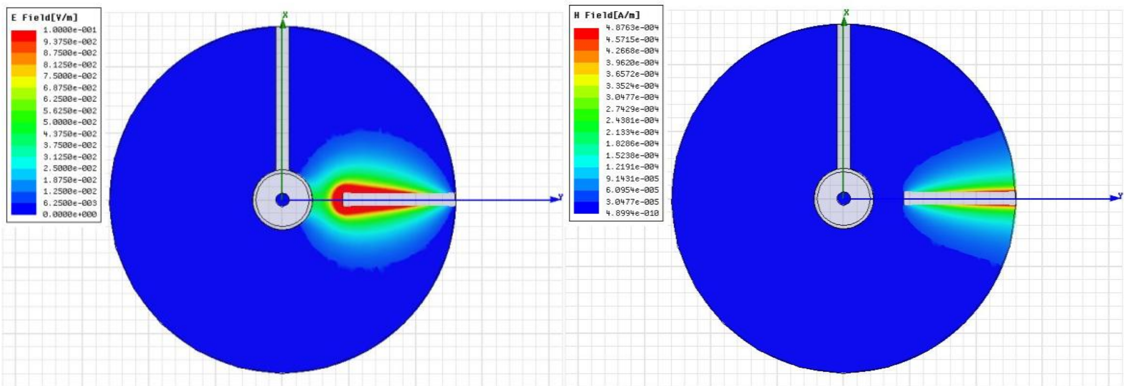

Figure 4.12: E and H field magnitude of the PC1 mode showing poor influence of DT stems on mode pattern.

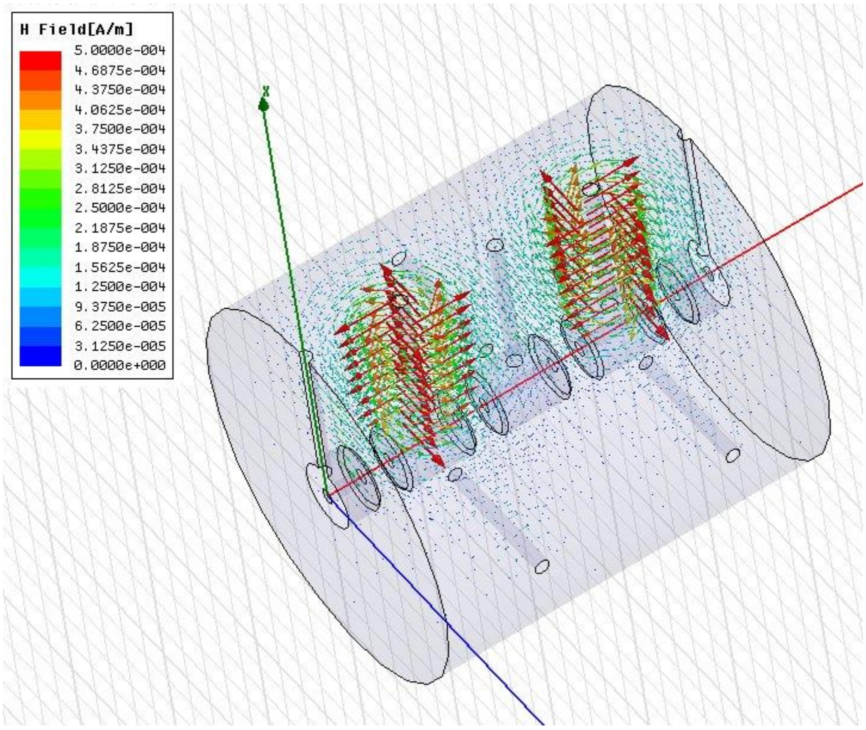

Figure 4.13: a 3D view of stem mode magnetic field, showing weak coupling between stems and PCs.

References

[1] S. Ramberger et al., “Drift Tube Linac Design and Prototyping for the CERN Linac4”, Proc. LINAC08.

[2] N. Alharbi, F. Gerigk and M. Vretenar, “Field Stabilization with Post Couplers for DTL Tank1 of Linac4”, Tech. Rep. CARE-Note-2006-012-HIPPI, CARE, 2006.

[3] Los Alamos Accelerator Code Group, Poisson Superfish.

[4] Los Alamos Accelerator Code Group, Poisson Superfish User’s Manual.

[5] S. Machida, T. Kato, S. Fukumoto, “Stabilizing characteristics of post-couplers”, Transaction on Nuclear Science, 1985, Vol. 32.

[6] Ansoft Corporation, HFSS 10.1.

[7] T. Wangler, “RF Linear Accelerators”, John Wiley & Sons, Inc. 1998, par.5.14.

Chapter 5. Post couplers: equivalent circuit

With the objective of better understanding the post coupler (PC) stabilization mechanism and in order to define a tuning strategy for longer DTL cavities, an equivalent circuit model was developed and it is presented in this chapter. Principal ingredients for a representative circuit are its equivalent circuit elements including their interdependence expressed by connections and mutual inductances.

5.1 Circuit equations and matrix form

A complete equivalent circuit for a DTL cell equipped with PCs is shown in Figure 5.1. In this circuit C_0 represents the gap capacitance, $L_0/2$ represents the inductance of half dirft tube (DT), C is the capacitance of a DT to the tank wall, represented by the ground conductor. Stems are represented by inductors L_s in parallel with the shunt capacitance C_s. C_p is the capacitance between PC and DT and L_p the inductance of a PC.

C_0 can be estimated with the parallel plate capacitance formula, L_0 and C_s with coaxial inductance and capacitance formulas and L_s with straight wire inductance formula [1]. C_p and L_p estimation formulas are described in Chapter 4. Geometrical formulas, DTL hot prototype dimensions and circuit element values calculated are listed in Table 5.1 and obtained frequency values are compared measured frequencies. These approximations are obtained by electrostatic arguments, but they can give an idea of the orders of magnitude of the circuit elements.

There are 3 main resonator chains in a DTL: drift tube resonators, stem resonators and PC resonators. The TM_{010} mode frequency is given by $\omega_0 = 1/\sqrt{C_0 L_0}$ and we define a PC frequency $\omega_p = 1/\sqrt{C_p L_p}$ and a stem frequency $\omega_s = 1/\sqrt{C_s L_s}$. Frequency values estimated from geometrical parameters give ω_s (≈ 200 MHz) lower than ω_0 and ω_p (≈ 350 - 370 MHz). This is confirmed by measurements on the DTL prototype, where the stem dispersion curve is lower than TM and PC dispersion curves (Figure 5.2). Since for frequencies close to the operating mode the stem impedance $Y_{stem} = j\omega C_s\left(1-\frac{\omega_s^2}{\omega^2}\right)$ is capacitive and there is not coupling between stem and PC, as discussed in Chapter 4, the circuit model is simplified to the circuit in Figure 5.3, where the capacitance C is defined $C = C_s\left(1 - \frac{\omega_s^2}{\omega^2}\right)$.

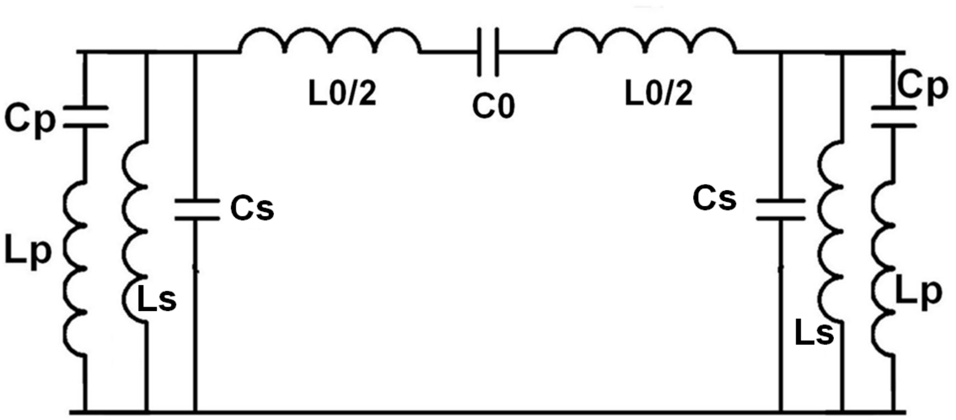

Figure 5.1: equivalent circuit for a DTL including DT, stem and PC resonators.

Formula	Geom. Parameters	Calc. Values	Frequency [MHz]
$C_0 = \varepsilon_0 \frac{\pi \cdot d_{DT}^2}{4 \cdot gap}$	d_{DT}=9 cm, gap=1.5 cm	3.76 pF	370
$L_0 = 2 \cdot 10^{-7} \ln\left(\frac{D_{tank}}{d_{DT}}\right)\beta\lambda$	D_{tank}=52 cm, d_{DT}=9 cm, $\beta\lambda$=14 cm	49 nH	
$C_s = \varepsilon_0 \frac{2\pi}{\ln\left(\frac{D_{tank}}{d_{DT}}\right)}\beta\lambda$	D_{tank}=52 cm, d_{DT}=9 cm, $\beta\lambda$=14 cm	4.44 pF	200
$L_s = 2 \cdot 10^{-7} \cdot l_{st}\left(2.303\log\left(\frac{4l_{st}}{d_{st}}\right)\right)$	L_{st}=21.5 cm, D_{st}=2.9 cm	146 nH	
$C_p = \varepsilon_0 \frac{A_Q}{g_{av}}$	d_{pc}=2 cm, gap_{pc}=10 mm	1.96 pF	330
$L_p = 2 \cdot 10^{-7} l_{pc} \ln\left(\frac{D_{eq}}{d_{pc}}\right)$	l_{pc}=20.5 cm, L_{tank}=56 cm, N_{PCs}=3	117 nH	

Table 5.1: formulas, geometric dimensions and circuit element values for DTL prototype geometry.

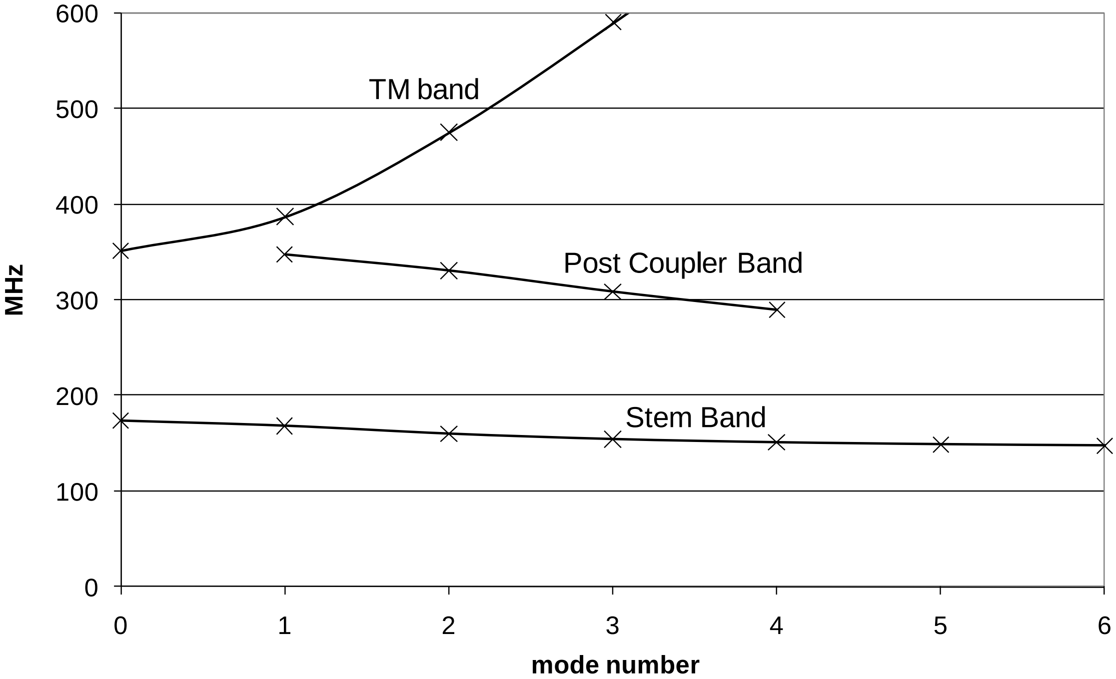

Figure 5.2: frequency bands in the DTL prototype.

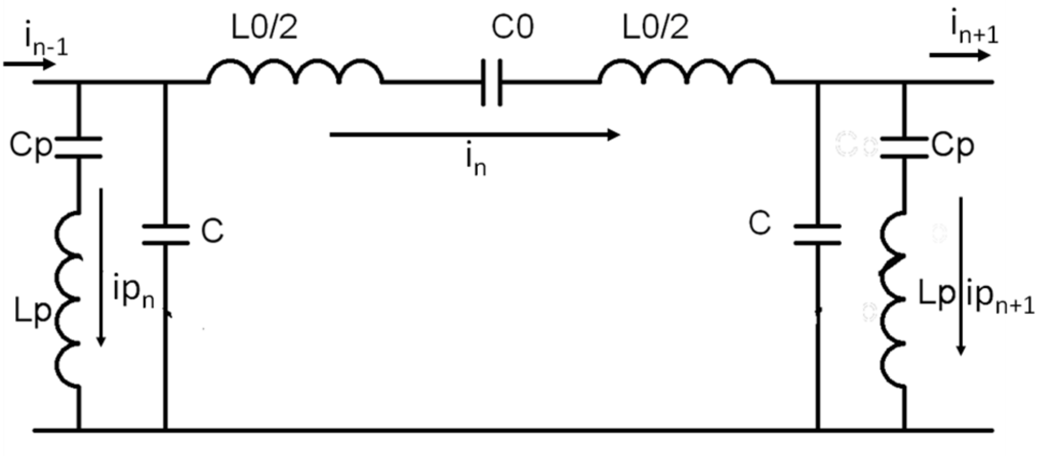

Figure 5.3: Equivalent Circuit for a DTL equipped with PCs.

Solving the mesh equations for the drift tube and the PC currents, we obtain the system

$$\begin{cases} ip_n\left(j\omega L_p + \dfrac{1}{j\omega C_p}\right) - \ i_{n-1} - i_n - ip_n \ \ \dfrac{1}{j\omega C} = 0 \\ i_n\left(j\omega L_0 + \dfrac{1}{j\omega C_0}\right) + \ 2i_n - i_{n-1} - i_{n+1} + ip_n - ip_{n+1} \ \ \dfrac{1}{j\omega C} = 0 \\ ip_{n+1}\left(j\omega L_p + \dfrac{1}{j\omega C_p}\right) - \ i_n - i_{n+1} - ip_{n+1} \ \ \dfrac{1}{j\omega C} = 0 \end{cases}$$

This system is equivalent to the following, with some substitutions and simplifications:

$$\begin{cases} -\dfrac{i_{n-1}}{C}+ip_n\left(\dfrac{1}{C}+\dfrac{1}{C_p}\right)+\dfrac{i_n}{C}=\omega^2\dfrac{ip_n}{C_p\omega_p^2} \\ -\dfrac{i_{n-1}}{C}+\dfrac{ip_n}{C}+i_n\cdot\left(\dfrac{2}{C}+\dfrac{1}{C_0}\right)-\dfrac{ip_{n+1}}{C}-\dfrac{i_{n+1}}{C}=\omega^2\dfrac{i_n}{C_0\omega_0^2} \\ -\dfrac{i_n}{C}+ip_{n+1}\left(\dfrac{1}{C}+\dfrac{1}{C_p}\right)+\dfrac{i_{n+1}}{C}=\omega^2\dfrac{ip_{n+1}}{C_p\omega_p^2} \end{cases}$$

This system of equations can be put into a matrix form $\overline{\overline{M}}\cdot\vec{I}=\omega^2\vec{I}$, to be solved as an eigenvalue problem. For a cavity of 3 cells + 2 PCs the 5 x 5 matrix is:

$$\begin{bmatrix} C_0\omega_0^2\left(\dfrac{1}{C}+\dfrac{1}{C_0}\right) & -\dfrac{C_p\omega_p^2}{C} & -\dfrac{C_0\omega_0^2}{C} & 0 & 0 \\ -\dfrac{C_0\omega_0^2}{C} & C_p\omega_p^2\left(\dfrac{1}{C}+\dfrac{1}{C_p}\right) & \dfrac{C_0\omega_0^2}{C} & 0 & 0 \\ -\dfrac{C_0\omega_0^2}{C} & \dfrac{C_p\omega_p^2}{C} & C_0\omega_0^2\left(\dfrac{2}{C}+\dfrac{1}{C_0}\right) & -\dfrac{C_p\omega_p^2}{C} & -\dfrac{C_0\omega_0^2}{C} \\ 0 & 0 & -\dfrac{C_0\omega_0^2}{C} & C_p\omega_p^2\left(\dfrac{1}{C}+\dfrac{1}{C_p}\right) & \dfrac{C_0\omega_0^2}{C} \\ 0 & 0 & -\dfrac{C_0\omega_0^2}{C} & \dfrac{C_p\omega_p^2}{C} & C_0\omega_0^2\left(\dfrac{1}{C}+\dfrac{1}{C_0}\right) \end{bmatrix}\cdot\begin{bmatrix} \dfrac{i_0}{C_0\omega_0^2} \\ \dfrac{ip_1}{C_P\omega_P^2} \\ \dfrac{i_1}{C_0\omega_0^2} \\ \dfrac{ip_2}{C_P\omega_P^2} \\ \dfrac{i_2}{C_0\omega_0^2} \end{bmatrix}=\omega^2\begin{bmatrix} \dfrac{i_0}{C_0\omega_0^2} \\ \dfrac{ip_1}{C_P\omega_P^2} \\ \dfrac{i_1}{C_0\omega_0^2} \\ \dfrac{ip_2}{C_P\omega_P^2} \\ \dfrac{i_2}{C_0\omega_0^2} \end{bmatrix}$$

Eigenvectors are currents scaled with capacitances and element frequencies squared. Eigenvalues are mode frequencies squared.

The voltage through a gap is proportional to the current divided by the capacitance C_0 of the gap $V_{0,i}=I_{0,i}/C_{0,i}$, and the average field E_0 is defined by voltage divided by cell length $E_{0,i}=V_{0,i}/Lcell_i$. In case of all identical cells currents, voltages and fields are equivalent, but is important to consider different definitions in case of increasing gap lengths or gap perturbations.

5.2 Circuit derivation of the stabilizing post couplers condition

This circuit gives a first idea of the PCs stabilization mechanism.

Let us use a transport matrix notation for voltages V_n and currents I_n along the circuit chain [2]:

$$\begin{bmatrix} V_{n+1} \\ I_{n+1} \end{bmatrix} = \begin{bmatrix} 1 & -Z_n \\ -Y_n & 1+Y_n Z_n \end{bmatrix} \begin{bmatrix} V_n \\ I_n \end{bmatrix}$$

where $Z_n = \dfrac{1}{j\omega C_0}\left(1-\dfrac{\omega^2}{\omega_0^2}\right)$ and $Y_n = j\omega\left(C + C_p \dfrac{\omega_p^2}{\omega_p^2-\omega^2}\right)$.

The DTL tank is close with metallic end plates. In the equivalent circuit this condition is represented by a short circuit at both ends of the circuit chain (Figure 5.4). Then boundary conditions are $V_0 = 0$ and $V_{end} = 0$.

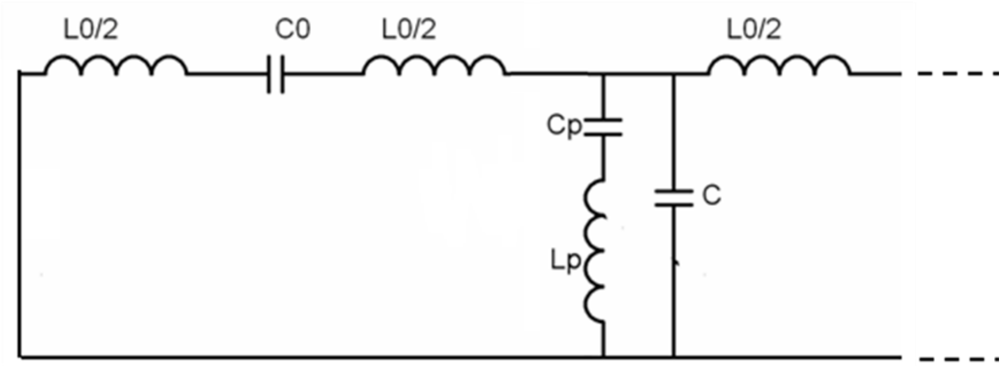

Figure 5.4: DTL end plates are represented by short circuit boundary conditions in the equivalent circuit.

If the 1st cell capacitance has a perturbation dC_0, and there are no PCs, the field flatness of the whole structure is perturbed (the quantity proportional to the gap field is the current)

$$\begin{bmatrix} V_1 \\ I_1 \end{bmatrix} = \begin{bmatrix} -Z_0 I_0 \\ (1+Z_0 Y_0) I_0 \end{bmatrix} = \begin{bmatrix} -\dfrac{1}{j\omega C_0}\left(d-\dfrac{\omega^2}{\omega_0^2}\right) I_0 \\ \left(1+\dfrac{j\omega C}{j\omega C_0}\left(d-\dfrac{\omega^2}{\omega_0^2}\right)\right) I_0 \end{bmatrix} = \begin{bmatrix} -\dfrac{1}{j\omega C_0}(d-1) I_0 \\ \left(1+\dfrac{C}{C_0}(d-1)\right) I_0 \end{bmatrix}$$

where $d = \dfrac{C_0}{C_0 + dC_0}$ and the driving frequency is $\omega = \omega_0$. For the next unperturbed cells the impedance $Z_n = 0$, and we obtain:

$$I_2 = -Y_1 V_1 + (1+Y_1 Z_1) I_1 = Y_1 Z_0 I_0 + I_1 = I_1 + \frac{C}{C_0}(d-1) I_0 .$$

The difference $\left|I_n - I_{n-1}\right| = \left|\dfrac{C}{C_0}(d-1) I_0\right|$ is constant along the cell gaps (Figure 5.5).

Moreover, if the cell length scales with βλ, the perturbation effect at other cells becomes stronger where the ratio C/C_0 is larger. The effect is therefore stronger towards higher beam energies in the DTL!

Let us now suppose to have one PC every other cell (Figure 5.5).

$$I_2 = I_1 + \left[\frac{C}{C_0}(d-1) + \frac{C_p}{C_0}(d-1)\left(\frac{\omega_p^2}{\omega_p^2 - \omega_0^2} \right) \right] I_0 .$$

The formula shows that the presence of the PCs can modify the propagation of the perturbation from one cell to the next one.

The PCs stabilize if $I_2 = I_0$:

$$I_2 \equiv \left(1 + \frac{C}{C_0}(d-1) \right) I_0 + \left[\frac{C}{C_0}(d-1) + \frac{C_p}{C_0}(d-1)\left(\frac{\omega_p^2}{\omega_p^2 - \omega_0^2} \right) \right] I_0 = I_0$$

and from this equation a condition for the optimum value of the PC frequency is obtained:

$$\omega_p^2 = \frac{2C\omega_0^2}{2C + C_p} .$$

If we assume that, when changing the PC - DT gap, the variation of Lp is negligible with respect to the variation of C_p, it is useful to solve the previous relation for C_p:

$$C_p^{stab} = \frac{2C}{2CL_p\omega_0^2 - 1} .$$

In general the conditions are $\omega_p^2 = \dfrac{\omega_0^2}{1 + \dfrac{n \cdot C_p}{C}}$ and $C_p^{stab} = \dfrac{C}{CL_p\omega_0^2 - n}$ where $n = \dfrac{number - post - couplers}{number - cells}$. Let us define the coupling coefficient $k_p = \dfrac{C_p}{C}$ and the previous relation becomes $\omega_p^2 = \dfrac{\omega_0^2}{1 + n \cdot k_p}$ where both ω_p and k_p depend on C_p.

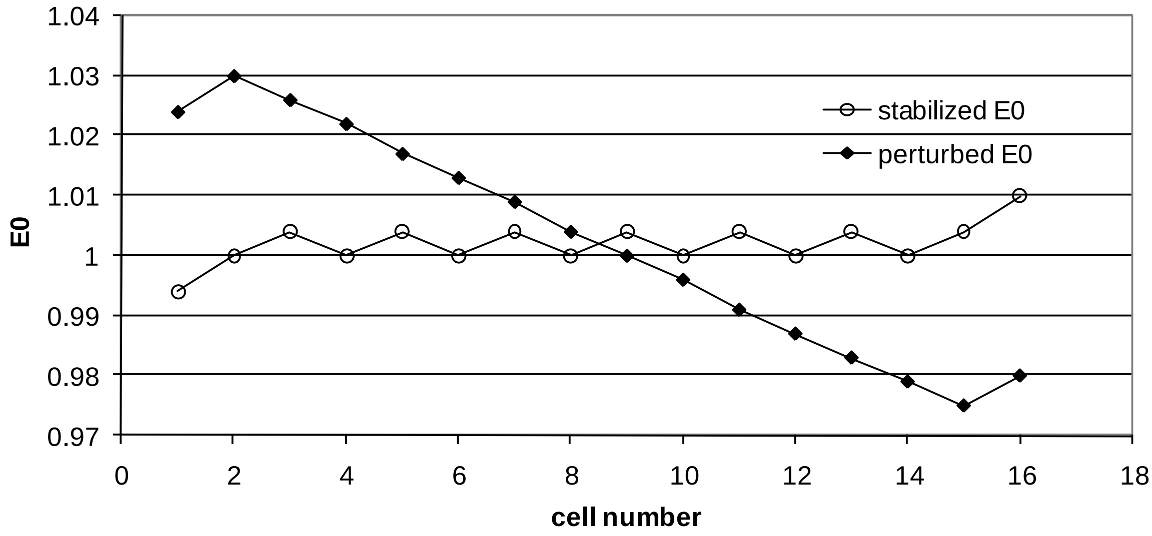

Figure 5.5: perturbed E_0 without PCs and with PCs at stabilizing value of C_p from a circuit simulation.

The optimum value of C_p for stabilization decreases as function of the capacitance C (Figure 5.6). Where DTs are longer, gap PC-DT must be larger; where DTs are shorter, gap PC-DT must be smaller.

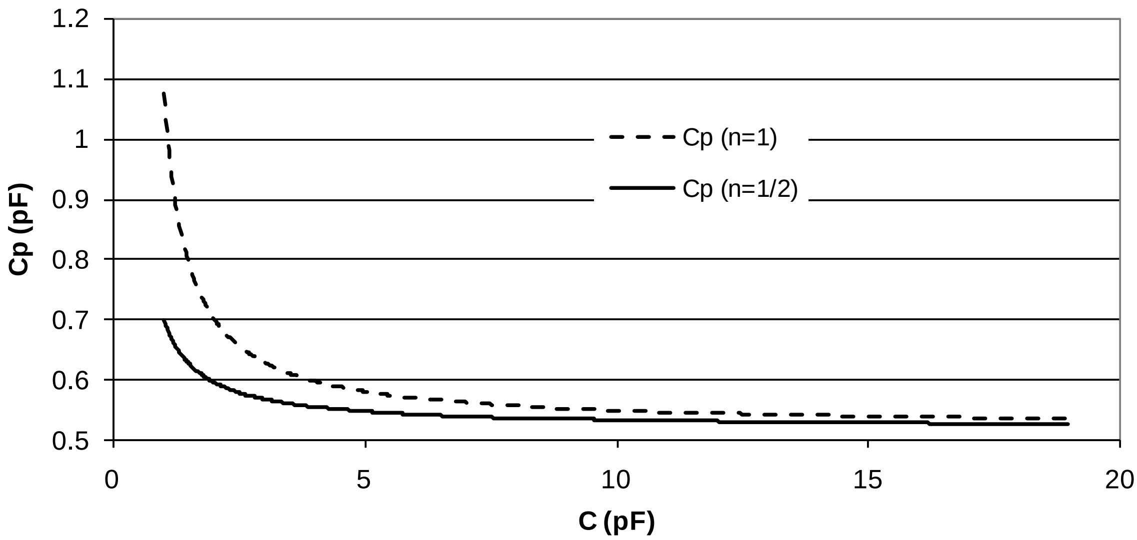

Figure 5.6: C_p as function of C (case of n=1 and n=1/2).

Some observations can be made about the distance between PC and DT in order to understand the stabilizing setting of gap PC-DT (Figure 5.7):

- if the gap is too short ($C_p > C_p^{stab}$), PCs can compensate the perturbation, but not completely;

- if the gap is slightly larger than the stabilizing condition ($C_p < C_p^{stab}$ with $\omega_0 > \omega_p > \omega_p^{stab}$) there is a kind of over-compensation that changes the slope with respect to the perturbation;
- if gap is much larger than the stabilizing condition ($C_p << C_p^{stab}$ and $\omega_p > \omega_0$), the PC effect is de-stabilizing.

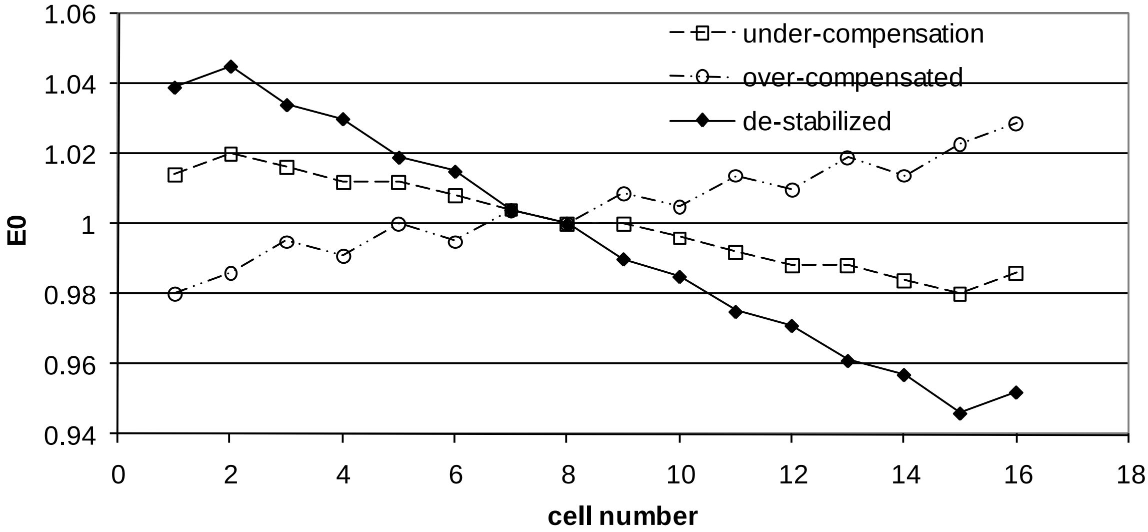

Figure 5.7: the PC effect in a perturbed field with gap PC-DT at 3 different configurations described above.

5.3 1st and 2nd magnetic coupling between post couplers

A comparison of measured PC dispersion curve with curve obtained by the equivalent circuit (Figure 5.10a) shows that one needs to take into account a next nearest coupling between PCs, which couples PCs placed in opposite sides of the DTL tank. This nearest neighbor coupling is equivalent to a magnetic coupling between PC inductors L_p (Figure 5.8) with the coupling factor $k_{p1} = -M_p / L_p \cdot \omega_0^2$ at the operating frequency using self and mutual inductances L_p and M_p.

A next nearest neighbor coupling factor k_{p2} between PCs is included in the matrix as well. It is equivalent to a mutual inductance M_{p2} acting between PCs placed at the same side of the DTL tank. M_{p2} has an opposite sign with respect to M_p.

Figure 5.8 shows the circuit including PC couplings, Figure 5.8 shows the matrix and Figure 5.10a and 5.10b show the dispersion curves obtained taking into account the PC couplings.

The effect of a second magnetic coupling between PCs has been clearly observed in 3D HFSS simulations. A structure with of 4 cells of 7 cm length each, equipped with 3 PCs, shows that the 2nd PC-mode, characterized by the un-excited central PC (Figure 5.11), is higher in frequency respect to the 1st PC-mode, which is usually the highest in frequency. This effect is caused by the stronger negative coupling and it becomes less important with 10 cm long cells. Finally, with 14 cm long cells, the 2nd PC-mode frequency is lower than the 1st mode.

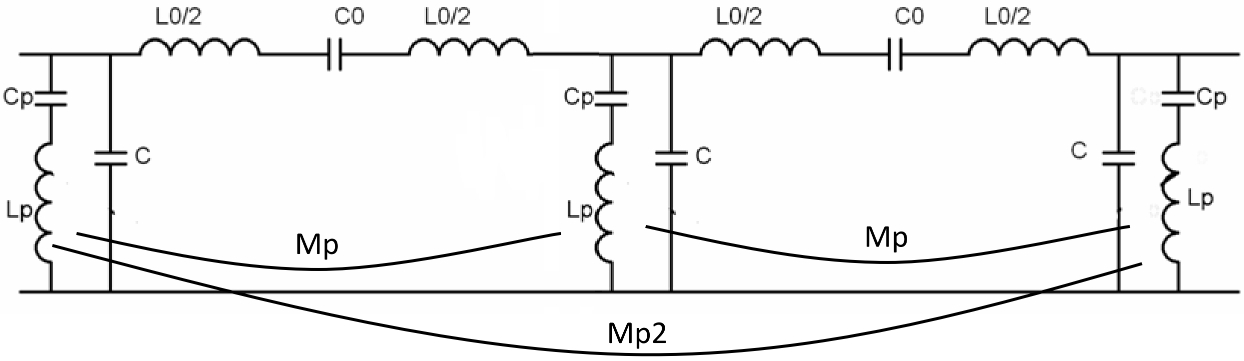

Figure 5.8: equivalent circuit including nearest and next nearest coupling between PCs.

$$\begin{bmatrix}
C_0\omega_0^2\left(\frac{1}{C}+\frac{1}{C_0}\right) & -\frac{C_p\omega_p^2}{C} & -\frac{C_0\omega_0^2}{C} & 0 & 0 & 0 & 0 \\
-\frac{C_0\omega_0^2}{C} & C_p\omega_p^2\left(\frac{1}{C}+\frac{1}{C_p}\right) & \frac{C_0\omega_0^2}{C} & k_{p1} & 0 & k_{p2} & 0 \\
-\frac{C_0\omega_0^2}{C} & \frac{C_p\omega_p^2}{C} & C_0\omega_0^2\left(\frac{2}{C}+\frac{1}{C_0}\right) & -\frac{C_p\omega_p^2}{C} & -\frac{C_0\omega_0^2}{C} & 0 & 0 \\
0 & k_{p1} & -\frac{C_0\omega_0^2}{C} & C_p\omega_p^2\left(\frac{1}{C}+\frac{1}{C_p}\right) & \frac{C_0\omega_0^2}{C} & k_{p1} & 0 \\
0 & 0 & -\frac{C_0\omega_0^2}{C} & -\frac{C_p\omega_p^2}{C} & C_0\omega_0^2\left(\frac{2}{C}+\frac{1}{C_0}\right) & -\frac{C_p\omega_p^2}{C} & -\frac{C_0\omega_0^2}{C} \\
0 & k_{p2} & 0 & k_{p1} & -\frac{C_0\omega_0^2}{C} & C_p\omega_p^2\left(\frac{1}{C}+\frac{1}{C_p}\right) & \frac{C_0\omega_0^2}{C} \\
0 & 0 & 0 & 0 & -\frac{C_0\omega_0^2}{C} & \frac{C_p\omega_p^2}{C} & C_0\omega_0^2\left(\frac{1}{C}+\frac{1}{C_0}\right)
\end{bmatrix}$$

Figure 5.9: circuit matrix including nearest and next nearest coupling between PCs.

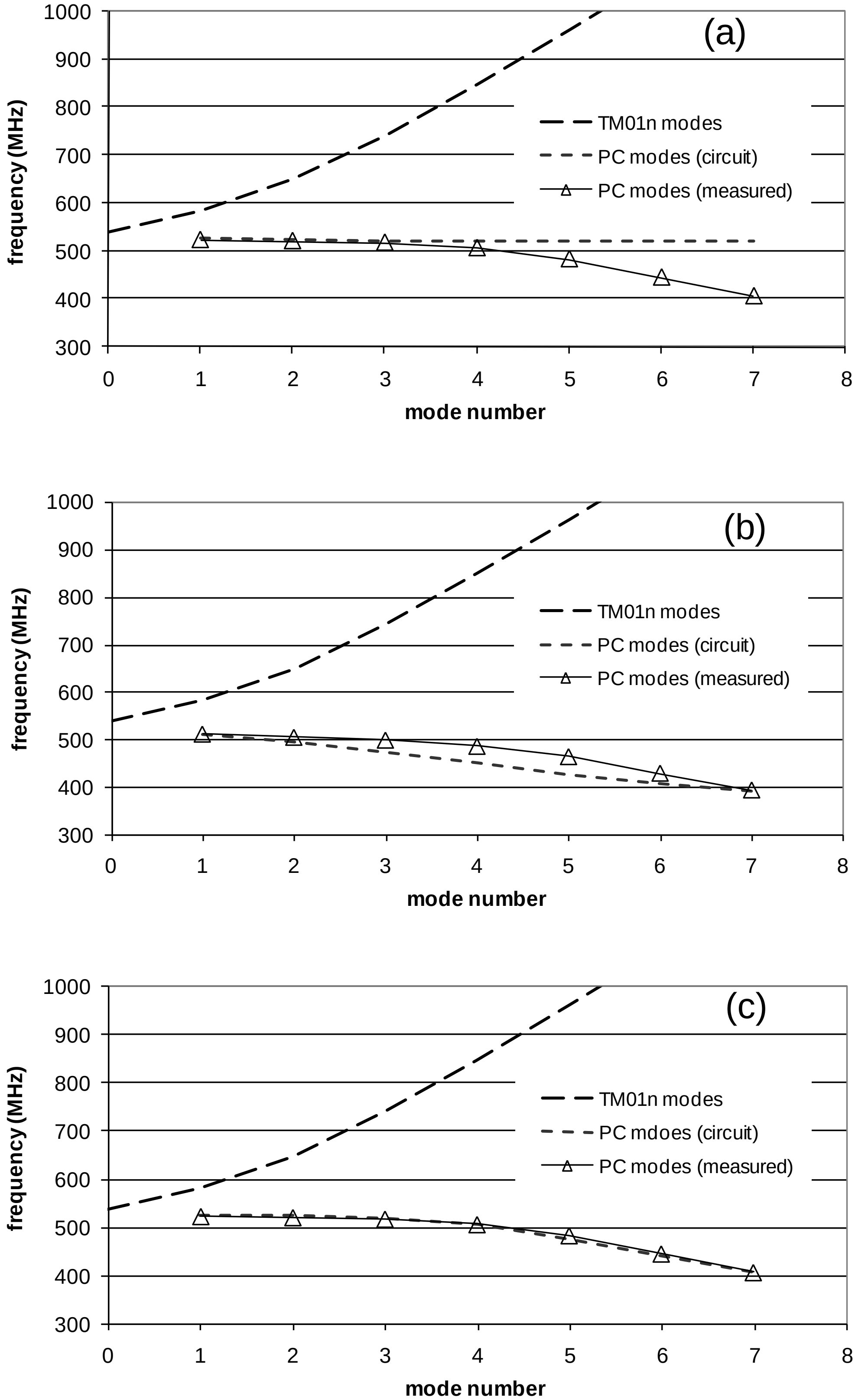

Figure 5.10: PC dispersion curve computed by equivalent circuit without PC coupling (a), with nearest neighbor PC coupling (b) and next nearest neighbor PC coupling (c).

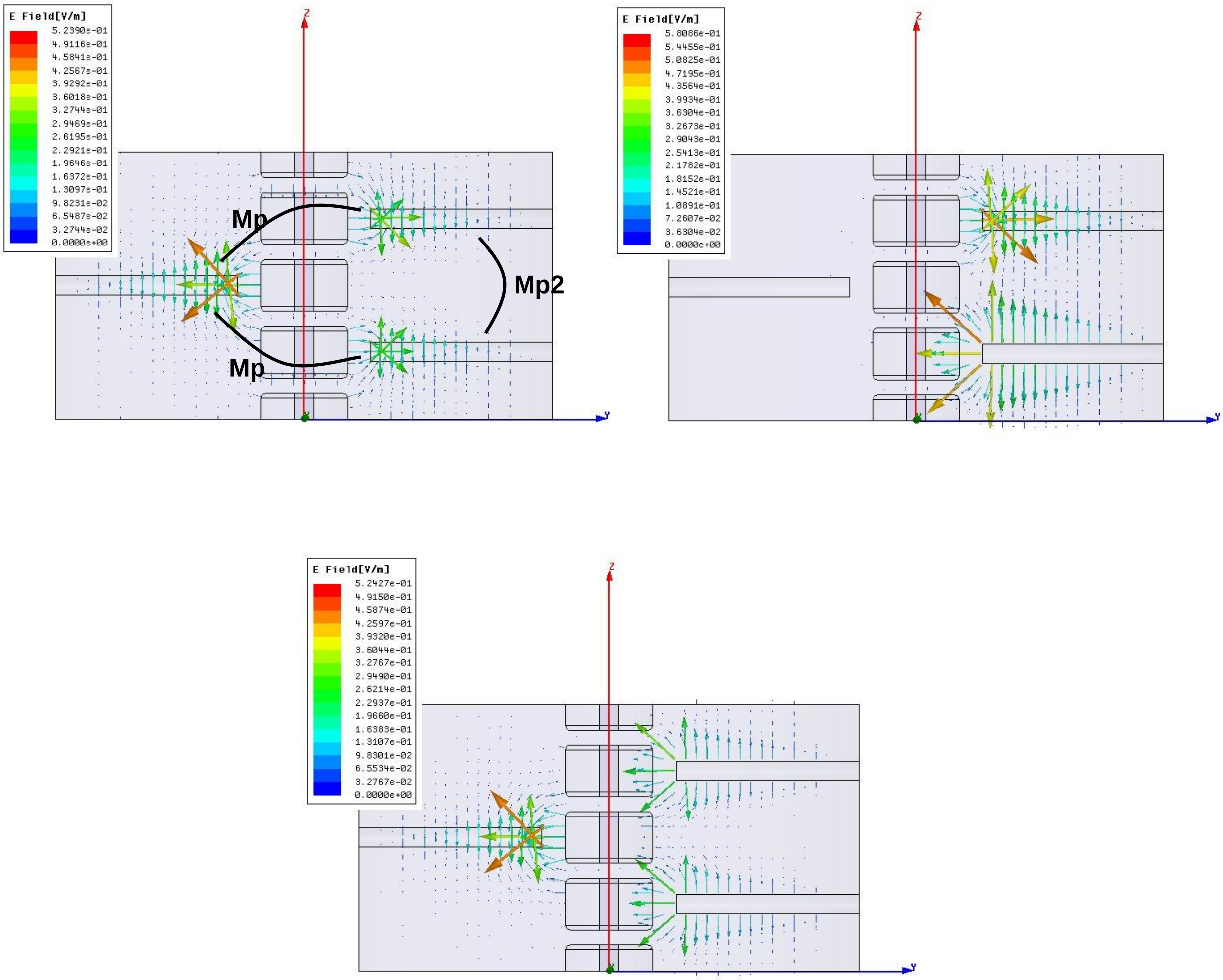

Figure 5.11: electric field pattern of PC modes in a DTL cavity equipped with 3 PCs.

Figure 5.12 illustrates a lattice model equivalent to a DTL tank equipped with PCs. The matrix can be written by showing couplings between resonant elements (Figure 5.11). Graphically it is clear that the coupling k_0 between DT cells can be increased by shortening the cell length (capacitance C decreases), the coupling k_p between PCs and DTs increases when gap PC-DT is smaller (capacitance C_p increases), couplings k_{p1} and k_{p2} between PCs increase with smaller spacing between PCs (increase in the ratio M_p/L_p). Table 5.2 shows coupling coefficient orders of magnitude extrapolated by fitting frequency measurements on the DTL cold model with 7 PCs. The main coupling k_0 is the strongest, the second magnetic coupling k_{p2} between PCs is the weakest.

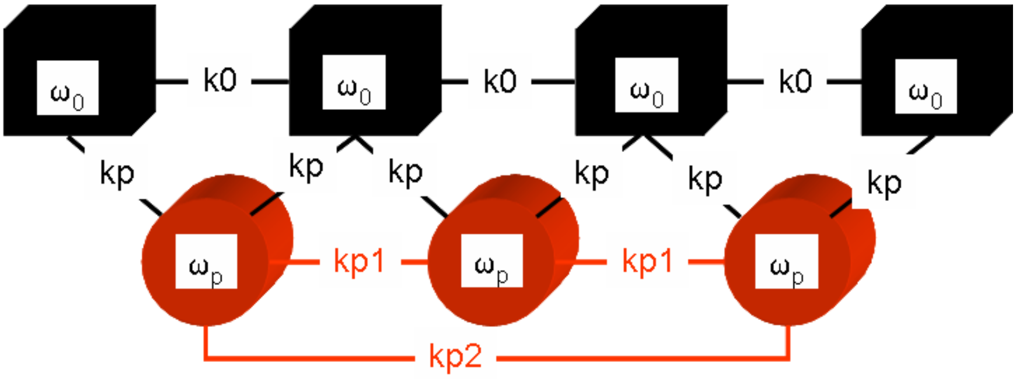

$$\begin{bmatrix} k_0+\omega_0^2 & -k_p & -k_0 & 0 & 0 & 0 & 0 \\ -k_0 & k_p+\omega_p^2 & k_0 & k_{p1} & 0 & k_{p2} & 0 \\ -k_0 & k_p & k_0+\omega_0^2 & -k_p & -k_0 & 0 & 0 \\ 0 & k_{p1} & -k_0 & k_p+\omega_p^2 & k_0 & k_{p1} & 0 \\ 0 & 0 & -k_0 & -k_p & k_0+\omega_0^2 & -k_p & -k_0 \\ 0 & k_{p2} & 0 & k_{p1} & -k_0 & k_p+\omega_p^2 & k_0 \\ 0 & 0 & 0 & 0 & -k_0 & k_p & k_0+\omega_0^2 \end{bmatrix}$$

Figure 5.12: lattice model with couplings between resonant elements. The matrix shows all couplings between elements.

k_0/ω_0^2	k_p/ω_0^2	k_{p1}/ω_0^2	k_{p2}/ω_0^2
2.5	0.25	0.076	-0.031

Table 5.2: normalized coupling factors estimated for DTL prototype with 4 PCs at gap PC-DT = 25 mm.

References

[1] F.E. Terman, “Radio engineer's handbook”, McGraw-Hill 1943.

[2] T. Wangler, “RF Linear Accelerators”, John Wiley & Sons, Inc. 1998, par.3.4.

Chapter 6. Post couplers: tuning procedure and measurements

A DTL cold model with scaled dimensions has been built by KASCT in Saudi Arabia for tuning study (Figure 6.1) [1]. The operating frequency is 538.7 MHz, the tank diameter 340 mm and the DT diameter 58.8 mm, the length is 862 mm. It consists of a 16 cells cavity equipped with holes for PC positioning at each DT, in order to test the effectiveness of stabilization for different PC configurations. The end cells can be easily moved in order to induce a perturbation on the accelerating field.

In this chapter we present a tuning procedure based on the equivalent circuit analysis of the measured frequencies, which allows to calculate the gap PC-DT for field stabilization. The advantage of this method with respect to the usual one [2,3] is in avoiding a large number of bead pulling measurements at different PC lengths. The prediction of the circuit are verified with measurements on the DTL cold model, in cavity configurations with 5 and 7 PCs.

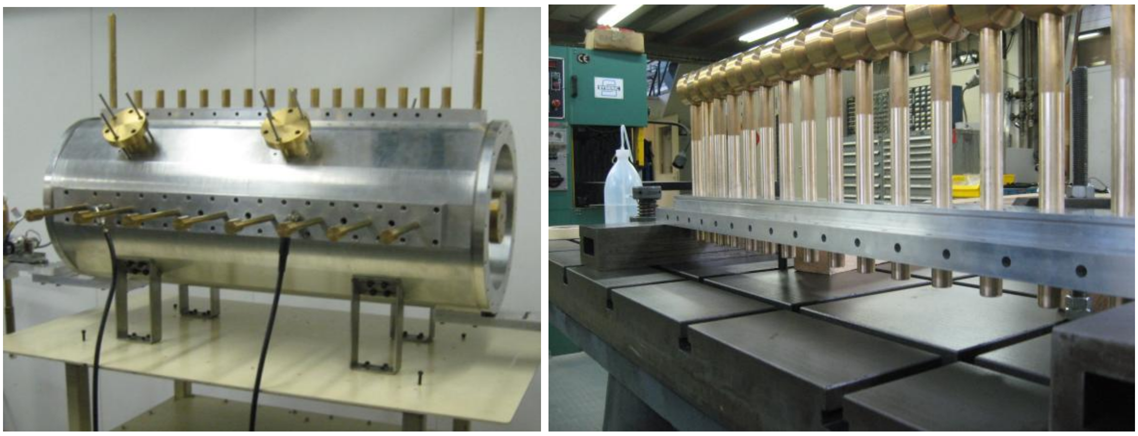

Figure 6.1: DTL cold model at CERN and a view of the drift tubes in the alignment phase.

6.1 Circuit extrapolation of stabilizing post coupler setting

The following results are deduced from the 16 cell DTL cold model present at CERN, equipped with 5 and 7 PCs. Because PCs are every 3 or every 2 drift tube, we minimize the average value of the tilt sensitivity, resulting in a saw-tooth pattern. Tilt

Sensitivity is defined as $TS_i = \left(E0_i^{pert} - E0_i^{unpert} \right) / E0_i^{unpert} \cdot (1/\Delta f)$ and Tilt Sensitivity Slope is the slope of the linear interpolation of the Tilt Sensitivity curve.

A procedure to find an optimum average PC length is the following:

- The gap capacitance C_0 is calculated from a SUPERFISH simulation, using the formula $\frac{1}{2} C_0 V^2 = U$
- Measurement of the TM_{010} and TM_{011} without PCs to calculate the coupling capacitance C between tank and drift tubes (Figure 6.2) (Note: here we make the assumption that all the cells have the same average length, we don't take into account the increasing cell length)
- Measurement of the PC frequency band (at least 3 modes, for example $PC_{highest}$, PC_{lowest}, $PC_{central}$ modes) and of the TM_{010} and TM_{011} modes at different length of the PCs (Figure 6.3)
- Fitting of the measured frequencies with dispersion curves computed by the circuit, by adjusting the circuit parameters ω_0,ω_p, C_p, k_{p1}, k_{p2}
- Insertion of a perturbation δC_0 in the end capacitances of the circuit, which simulates the end cell displacement
- Looking at the fields given by the previously fitted circuits: the goal is to minimize the Tilt Sensitivity (Figure 6.4)
- Extrapolation of the stabilizing PC length from the parameter curves (Table 6.1), looking at the zero of TS_Slope curve (Figure 6.5).

The same analysis has been done for both 5 PCs configuration and 7 PCs configuration.

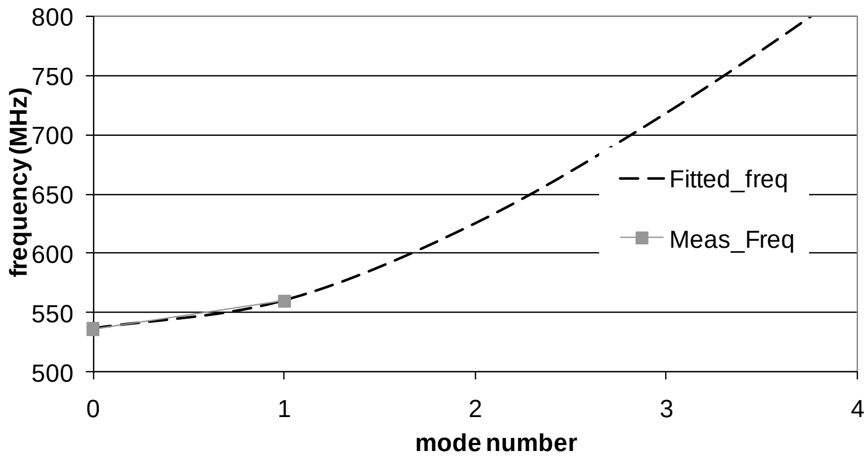

Figure 6.2: TM_{010} and TM_{011} modes measured without PCs and fitted curve.

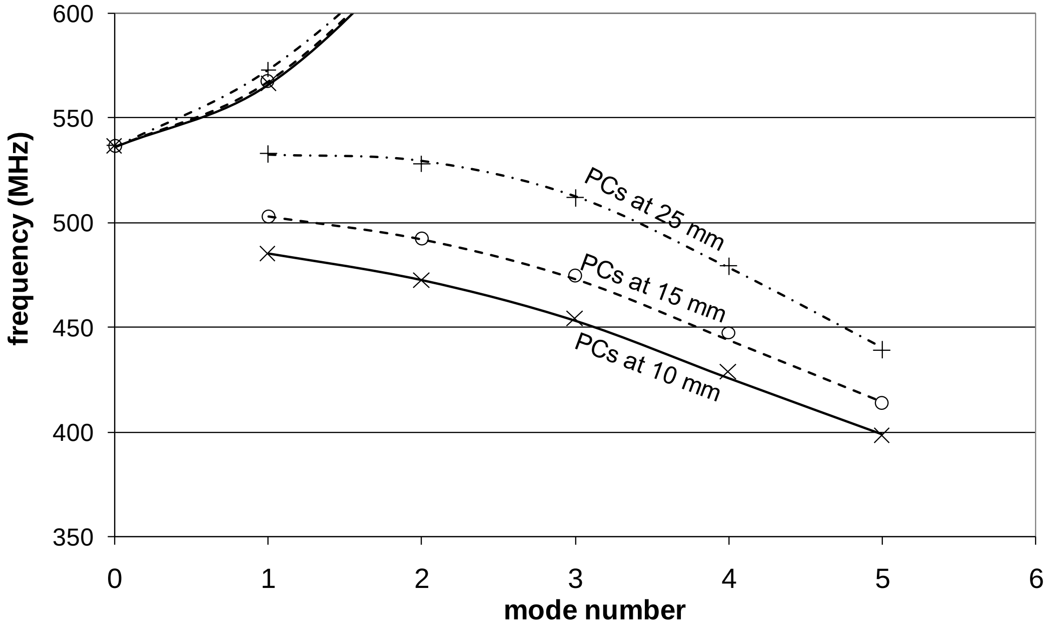

Figure 6.3: frequencies at 3 different values of the gap PC-DT. A larger gap corresponds to a higher PC frequencies and to a larger frequency distance between TM_{010} and TM_{011} modes.

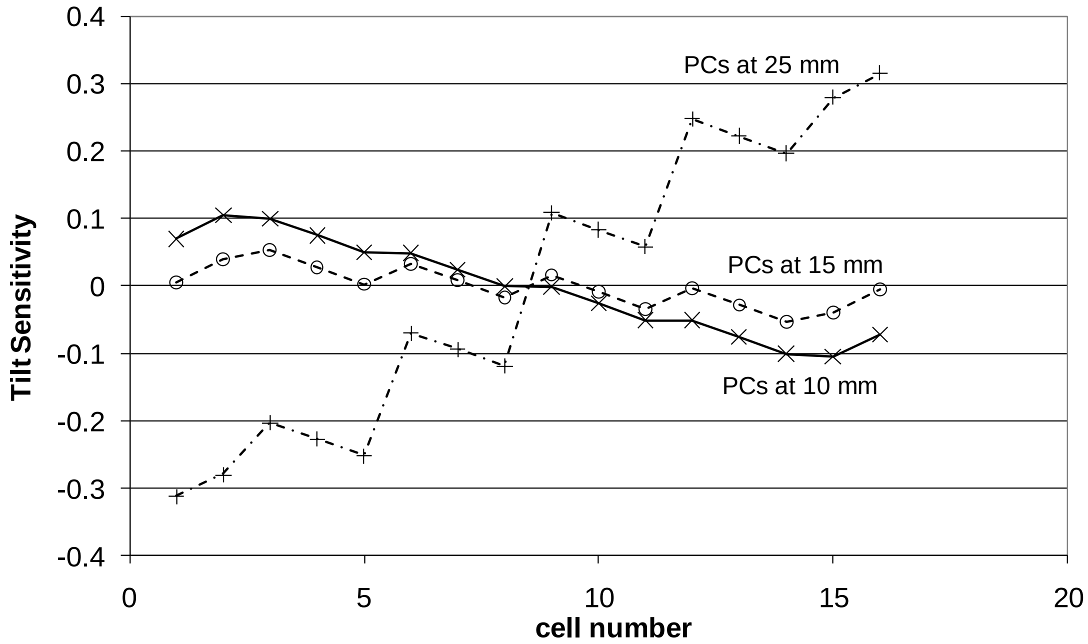

Figure 6.4: E_0 perturbed field calculated by the equivalent circuit. Each curve is associated to a different value of the gap PC-DT.

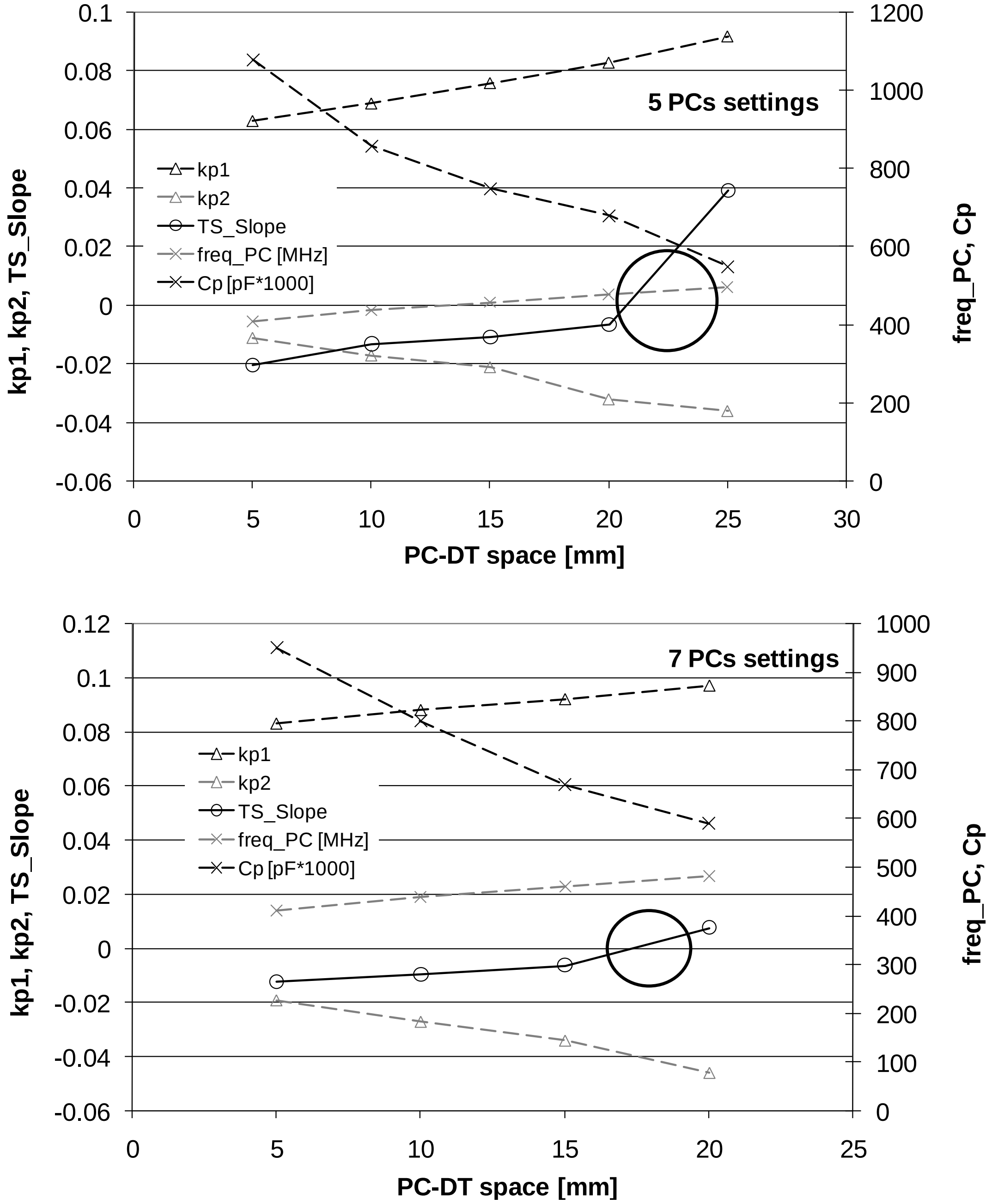

Figure 6.5: circuit parameters and Tilt Sensitivity Slope as function of the gap PC-DT for 5 PCs and 7 PCs configurations. The Tilt Sensitivity zero point is marked.

Stabilizing Parameters							
	gap_{pc} [mm]	ω_p [MHz]	C_p [pF]	k_0/ω_0^2	k_p/ω_0^2	k_{p1}/ω_0^2	k_{p2}/ω_0^2
5 post–couplers	22.5	485	0.62	2.3	0.20	0.087	-0.033
7 post–couplers	19.0	477	0.61	2.3	0.19	0.096	-0.044

Table 6.1: stabilizing PC setting for DTL cold model equipped with 5 PCs and 7 PCs.

Let us consider the ratio $r = \dfrac{\Delta(TS\_Slope)}{\Delta gap_{PC-DT}}$ as the sensitivity criterion for the PC length adjustment. This sensitivity is larger in the case of 5 PCs, where r = 9 around the optimum gap = 22.5 mm, than in the case of 7 PCs, where r = 2 around the optimum gap = 19 mm. An increased sensitivity to the PC length adjustment is related to a larger gap PC-DT and it makes more difficult to fix the optimum PC length for stabilization.

6.2 Measurements on DTL cold model

In order to verify the equivalent circuit results, we use the Tilt Sensitivity method to find the stabilization length on the DTL cold model equipped with 5 and 7 PCs.

First, we need a measurement of the reference field (Figure 6.6) to be stabilized, which is called the "natural field distribution" of the tank [4]. In order to verify the effectiveness of PCs for stabilization of the accelerating field, it is not necessary to refer to a perfectly flat field.

We perturb the first and the last gap to create a tilt in the field (Figure 6.7).

Now we start with a small gap PC-DT (15 mm), and as expected from the equivalent circuit, PCs are not able to stabilize the tilt of the field (Figure 6.8).

If gap is too large (25 mm for 5 PCs, 22 mm for 7 PCs), the field reverses its slope, and we reach over-compensation (Figure 6.9).

Finally we set the PCs at gap_{pc} calculated with the equivalent circuit: 22.5 mm gap for 5 PCs, 19 mm gap for 7 PCs. One can see the tilt sensitivity curve approaching to zero, except that for the cells close to the tank ends (Figure 6.10).

This effect can be mitigated by adjusting the gap_{pc} in order to take into account the increasing cell length in this model. What we expect is an optimum PC configuration where the central PC is kept at the computed gap_{pc}, but with smaller gap_{pc} at the low energy side, larger gap_{pc} at the high energy side (Figure 6.11). Table 6.2 shows the final PC settings.

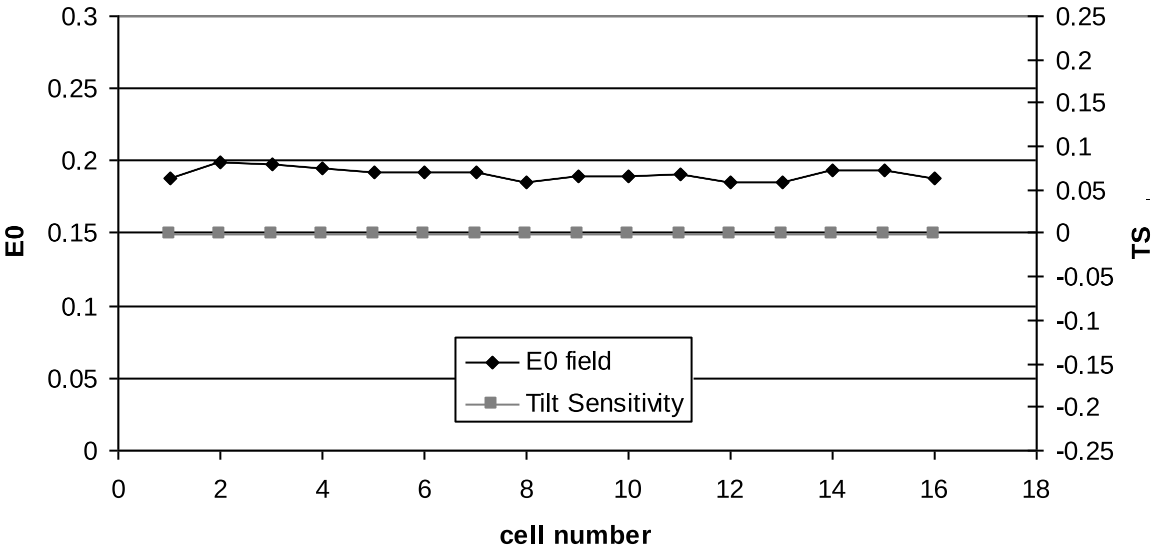

Figure 6.6: reference field and tilt sensitivity.

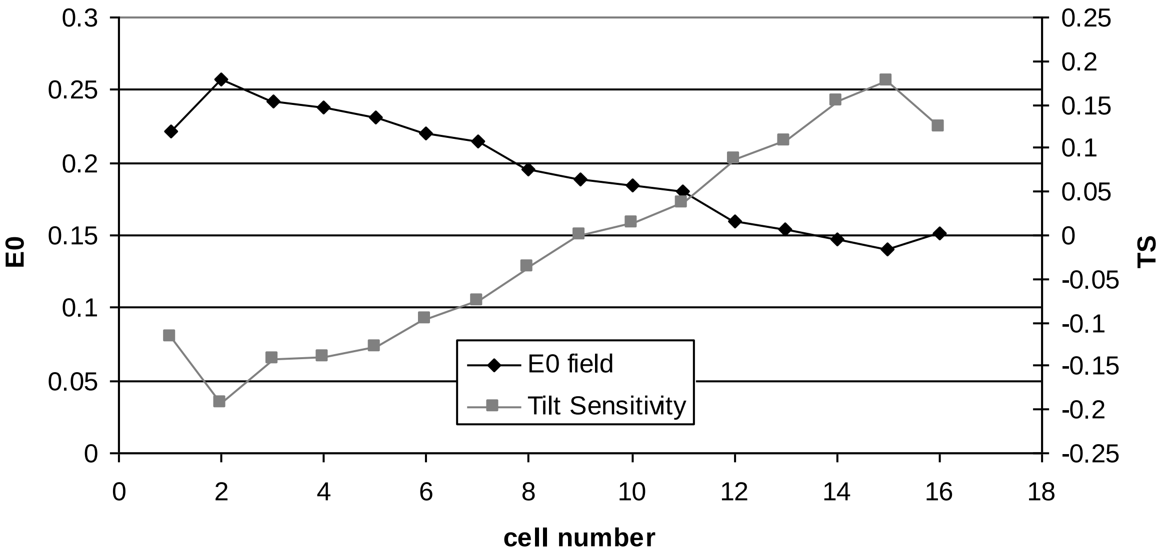

Figure 6.7: perturbed field and tilt sensitivity.

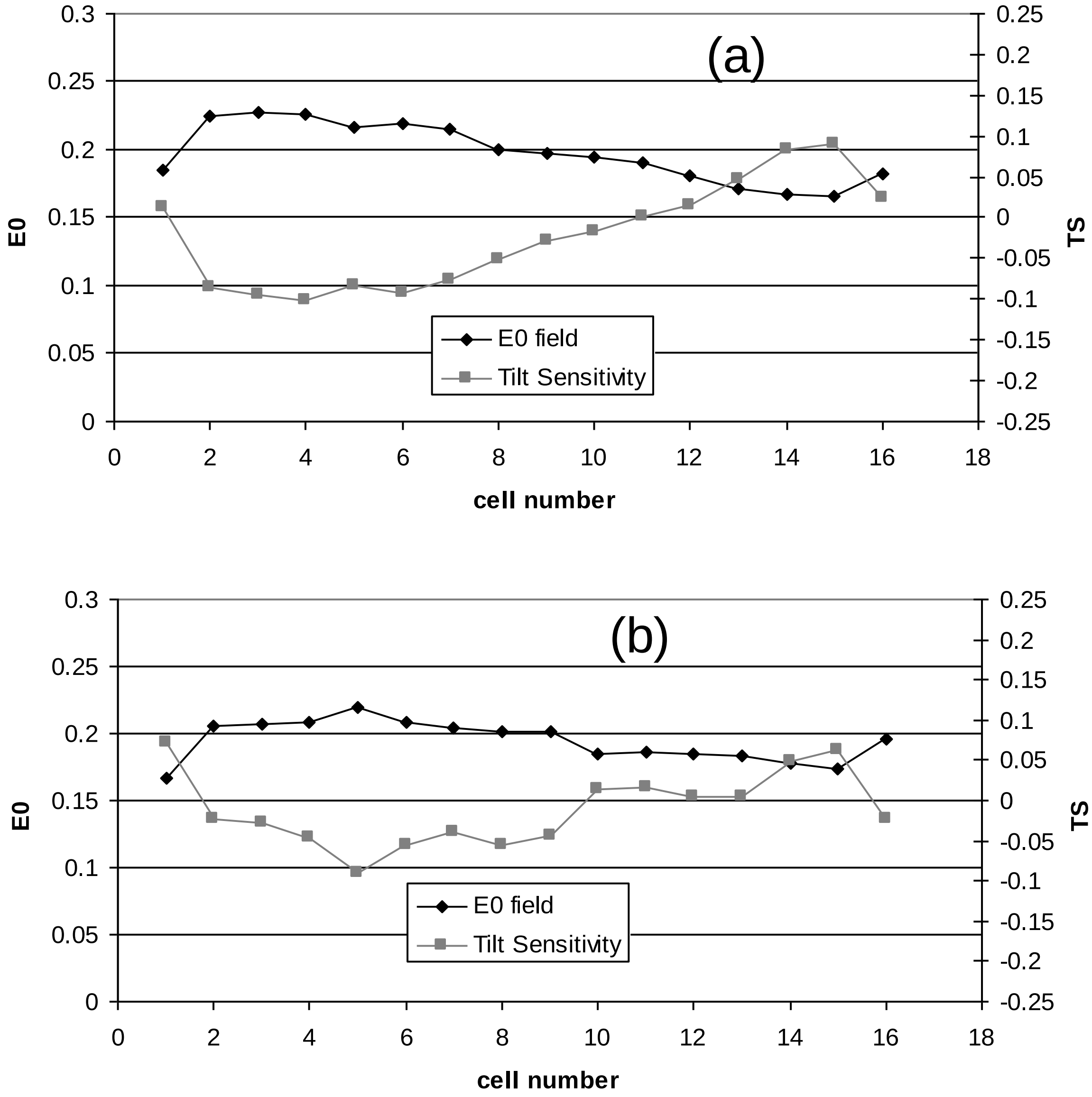

Figure 6.8: gap PC-DT = 15 mm is too small for both 5 PCs (a) and 7 PCs (b) case.

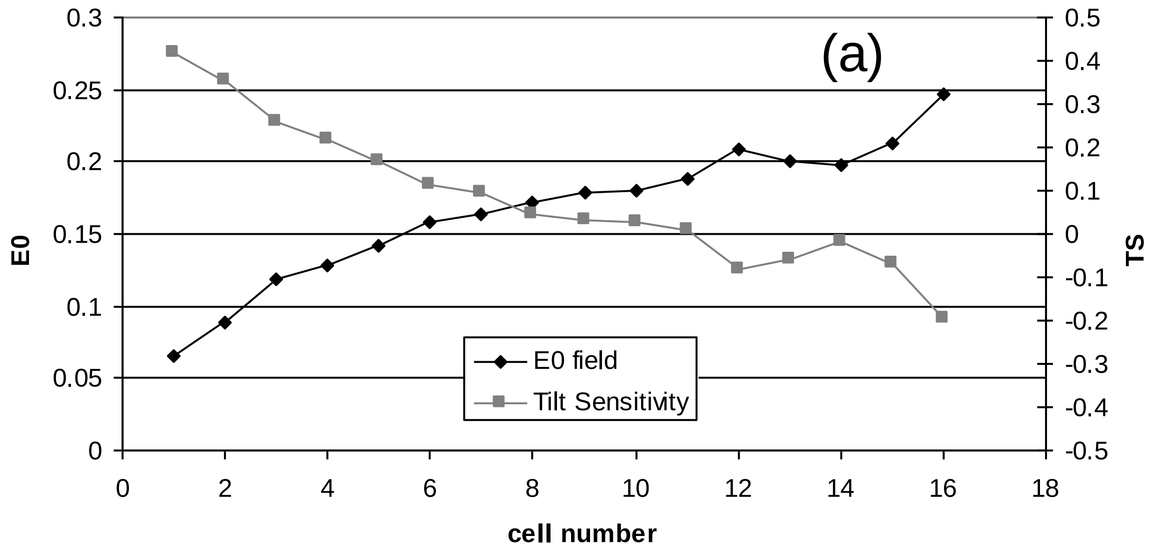

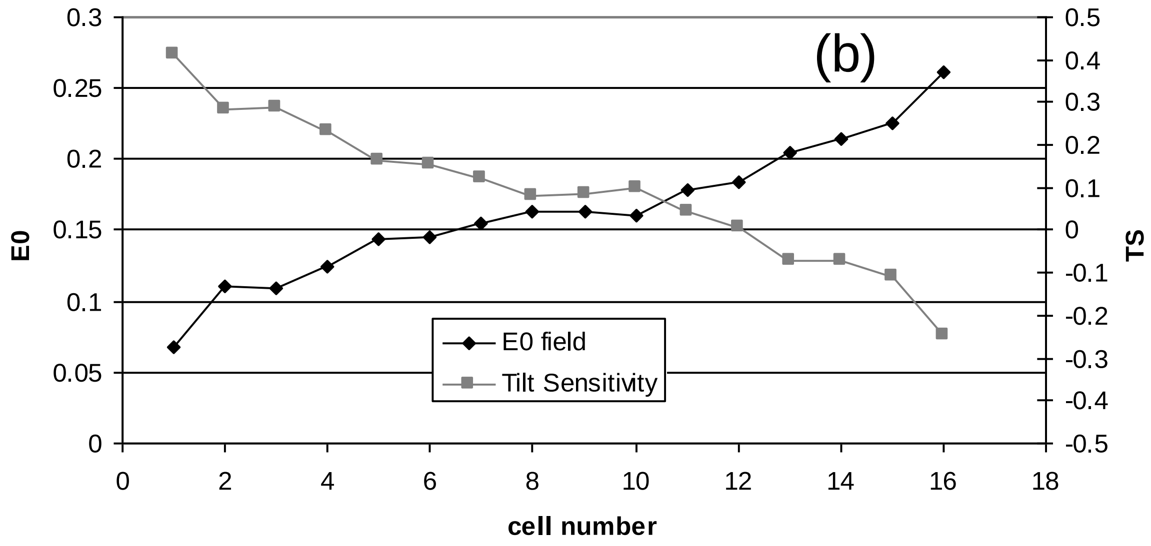

Figure 6.9: (a) gap PC-DT = 25 mm is too large for 5 PCs configuration. (b) gap PC-DT = 22 mm is too large for 7 PCs configuration.

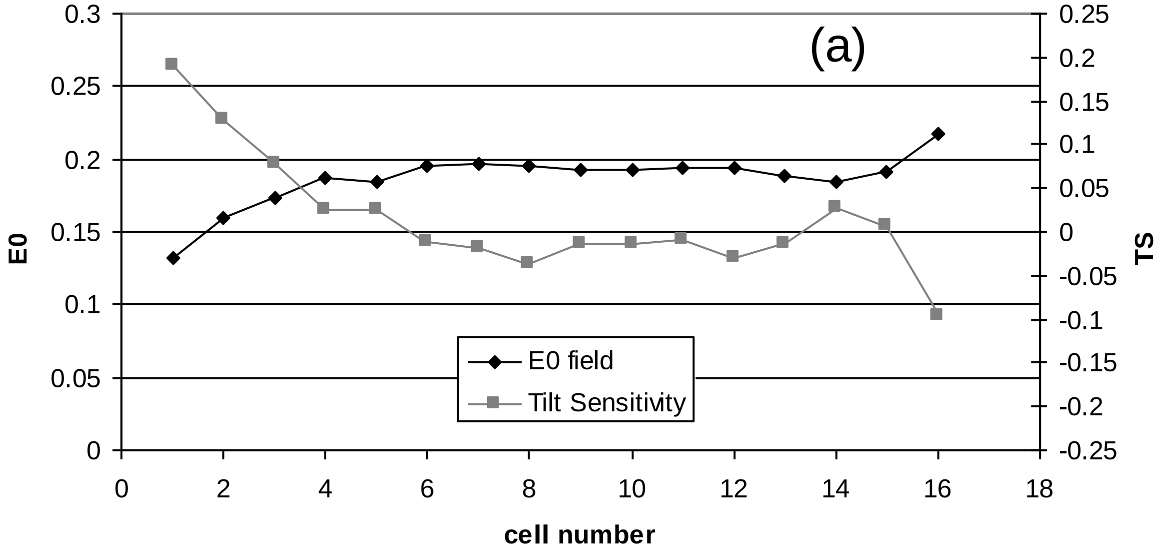

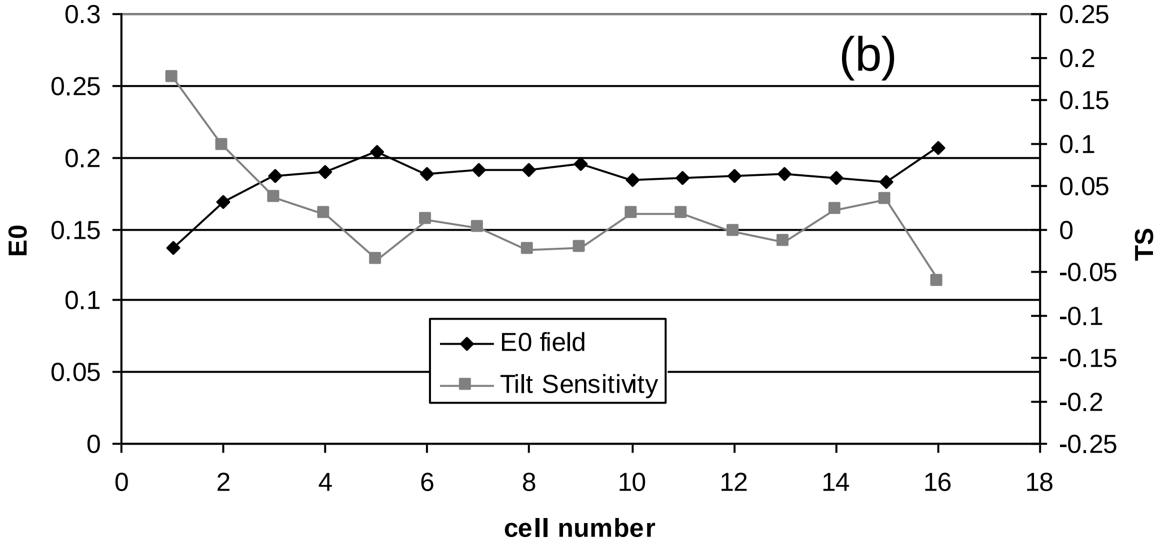

Figure 6.10: (a) 5 PCs are set all at the gap_{pc} = 22.5 mm, as calculated by the equivalent circuit simulation (Figure 6.5). (b) 7 PCs are set all at the gap_{pc} = 19 mm, as calculated by the equivalent circuit simulation (Figure 6.5).

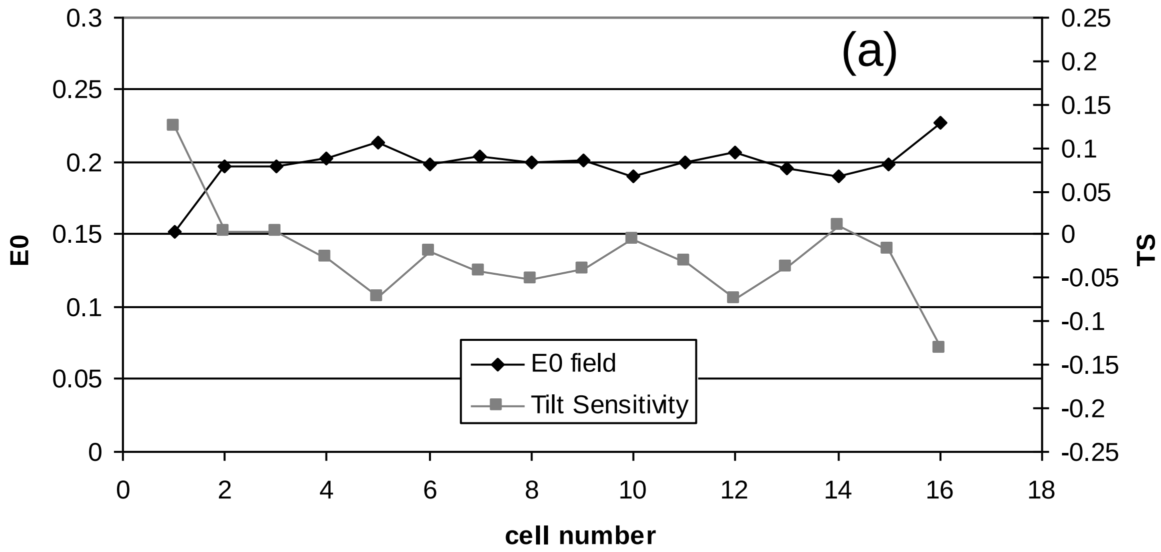

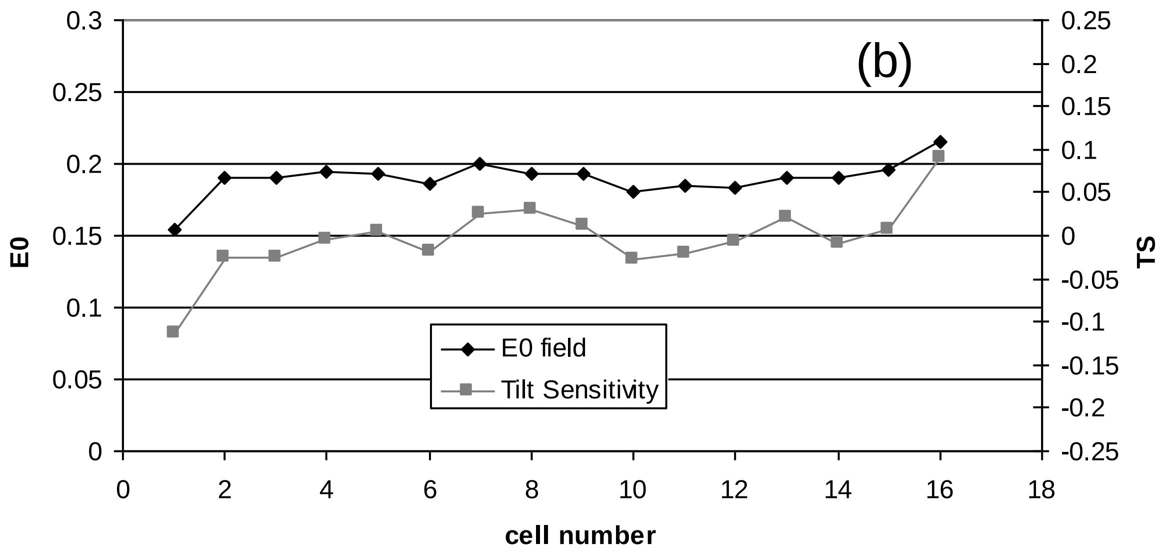

Figure 6.11: PCs are adjusted taking into account of the increasing length of the cells for 5 PCs (a) and 7 PCs (b).

PC number	1	2	3	4	5	-	-
Gap [mm]	21.5	22	22.5	23	23.5	-	-
PC number	1	2	3	4	5	6	7
Gap [mm]	17.5	18	18.5	19	19.5	20	20.5

Table 6.2: Optimum PC settings for DTL cold model at CERN.

References

[1] N. Alharbi, F. Gerigk and M. Vretenar, “Field Stabilization with Post Couplers for DTL Tank1 of Linac4”, Tech. Rep. CARE-Note-2006-012-HIPPI, CARE, 2006.

[2] G. Dôme, “Review and survey of accelerating structures”, in “Linear Accelerators” (ed. by P. Lapostolle and A Septier) North-Holland Publ. Co., 1969.

[3] J. M. Potter, “Drift Tube Linacs”, in “Handbook of Accelerator Physics and Engineering” (ed. By A. Wu Chao and M. Tigner) World Scientific Publ. Co., 2006.

[4] J. Billen, private communication.

Chapter 7. Conclusions

We can now summarize results obtained and illustrated in previous chapters, following the scheme presented in the Introduction.

2D simulations, performed with Superfish code, are reliable for the calculation of frequency detuning effect and power dissipation due to the post coupler insertion, as shown by the comparison with measurements taken on the DTL "hot" prototype. This comparison shows also that 2D simulations cannot give any hint about the coupling between post couplers (PCs) and accelerating cells.

3D simulations, performed with HFSS code, compute cavity fields and frequency modes in agreement with measurements taken in DTL hot prototype. The stabilizing effect of PCs for the accelerating mode is interpreted on the basis of a mutual cancelation of the perturbations induced by the TM_{011} and PC_1 mode. 3D simulations were undertaken to study PCs mode frequencies as a function of number of PCs per meter and of the gap PC-DT. In quasi-static approximation, formulas for estimation of PC circuit parameters as a function of the PC geometry were defined and verified to be consistent with simulation results. 3D simulations allow a graphical picture of mode patterns in order to understand couplings between different elements inside the cavity.

The equivalent circuit for a DTL equipped with PCs is exhaustive. It gives an explanation of stabilizing PC settings in terms of circuit parameters and shows clearly that PC frequency tuning is indissolubly related to the PC-DT coupling. The matrix form of circuit equations allows the introduction of nearest neighbor coupling and next nearest neighbor coupling between PCs. With the insertion of couplings, experimental dispersion curves are precisely reproduced.

A tuning procedure based on the equivalent circuit and on frequency measurements was defined, tested and validated with measurements on the DTL aluminum model in 2 different PC configurations.

Appendix A. Cavity figures of merit

There are several figure of merit used to characterize accelerating cavities. We will introduce most important ones in this Appendix [1, 2].

First of all we define the average axial field E0 for a single accelerating cell of length L_{cell} as

$$E_0 = \frac{V_0}{L_{cell}} = \frac{\int_{Lcell} \overline{E}(0,z) \cdot d\overline{z}}{L_{cell}}.$$

Power P is dissipated from resistive losses in the walls of the cavity to maintain the fields. The figure of merit for stored energy U per unit power loss P_{cav} is the *quality factor*

$$Q_0 = \omega U/P_{cav}.$$

The *shunt impedance* measures how effective the cavity is in producing an axial electric field per unit power loss, and it is defined by

$$r_s = (V_0)^2/P_{cav}.$$

The energy gain of an arbitrary particle with charge q traveling through the accelerating cell on axis is

$$\Delta W = q \int_{L_{cell}} E(0,z)\cos[\omega t(z)+\phi]dz$$

where ϕ is the phase of the electric field relative to the crest at t = 0. The equation can be written in the form

$$\Delta W = qV_0 T\cos\phi$$

where the transit time factor is defined by

$$T \equiv \frac{\int_{Lcell} E(0,z)\cos\omega t(z)dz}{\int_{Lcell} E(0,z)dz} - \tan\phi \frac{\int_{Lcell} E(0,z)\sin\omega t(z)dz}{\int_{Lcell} E(0,z)dz}.$$

The maximum energy gain of a particle in an accelerating gap is then

$$\Delta W = qV_0T = qE_0L_{cell}T.$$

The effective shunt impedance measures the efficiency for delivering energy to a particle per unit power loss. It is defined by

$$r = \left(\frac{\Delta W}{q}\right)^2 \frac{1}{P_{cav}} = \frac{E_0TL}{P_{cav}}^2 = r_sT^2.$$

The shunt impedance per unit length is simply

$$Z = \frac{r_s}{L} = \frac{E_0^2}{P_{cav}/L}.$$

The effective shunt impedance per unit length measures the acceleration efficiency per unit length

$$ZT^2 = \frac{r_s T^2}{L} = \left(\frac{\Delta W}{qL}\right)^2 \frac{1}{P_{cav}/L}.$$

Figure A.1 shows a block diagram of an RF system for an accelerating cavity. The electromagnetic energy is provided by the RF generator, like a klystron. The electromagnetic energy travel through the waveguide system and it is coupled to the cavity by the power coupler. If some power is reflected back by from cavity, the circulator directs it to the matched load, where it is dissipated.

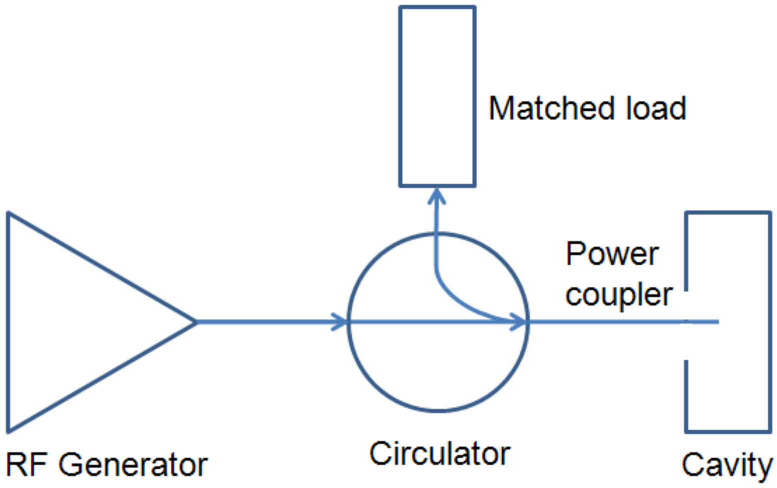

Figure A.1: block diagram of an RF system for an accelerating cavity.

For a cavity coupled to a waveguide, it is conventional to define a general parameter that is a measure of the waveguide-to-cavity *coupling strength*, called the parameter β, which is defined by

$$\beta = \frac{P_{ex}}{P_{cav}} = \frac{Q_0}{Q_{ex}}$$

where P_{ex} is defined as the external power radiated from the cavity when the generator is turned off, and $Q_{ex} = \omega U/P_{ex}$. This parameter "measures" the capability of the power coupler of providing the necessary power to the cavity. In fact if $\beta < 1$ the waveguide and cavity are said to be undercoupled. If $\beta > 1$ the waveguide and cavity are said to be overcoupled. If $\beta = 1$ the waveguide and cavity are said to be critically coupled.

The coupling strength β is related to the reflection coefficient Γ according to the formula

$$|\Gamma| = \frac{V_-}{V_+} = \sqrt{\frac{P_-}{P_+}} = \left|\frac{\beta - 1}{\beta + 1}\right|.$$

References

[1] T. Wangler, “RF Linear Accelerators”, John Wiley & Sons, Inc. 1998, par. 2.5.

[2] T. Wangler, “RF Linear Accelerators”, John Wiley & Sons, Inc. 1998, par. 5.4.

Appendix B. High Power Test on DTL hot Prototype

B.1 Low power RF measurements for cavity characterization

Low power measurements have been performed in order to know resonance frequency, quality factor Q_{cav} of the cavity and coupling strength β of the iris coupler. DTL hot prototype is equipped with two small pick-ups for low power measurements and RF monitoring in high power operation. Vacuum and RF tightness are provided by Helicoflex® type joints. For low power measurements a HP Network Analyzer is used.

Resonance frequency with tuners completely inserted and post couplers at 182 mm length is $f_0 = 351.973$ MHz, slightly lower than the design frequency because of a re-machining which enlarged the tank diameter of about 1.2 mm.

The quality factor Q_{cav} is measured using 2 pick-up's as input and output ports. The bandwidth of an oscillator is defined [1] as the frequency difference Δf between the two points on each side of the resonance curve, where the voltage is lower than the peak value by $\sqrt{2}$. Network Analyzer gives transmission parameter S_{21} from port 1 to port 2 measured in dB, then two half power points are at -3 dB with respect to the resonance peak. This measurement gives the loaded quality factor $Q_L = f/\Delta f = Q_{cav}/(1+\beta_1+\beta_2)$ where β_1 and β_2 are coupling coefficient of two cavity pick-up's. Since β_1 and β_2 are much smaller than 1, we have directly $Q_{cav} \approx Q_L = 33700$ (80% of the nominal $Q_0 = 42000$).

The input waveguide (half-height WR2300) is connected to the iris coupler, in order to measure the coupling strength β between waveguide and cavity. In this case port 1 is the transition from coaxial cable to waveguide (N-WR2300 transition) and port 2 is the pick-up. Measurement of half power points gives $Q_L = f/\Delta f = Q_{cav}/(1+\beta+\beta_{pick\text{-}up})$, but $\beta_{pick\text{-}up} \ll \beta$, then we have $Q_L = Q_{cav}/(1+\beta) = 18500$. For the previous value of $Q_{cav} = 33700$ the coupling factor is $\beta = 0.82$.

From measurements of standing wave ratio SWR and reflection coefficient Γ at resonance it is possible to have a check of β value. Microwave theory says that $|\Gamma| = |(\beta-1)/(\beta+1)|$ and $SWR = (1+|\Gamma|)/(1-|\Gamma|)$ [1]. From these relations we obtain that

$\beta = 1/SWR$ if waveguide and cavity are undercoupled ($\beta < 1$), $\beta = SWR$ if they are overcoupled ($\beta > 1$), $\beta = SWR = 1$ if they are critically coupled ($\beta = 1$) and in this case $\Gamma = 0$ (no reflection). Since S_{11} circle in the Smith Chart representation has diameter < 1 (Figure B.1), our case is undercoupled. The measurement of SWR = 1.14 gives $\beta = 0.88$. A measurement performed after cavity installation in SM18 bunker confirms this result, in fact $S_{11} = -22.3$ dB (Figure B.2) means $|\Gamma| = 0.0767$, SWR = 1.17 and finally $\beta = 0.85$. With the previous value of Q_L we obtain $Q_{cav} = Q_L(1+\beta) = 18500 \cdot 1.85 = 34200$.

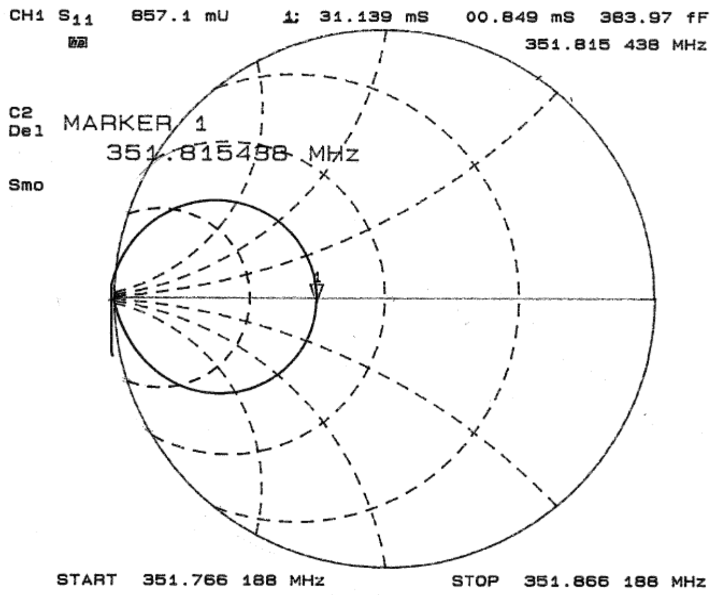

Figure B.1: S11 circle in Smith Chart shows that waveguide and cavity are undercoupled.

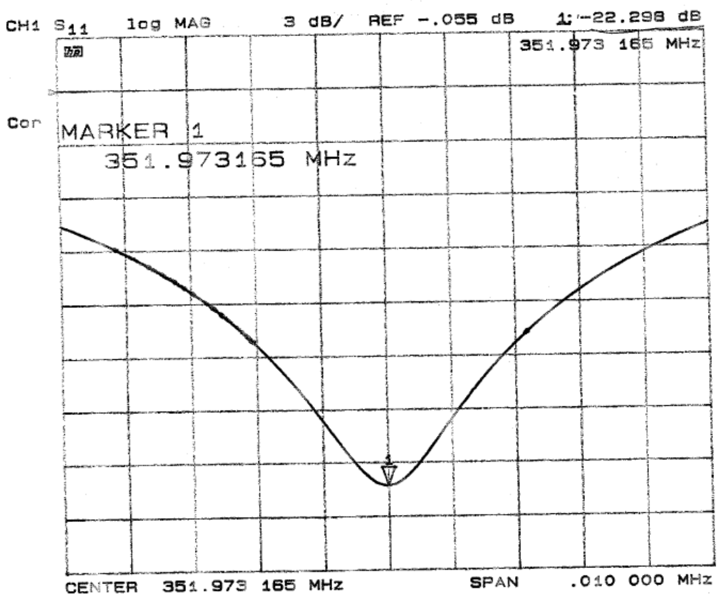

Figure B.2: measurement of S_{11} of DTL prototype.

These measurements are confirmed by 3D simulations with HFSS. Only cells 7 and 8 of the prototype are simulated, for their location just below the iris coupler. Simulation results are scaled to the real power dissipation of the prototype ($Q_{cav} = 0.8 \cdot Q_0$). Simulations are performed with 2 methods (Figure B.3):

1. Driven modal simulation: tank, drift tubes, stems and iris coupler are dissipative (copper conductivity $\sigma = 5.8 \times 10^7$ S·m), while waveguide is supposed to be lossless. 3D code computes directly SWR and S_{11}. Coupling coefficient β can be extracted using the above mentioned relations. The reference port 1 is located at the same plane of N-WR2300 transition.
2. "Balleyguier's" simulations [2]: structure is completely lossless. Two eigen-mode simulations are performed, with different boundary conditions at the reference plane (perfect magnetic or perfect electric). Mesh is the same for both simulations. Results are combined in order to obtain the external quality factor Q_{ext} of iris coupler, and from this $\beta = Q_{cav}/Q_{ext}$ is calculated.

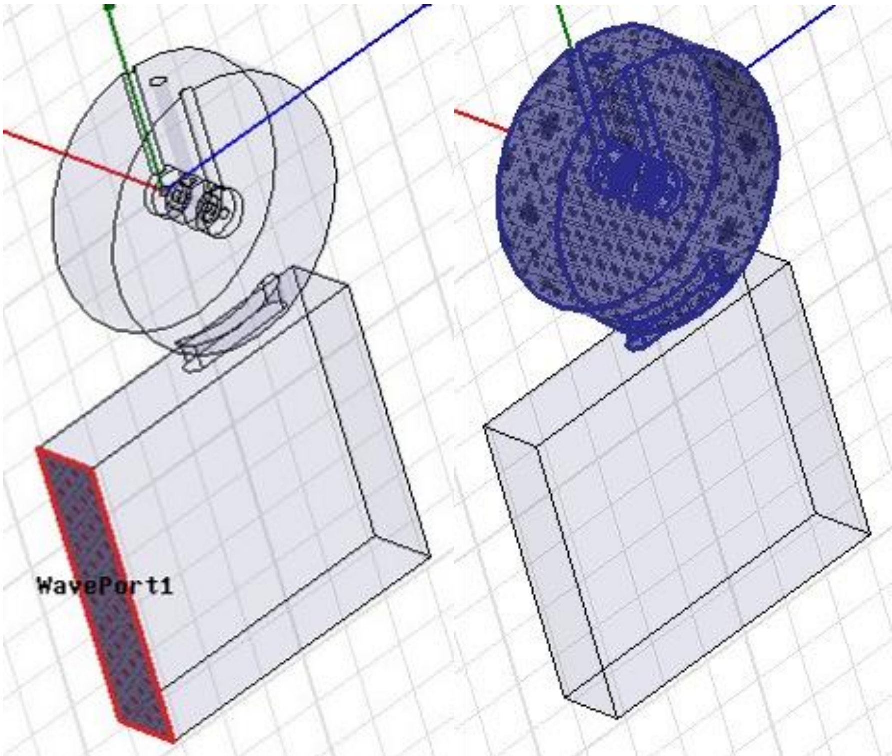

Figure B.3: geometry used for simulations of coupling factor β. In picture on left, reference wave port is marked. In picture on right, dissipative surfaces used in driven modal simulation are marked.

Simulation results are listed in Table B.1 in comparison with measurements. Agreement between simulations is 1.5%, and between simulations and measurements is 10%.

	Measurements	Driven Modal Sim.	Balleyguier's Sim.
β	0.85	0.95	0.93

Table B.1: comparison between measurements and simulations of waveguide-cavity coupling factor β.

Finally we can summarize cavity RF parameters:

- cavity frequency is f_0 = 351.973 MHz with tuners completely inserted and post couplers 182 mm long;
- quality factor is Q_{cav} = 34500, about 80% of nominal value, simulated with Superfish code;
- coupling strength is β = 0.85, for a power reflection of $\Gamma^{-2} = P_-/P_+ = 0.6\%$.

B.2 Bead pulling measurements and post couplers setting

Bead pulling measurements have been performed in order to check field flatness and set post coupler length for stabilization.

Measured reference field E_0 is shown in Figure B.4. The curve shows a 30% slope, due to the data analysis based on the integration of the measured field E(z). Since for post coupler setting it is sufficient to have a reference field not necessarily flat, we can use curves from integration analysis.

Post coupler lengths are calculated with procedure described in Chapter 6. Stabilized field shown in Figure B.6 is obtained with a post coupler length of 182 mm.

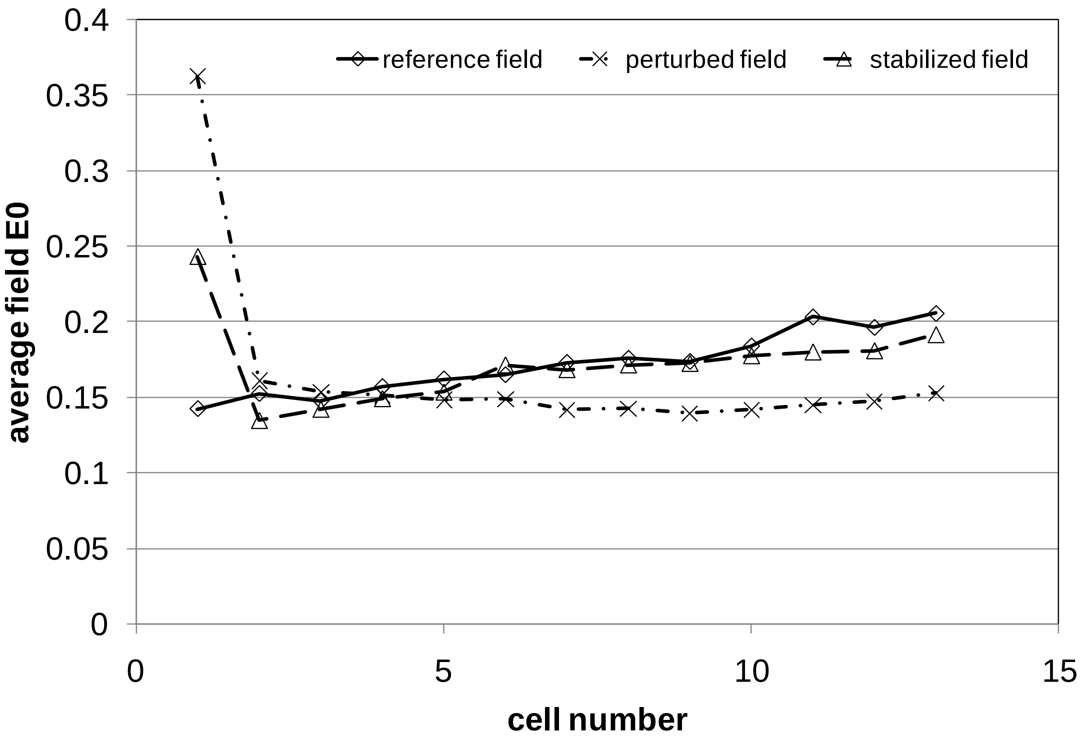

Figure B.4: field stabilization with post couplers.

B.3 Power measurement calibration

Three power signals are measured during cavity conditioning:

1. P_+: the incident power from klystron to the DTL, measured by a directional coupler on the waveguide, located about 1 meter before the iris coupler;
2. P_-: the power reflected from DTL to the waveguide, measured by a second directional coupler located at the same point;
3. P_{cav}: the power in cavity, measured by the two pick-ups on the tank wall.

Directional couplers on the waveguide are calibrated using a Network Analyzer, two transitions N-WR2300 and 50 Ω matched loads (Figure B.5). One coupler measures P_+, the other P_-. For each one we need to know the attenuation, which is the ratio between power in waveguide and power extracted by the coupler. A second parameter to be known is the directivity of the directional coupler, which gives the capability of distinguishing forward and reverse power direction and finally gives the measurement error. Measurements at 352 MHz give:

- P_+: attenuation = -50 dB, directivity = 32 dB (error on P_+ < 1/1000);
- P_-: attenuation = -50 dB, directivity = 22 dB (error on P_- < 4/1000).

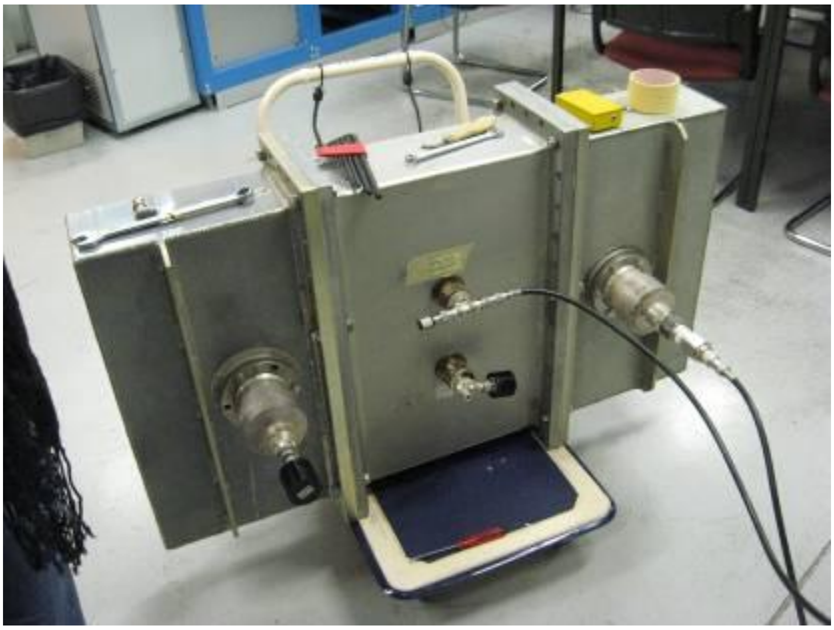

Figure B.5: directional coupler calibration.

In order to characterize the attenuation of cavity pick-ups, the input waveguide with transition N-WR2300 is installed. The pick-up is rotated up to have attenuation $P_{pickup}/P_+ = -50$ dB. We assume to have the same attenuation for power in cavity: $P_{pickup}/P_{cav} = P_{pickup}/P_+ = -50$ dB. This assumption is true only if two conditions are satisfied:

1. pick-up coupling factor $\beta_{pick\text{-}up} << 1$ ($P_{pick\text{-}up} << Pcav$);
2. iris coupling factor $\beta \approx 1$.

In fact we have that $P_+ = P_{cav} + P_- + P_{pick-up}$ and, considering that $P_- = (\Gamma^{-2}) \cdot P_+$, if $P_{pickup} << P_{cav}$ we obtain the following relation: $P_{cav} = P_+ \frac{4\beta}{\beta+1^{\;2}}$. We know that $P_+/P_{pickup} = 50$ dB, then substituting P_+ we obtain $P_{cav} = P_+ \frac{4\beta}{\beta+1^{\;2}} \approx P_{pick-up} 10^5$. This relation is fully correct for $\beta=1$. In our case $\beta=0.85$, the approximation is correct at 99.3%, as Figure B.6 shows.

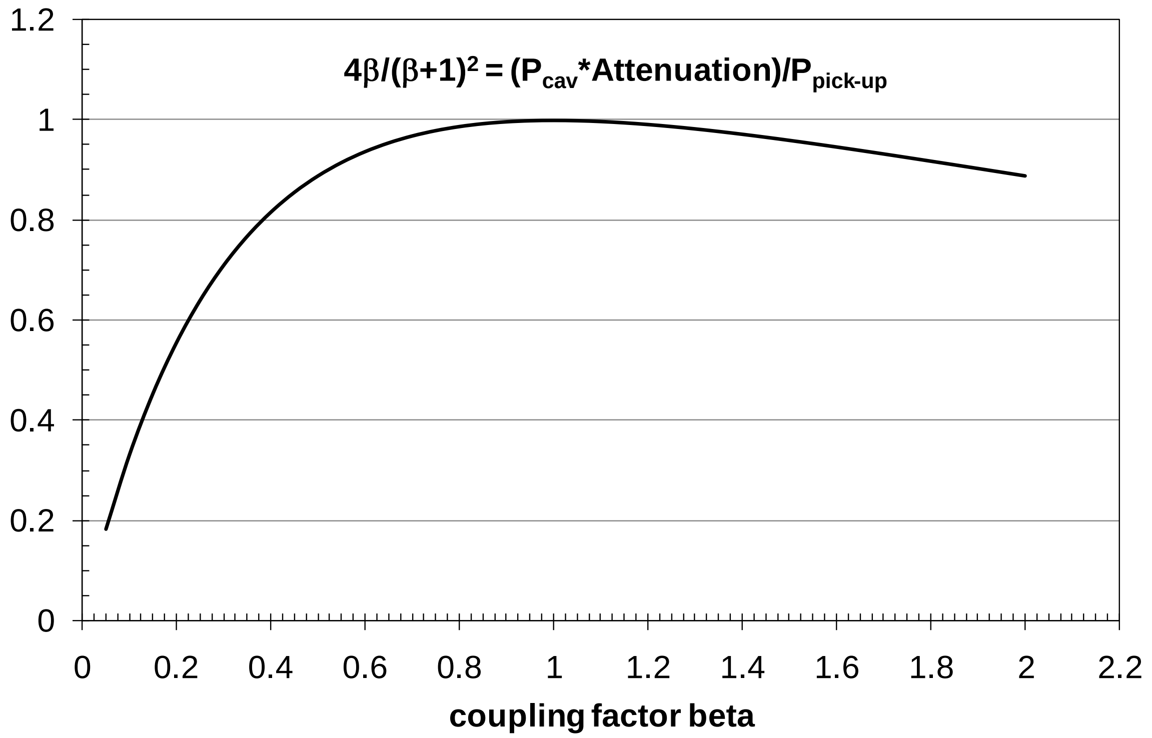

Figure B.6: approximation on P_{cav} measurement as a function of coupling factor β.

Finally attenuation of cables from pick-up to the control room is measured with a signal generator at the beginning of the line and a power meter at the end, giving 26.54 dB attenuation. The overall attenuation for RF power signals from cavity is 76.54 dB.

B.4 High power test

The goal of this test is to achieve the nominal field level of 3.3 MV/m. Considering cavity Q, a peak power of P_{cav} = 220 kW is required for this field level. The minimum duty cycle for Linac4 is 0.1%, but the structure must be tested also at 10% duty cycle to satisfy SPL operation.

The power source is a LEP-type klystron (1 MW, CW). The klystron runs in dc power and the input signal is generated by a Rhode & Schwartz signal generator in the control room. The signal frequency and the input signal level are given to a pre-amplifier connected to the klystron. Pulse length and repetition rate are separately controlled by a pulse generator. The klystron voltage is limited to 58 kV, the maximum cathode current is 9.6 A, for a dc power of about 560 kW. Since klystron efficiency is estimated to be 60%, maximum expected input power from klystron should be $P_+ \approx$ 330 kW.

Temperatures are monitored by a set of thermocouples installed on drift tubes, tuners, post couplers and on the iris coupler. The overall water flow is 30 l/m, the water temperature is 26°C. Water flows are also locally monitored on the iris coupler, on the cavity tank, on post couplers and drift tubes. The input water pressure is 6.5 bar, the output pressure is 3.5 bar. The water flow is maximum in drift tubes (3 l/m), in fact water drift tube temperatures are constant at 26°C during the test. Other points, like tuners and end cones, have been monitored also at 40°C and 55°C respectively. Vacuum level in the cavity is in the order of 10^{-7} mbar, with interlock at $9.0 \cdot 10^{-6}$ mbar.

During cavity conditioning the RF duty cycle is increased with different values of pulse length and repetition rate. P_+ is raised by setting the level of the signal generator. The signal generator frequency is adjusted to follow the cavity resonance frequency and maximize P_{cav}. Each level of P_+ is kept up to the stabilization of vacuum and power level in the cavity.

All RF signals are shown in an oscilloscope in the control room (Figure B.8).

Figure B.7: view of the high power installation of DTL prototype in SM18 bunker.

Figure B.8: view of the instrumentation in the control room.

If all power goes to enhance the cavity field level, energy balance should be $P_+ = P_{cav} + P_-$. In our case there is some incongruence, because maximum of P_{cav} does not coincide with minimum of P_-, and when $P_- = 0$, P_{cav} is different from P_+. Part of P_+ is lost in dissipative phenomena (dark current, electron loading phenomena). We assume to be at resonance frequency when $P_- = 0$. Figure B.9 shows that P_+ and P_{cav} curves match up to -23 dBm of signal generator level ($P_- = 0$). Above -23 dBm power increases not linearly because of the klystron saturation. Furthermore the difference between P_+ and P_{cav} indicates power lost in electron loading phenomena.

After two weeks of conditioning nominal field level has been achieved with $P_{cav} = 240$ kW, and Linac4 duty cycle has been exceeded with 20 Hz repetition rate and 1.3 ms pulse length (duty cycle = 2.6%). Figure B.10 shows peak values of P_{cav} as a function of P_+ at different steps.

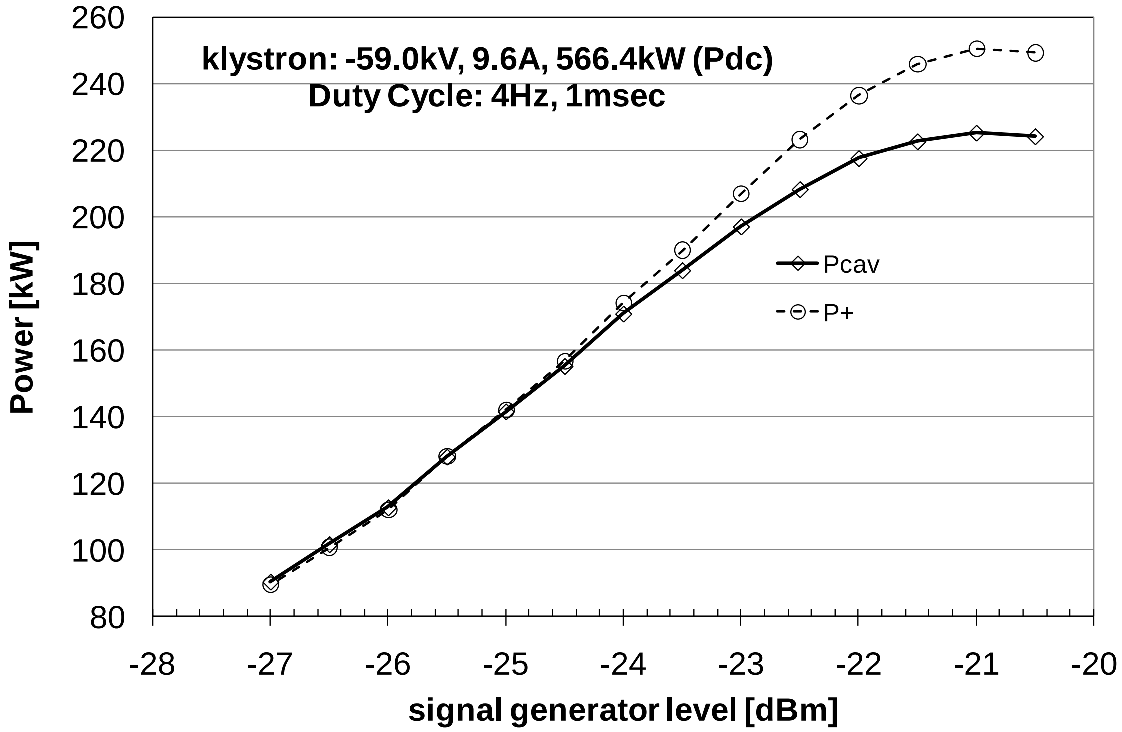

Figure B.9: P_{cav} and P+ as a function of signal from generator. Above -23 dBm klystron saturation and power losses in electron loading phenomena could be noticed.

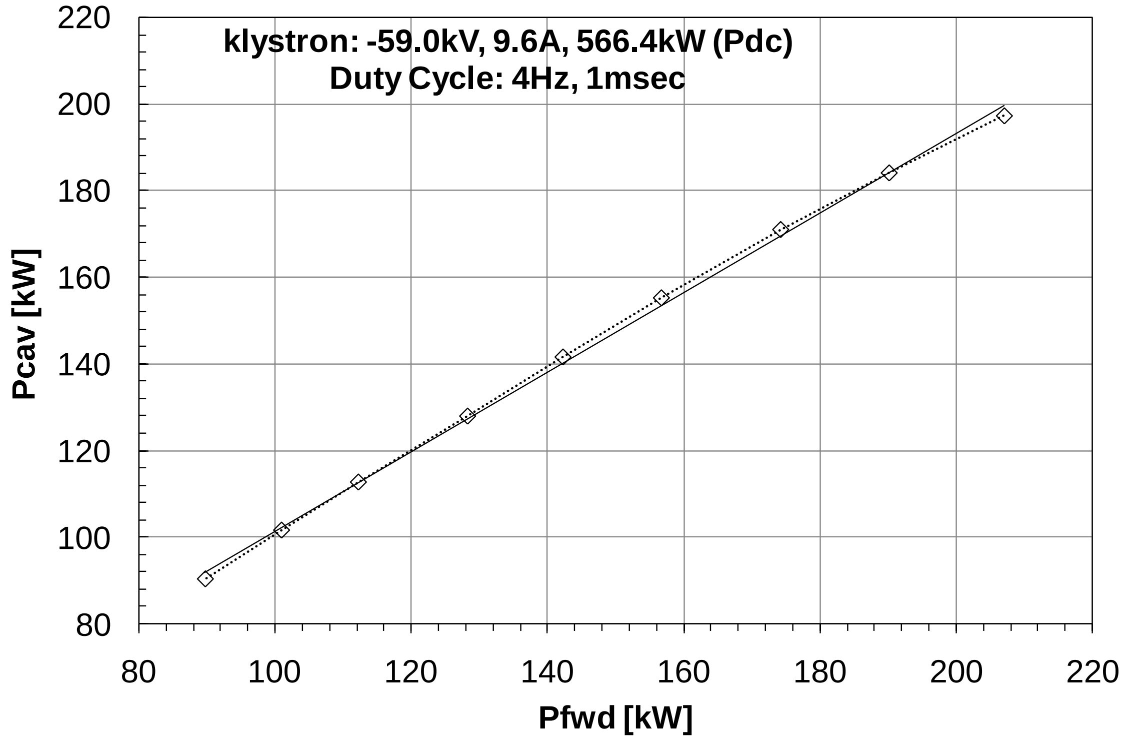

Figure B.10: P_{cav} (peak and average) as a function of P_+ from klystron at different step of conditioning. P_- is zero.

References

[1] T. Wangler, “RF Linear Accelerators”, John Wiley & Sons, Inc. 1998, chap.5.

[2] P. Balleyguier, " *A Straightforward Method* for *Cavity External Q Computation*”, Part. Accelerators, 1997, Vol. 57, 113.

Appendix C. Equivalent circuit for the Stems

In this appendix the stem equivalent circuit is presented, together with and a sample of parameter determination based on the frequencies measured for the DTL hot prototype.

The equivalent circuit for the analysis of stem resonances is shown in Figure C.1 [1]. In this circuit the series inductor $L_0/2$ represents the inductance of a half DT, the series capacitor C_0 corresponds to the capacitance of a gap, the shunt capacitor C_s summarizes the capacitance of a DT to the tank wall represented by the ground conductor. Stems are represented by inductors L_s in parallel with the shunt capacitance C_s. Each inductor is magnetically coupled with the next one by means of the mutual inductance M_s. The stem inductance L_s is written as 2 inductors $2\times L_s$ in parallel, in order to separate the mutual coupling with the previous stem from the mutual coupling with the next stem.

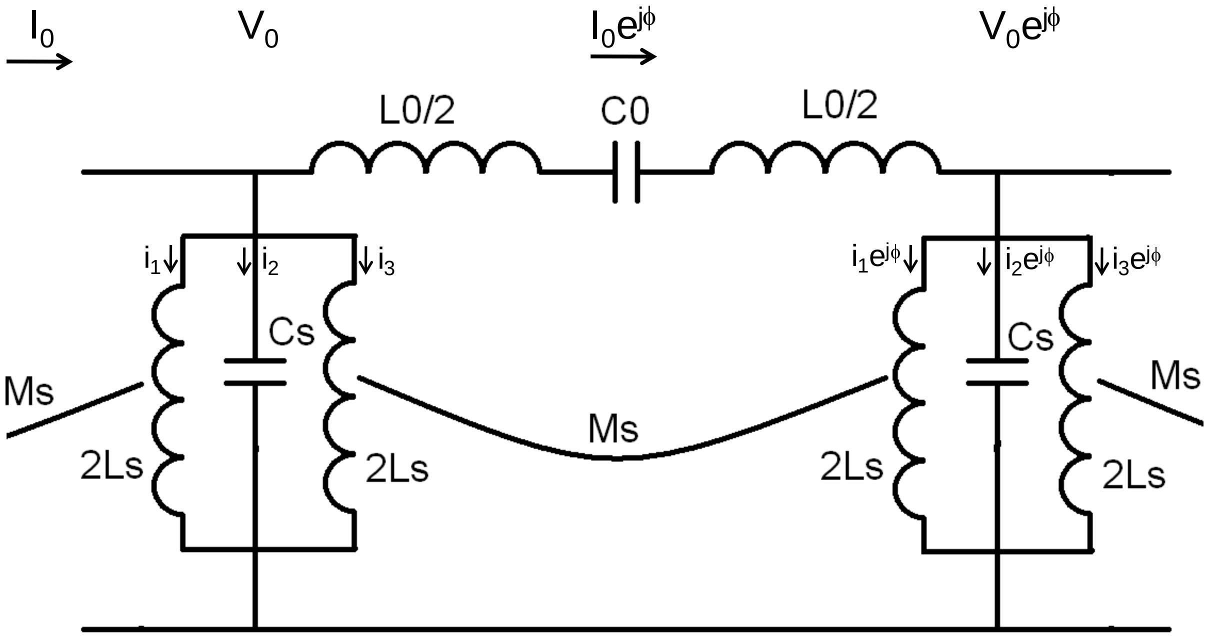

Figure C.1: equivalent circuit of a basic DTL cell with stems.

The equivalent circuit for the stems has been solved by applying Floquet's theorem for periodic structures. Currents and voltages are multiplied by a factor $e^{j\phi}$ when we move by one period along the chain. The system is described by 5 equations:

$$V_0 e^{-j\phi} - V_0 = I_0\left(j\omega L_0 + \frac{1}{j\omega C_0}\right) \quad \text{(C.1)}$$

$$V_0 = 2j\omega L_s i_1 + j\omega M_s i_3 e^{-j\phi} \quad \text{(C.2)}$$

$V_0 = 2j\omega L_s i_3 + j\omega M_s i_1 e^{j\phi}$ (C.3)

$V_0 = \dfrac{i_2}{j\omega C_s}$ (C.4)

$I_0 - I_0 e^{j\phi} = i_1 + i_2 + i_3$ (C.5)

From equations (C.2), (C.3) and (C.4) we have

$$i_1 + i_2 + i_3 = jV_0 \frac{-4L_s + 4C_s L_s^2 \omega^2 - C_s M_s^2 \omega^2 + 2M_s \cos(\phi)}{(4L_s^2 - M_s^2)\omega}.$$

Equations (C.1) and (C.5) give the ratio V_0/I_0 and the dispersion equation

$$\frac{-j(1-e^{j\phi})(4L_s^2 - M_s^2)\omega}{-4L_s + 4C_s L_s^2\omega^2 - C_s M_s^2 \omega^2 + 2M_s \cos(\phi)}(1-e^{j\phi}) = \frac{1}{e^{-j\phi} - 1 \;\; j\omega C_0}\left(1 - \frac{\omega^2}{\omega_0^2}\right)$$

which can be written as

$$a(1-\cos(\phi)) = \frac{\omega^2 - \omega_0^2}{\omega^2 \omega_0}\sqrt{\frac{C_s(2L_s + M_s)}{2}}\left(\omega^2 - \frac{2\cdot\; 1 + b(1-\cos(\phi)}{C_s(2L_s + M_s)}\right)$$

with $a = 2\sqrt{\dfrac{C_0}{L_0}\dfrac{L_s}{C_s}\left(1 + \dfrac{M_s}{2L_s}\right)}$ and $b = \dfrac{M_s}{2L_s - M_s}$.

The equation has 2 solutions for $\phi=0$:

- the zero mode (TM_{010}) of the main resonator chain $\omega_0 = 1/\sqrt{C_0 L_0}$ and
- the zero mode of the stem resonator chain $\omega_s = \sqrt{2}/\sqrt{C_s(2L_s + M_s)}$.

The previous equation can be simplified to

$$a(1-\cos(\phi)) = \frac{\omega^2 - \omega_0^2}{\omega^2 \omega_0 \omega_s}\sqrt{\frac{C_s(2L_s + M_s)}{2}} \;\; \omega^2 - \omega_s^2 \cdot\; 1 + b(1-\cos(\phi) \quad .$$

The DTL hot prototype consists of 13 accelerating cells and 12 stem cells. In order to determine parameters a, b, ω_0 and ω_s we use measured frequencies of modes 0 and $3\pi/13$ of the TM band and modes 0 and $4\pi/12$ of the Stem band. Results are in Table C.1.

Capacitance C_0 can be calculated from a Superfish simulation of the DTL hot prototype, using the relation $U = 1/2 \times (C_0 V^2)$. Then from formulas of ω_0, ω_s, a and b parameters we obtain circuit element values listed in Table C.2, in comparison with values obtained from geometrical formulas in Chapter 5. They show a good agreement.

Finally, Figure C.2 shows the comparison between frequencies measured on the DTL prototype and dispersion curves calculated with equivalent circuit, using parameter values listed in Table C.1.

mode	Frequency	parameter	value
TM_{010} (ϕ=0)	351.8 MHz	ω_0	351.8 MHz
TM_{012} (ϕ=2π/13)	462.5 MHz	ω_s	174.1 MHz
Stem 0 (ϕ=0)	174.1 MHz	a	10.9
Stem 4 (ϕ=4π/12)	151.9 MHz	b	4.6

Table C.1: measured frequencies and values of equation parameters.

parameter	Value	Geom. value (Chap.5)
C_0 [pF]	9.07	3.76
L_0 [nH]	22.7	49
C_s [pF]	3.32	4.44
L_s [nH]	138	144
M_s [nH]	227	-

Table C.2: stem circuit parameters fitted from frequency measurements in comparison with values calculated with geometrical formulas in Chapter 5.

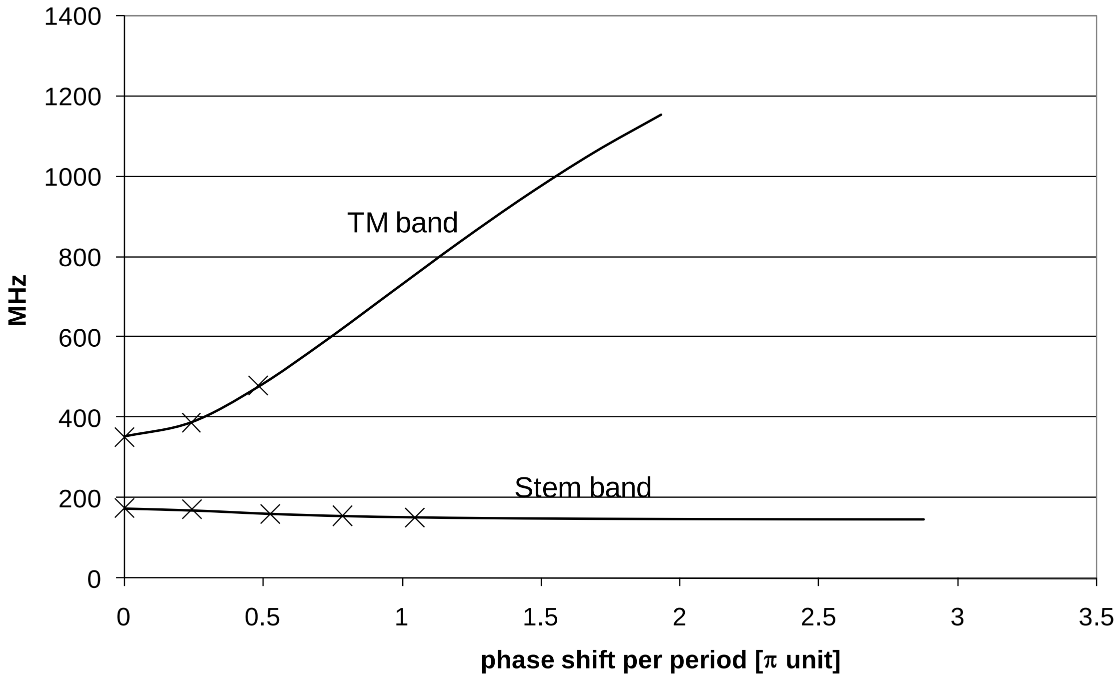

Figure C.2: comparison between measured (crosses) and calculated (continuous lines) dispersion curves.

References

[1] K. Batchelor et al., " Numerical Analysis of the RF Field in a Drift Tube Loaded Cavity", Proc. PAC1967.

Acknowledgements

I would like to thank peoples which have contributed to this thesis work.

First of all my supervisors, Andrea Pisent (LNL-INFN) and Suitbert Ramberger (CERN), for their attention and steers.

My friends and colleagues, Antonio Palmieri and Giovanni De Michele, for their continuous support, collaboration and patience.

Maurizio Vretenar and Jean Michel Giguet, for what I have learned from their experience.

Finally, I thank my family.